Chapter 5

THE RADIATION BELTS

W.N. Spjeldvik and P.L. Rothwell

Interaction of the solar wind flow with the earth's magnetic field gives rise to a cavity in the interplanetary medium known as the earth's magnetosphere. Within this cavity there exists a limited region where the motion of energetic particles is confined by the earth's magnetic field. This region comprises the earth's *radiation belts* as depicted in Figure 5-1. The radiation belt region contains electrons, protons, helium, carbon, oxygen, and other
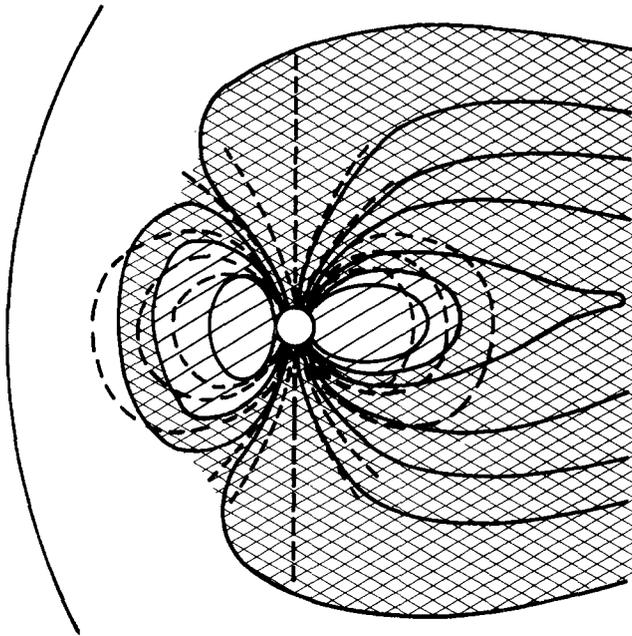

Figure 5-1. Cross-section of the earth's magnetosphere in the noon-midnight meridian showing relative locations (lightly shaded regions) of the earth's radiation belts in the overall magnetospheric topology.

ions with energies from less than 1 keV to hundreds of MeV. Particles below 200 keV energy represent the principal corpuscular energy density and form the extraterrestrial ring current. Confinement (or trapping) of these particles results from the dipolar-like topology of the geomagnetic field which is characterized by magnetic field lines that converge at high latitudes towards the poles resulting in a relative minimum magnetic field strength region in the vicinity of the geomagnetic equa-

tor. Figure 5-2 illustrates principal aspects of a charged particle trajectory in magnetic mirror field geometry. The
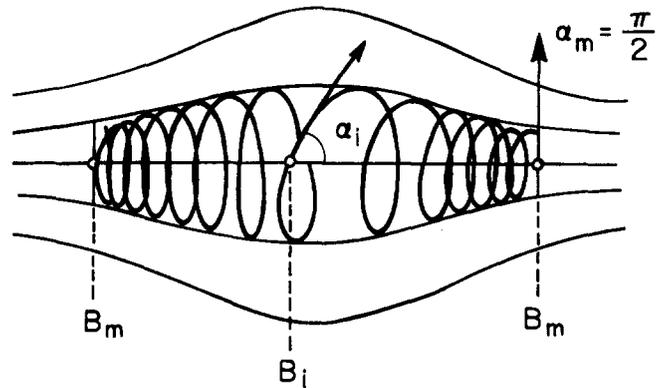

Figure 5-2. A charged particle trajectory in a magnetic "bottle". Conservation of the first adiabatic invariant can cause the spiraling particle to be reflected where the magnetic field is stronger. This causes the particle to be trapped by the magnetic field.

magnetic force ($F \propto V \times B$) deflects the particle velocity vector V so that the particle spirals around the magnetic field B. The convergence of the magnetic lines of force causes a tightening of the spiral angle and eventually a reflection of the particle from the high magnetic field region (mirror point); for this reason the earth's magnetic field is capable of confining charged particles. A detailed account of single particle motion in magnetic fields is found in Roederer [1970].

To a fair approximation, the earth's magnetic field in the radiation belt region can be described in terms of a magnetic dipole located near the center of the earth. The dipole moment is $M = 0.312$ G R_E^3, and the dipole is directed so that the magnetic south pole on the earth's surface is located in northern Greenland (geographic coordinates: 78.5°N, 291°E); on the earth, the northern end of the compass needle points to this location. The spatial distribution of the dipolar magnetic field strength is

$$B = B_E \left(\frac{R}{R_E}\right)^{-3} \frac{[4-3\cos^2\lambda]^{1/2}}{\cos^6\lambda} \qquad (5.1)$$

where R is the radial distance measured from the center of the earth, R_E is the radius of the earth, $B_E = 0.312$ G is the equatorial field at $R = R_E$ and λ is magnetic latitude. A detailed account of the earth's magnetic field and its variability is found in Chapman and Bartels [1951]. Since the geomagnetic field is inhomogeneous, a radiation belt particle experiences varying magnetic field strengths over its trajectory. Field variations on a length scale of the order of the particle's gyroradius cause a net drift across the magnetic field in the azimuthal direction around the earth as illustrated in Figure 5-3. This is a direct result of the field strength being greater closer to the earth causing
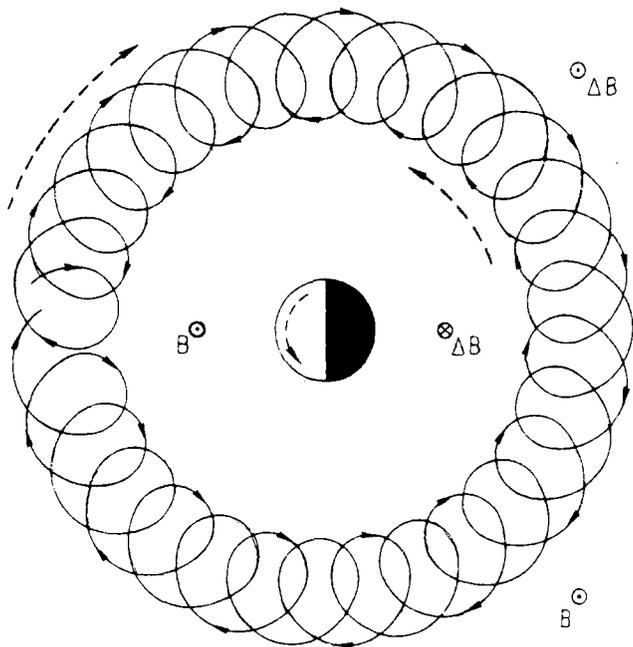

Figure 5-3. Schematic representation of the gyration and azimuthal drift (solid curve) of an equatorially mirroring proton with associated current patterns (dashed curves) [Shulz and Lanzerotti, 1974].

the particle orbital radius of curvature to be less there. The direction of the magnetic force depends on the sign of the particle charge: electrons drift eastward and positive ions drift westward. Thus the energetic trapped particles are spread out in a belt-like configuration around the earth, forming the *radiation belts*.

Radiation belt electrons move at very high speeds. For example, electrons with a kinetic energy of 500 keV move at 85% the speed of light. Radiation belt electrons must thus be studied using relativistic theory. Ions, because they are substantially heavier, generally move at subrelativistic velocities; at 500 keV the proton speed is 3% of the speed of light, while the heavier ions are even slower at the same energy.

The composition and flux intensities of the earth's radiation belts are determined by the strength of the

sources, internal transport processes, and loss mechanisms. The outer boundary of the radiation belt trapping region occurs at the point where the magnetic field is no longer able to maintain stable trapping, and at low altitudes the earth's atmosphere forms an effective boundary for radiation belt particles. During geomagnetically quiet conditions, the radiation belt region extends from the top of the atmosphere along dipole field lines to an equatorial radial distance of at least 7 earth radii. Energetic ions and electrons that encounter the dense atmosphere collide with the atmospheric constituents and are readily lost from the radiation belts. Particles with mirror points well inside the atmosphere (nominally below ~100 km altitude) are said to be within the atmospheric (bounce) *loss cone*. Kinematically, the angle between the velocity vector of such particles and the magnetic field direction (the pitch angle) at the equator is below a certain value, known as the loss cone angle. Figure 5-4 exemplifies this.
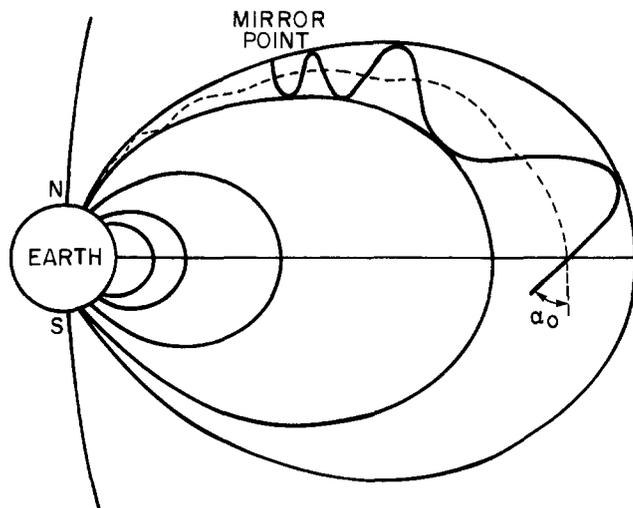

Figure 5-4. Illustration of magnetic mirroring in a dipolar magnetic field. The single particle trajectory shown in the solid line is for a particle outside the atmospheric bounce loss cone and the dashed line represents the trajectory of a particle inside the loss cone. The latter particle will encounter the denser parts of the earth's atmosphere (mirror point height nominally below 100 km) and will thus precipitate from the radiation belts.

The earth's radiation environment is best studied with combined experimental and theoretical means. On one hand, it is impossible to encompass the entire magnetosphere by experimental techniques or even to measure all the physical parameters that may have bearing on the dynamical phenomena; on the other hand, this environment is so complex that there can be little hope of theoretically predicting the total radiation belt behavior solely from a set of mathematical postulates. For example, the governing diffusion equations describing the trapped radiation phenomena may be known in analytic form,

but the transport coefficients that enter into them must be empirically determined.

This chapter gives an account of these and other applied concepts. The current state of knowledge of the geomagnetically trapped radiation is described both from the theoretical perspective and from direct observations. We demonstrate how this knowledge is used to construct physical models of the radiation belts. Empirical radiation belt models based on data compiled from many spacecraft and a brief survey of man's interaction with geospace are also presented.

5.1 THEORETICAL PRELIMINARIES

The difficult mathematical problem of the motion of energetic charged particles in a dipolar magnetic field was extensively studied during the first half of the twentieth century. A general analytic solution to the equation of motion was never found, and in most cases particle orbit tracing had to be done numerically. The interested reader is referred to Störmer [1955]. Physical approximations that lead to great simplification have, however, been found. This is known as the *adiabatic theory* for trapped particles [Alfvén and Fälthammer, 1963], and the earth's radiation belts have now been successfully described in terms of adiabatic invariants and their perturbation.

5.1.1 Single Particle Motion

An ensemble of ions and electrons moving in space constitutes a plasma that can exhibit many modes of collective as well as single particle behavior. In the presence of electric (E) and magnetic (B) fields these particles are subject to the electromagnetic Lorentz force, $F = q(E + V \times B)$, where q and V are the particle charge and velocity vector respectively. For ions q = Ze, where Z is the ionic charge state and e is the unit charge; for electrons q = −e. This force controls the particle motion, and collectively the ensemble of charged particles can modify the fields through induction, charge separation, and electrical currents formed by differential ion and electron motion. When the latter effects are negligible, the particles move independently of each other and the *single particle motion* approximation is applicable.

For geomagnetically trapped particles there exist three quasi-periodic motions: gyro motion around the magnetic field lines, bounce motion between the conjugate mirrorpoints, and drift motion around the earth. The fundamental physics in this approximation is described in detail by Alfvén and Fälthammar [1963]. One should note that the frequencies associated with each of these periodic motions are such that $f_{gyro} \gg f_{bounce} \gg f_{drift}$. For this reason the three types of motions are largely uncoupled. Figure 5-5 illustrates numerical values of
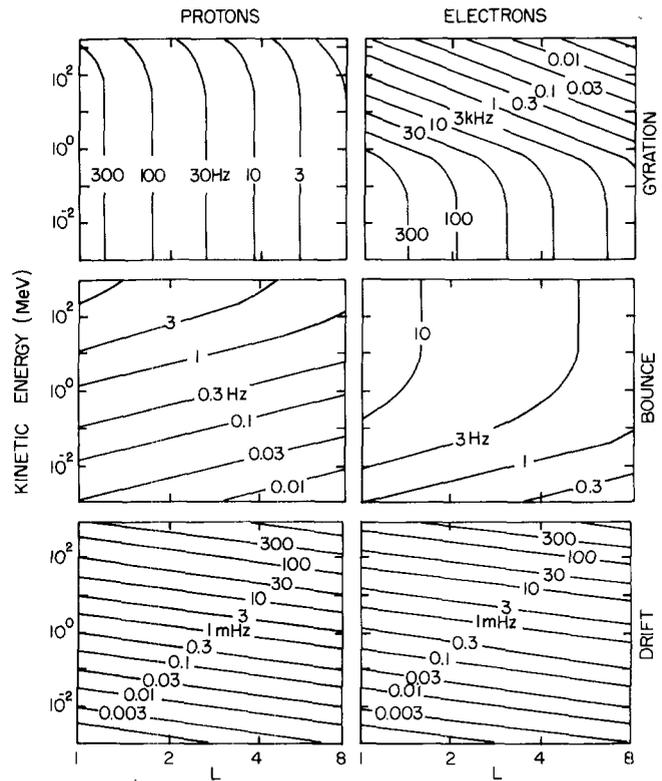

Figure 5-5. The gyration, bounce, and drift frequencies for equatorially mirroring particles in a dipole field as function of L-shell for different particle energies [Shulz and Lanzerotti, 1974].

these fundamental particle motion frequencies for protons and electrons in the earth's radiation belts [Schulz and Lanzerotti, 1974].

5.1.2 Adiabatic Invariants

In general, the motion of charged particles is such that momentum and energy can be transferred between the different particles, and between the particles and the fields that influence their motion. Therefore, it is not always possible to identify constants of motion. However, under certain conditions these energy and momentum exchanges are very small, and it is possible to identify specific quantities that remain virtually unchanged with the particle motion. These are called *adiabatic invariants*.

Associated with each of the three quasi-periodic modes of motion is an adiabatic invariant related to the Hamilton-Jacobi action variable:

$$J_i = \oint_i [P + \frac{q}{c} A] \cdot d\ell \qquad (5.2)$$

where $d\ell$ is a vector line element along the path of integration. Here P is particle momentum and A is the magnetic vector potential (that is, $B = \nabla \times A$). The integration

is extended over the particle orbit for gyro motion, bounce motion, and azimuthal drift motion (for i = 1, 2, 3 respectively). If the particle's trajectory closed exactly on itself, then the action variables J_i would be absolute constants of motion. Finite spatial and temporal variations in **B** prevent perfect closure, and thus the J_is are at best *approximate* constants.

5.1.2.1 First Adiabatic Invariant.

J_1 is obtained by evaluating the integral in Equation (5.2) over the particle gyro motion only, that is, over the particle orbit projection in a plane perpendicular to **B**. Using subscripts $\parallel$ and $\perp$ to denote directions parallel and perpendicular to **B**, and by virtue of Stokes' theorem [Schultz and Lanzerotti, 1974] one derives

$$J_1 = 2\pi\rho_g P_\perp + \frac{q}{c}\,\pi\rho_g^2 B \ . \qquad (5.3)$$

where $B = |\mathbf{B}|$, p is particle momentum and $\rho_g = P_\perp/|q|\,B$ is the particle gyro (or cyclotron) radius. From this, one defines the first adiabatic invariant

$$\mu = \frac{P_\perp^2}{2m_o B} = \frac{P^2 \sin^2\alpha}{2m_o B} \ , \qquad (5.4)$$

also known as the relativistic magnetic moment. Here m_o is the particle rest mass, and α = arc sin ($\mathbf{B}\cdot\mathbf{P}/PB$) is the pitch angle illustrated in Figure 5-6.
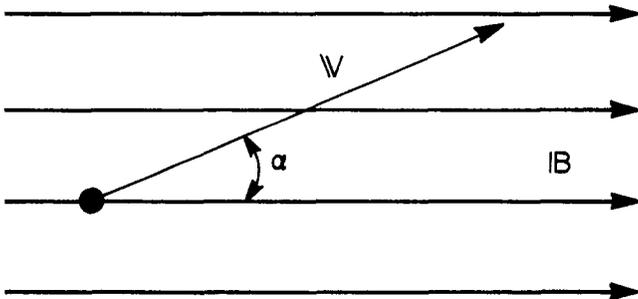

Figure 5-6. A particle with its velocity vector inclined to the magnetic field at an angle α. This angle is called the particle pitch angle.

For non-relativistic particles,

$$\mu = \frac{\epsilon_\perp}{B} = \frac{\frac{1}{2}m_o V_\perp^2}{B} \qquad (5.5a)$$

where $\epsilon_\perp$ is the particle kinetic energy associated with the directions perpendicular to the local magnetic field direction, while for relativistic particles

$$\mu = \frac{P_\perp^2}{2m_o B} = \gamma^2\left[\frac{\frac{1}{2}m_o V_\perp^2}{B}\right] \qquad (5.5b)$$

where the relativistic factor $\gamma = 1\ \sqrt{1-v^2/c^2}$. μ is an approximate constant of motion when both of the following conditions are fulfilled:

— The *spatial* scale of B-field variation is much larger than the particle gyroradius

$$\frac{B}{|\nabla B|} \gg \rho_g = P_\perp/B|q| = \gamma m_o V \sin\alpha/B|q| \qquad (5.6)$$

— The time scale of change of the B-field is much larger than the particle gyroperiod

$$T \gg \tau_g = 2\pi\rho_g/v_\perp = 2\pi\gamma m_o/B|q|. \qquad (5.7)$$

5.1.2.2 Second Adiabatic Invariant.

J_2 is obtained by evaluating the integral in Equation (5.2) over the bounce trajectory and averaged over the gyro motion, or equivalently along the magnetic field line (guiding center field line) around which the particle gyrates, and thereby defining the second adiabatic invariant:

$$J = \frac{1}{2}\,J_2 = \frac{1}{2}\oint \mathbf{P}\cdot d\ell = \int_{-\ell_m}^{+\ell_m} P_\parallel\,d\ell \qquad (5.8)$$

where $d\ell$ is an element of length along that field line segment and ℓ_m is the curvelinear distance of the mirrorpoints from the equator measured along the guiding center magnetic field line. Since equatorially mirroring particles ($\alpha_o = \pi/2$) do not have any bounce motion, it follows that J=0 for such particles.

Provided the particle mirrorpoints are above the dense atmosphere, J will remain an approximate constant when the time scale of B-field variation is much larger than the particle bounce time between the conjugate mirrorpoints

$$T \gg \tau_B = \int_{-\ell_m}^{+\ell_m} d\ell\,/V_\parallel(\ell)\ . \qquad (5.9)$$

Constancy of the first adiabatic invariant μ implies that

$$\frac{\sin^2\alpha_o}{B_o} = \frac{\sin^2\alpha}{B} = \frac{1}{B_m} = \text{constant} \qquad (5.10)$$

over the bounce motion between the mirror points. Here the subscript zero denotes equatorial quantities and B_m is the magnetic field induction at one of the mirror points

(where $\alpha = \pi/2$). Equation (5.10) is known as the mirror equation. Using (5.10) one finds

$$\tau_B = \frac{m_0\gamma}{P} \int_{-\ell_m}^{+\ell_m} d\ell \left(1 - \frac{B}{B_0}\sin^2\alpha_0\right)^{-\frac{1}{2}}$$

$$= \frac{m_0\gamma}{P} \int_{-\ell_m}^{+\ell_m} d\ell \left(1 - \frac{B}{B_m}\right)^{-\frac{1}{2}}, \qquad (5.11)$$

and in dipolar coordinates (Equation 5.11) becomes

$$\tau_B = \frac{2m_0\gamma}{P} T(\alpha_0), \qquad (5.12)$$

where $T(\alpha_0)$ is the bounce time integral given by

$$T(\alpha_0) = \int_0^{\lambda_m(\alpha_0)} \frac{\cos\lambda\,[4-3\cos^2\lambda]\,d\lambda}{\left\{1 - \frac{\sin^2\alpha_0}{\cos^6\lambda}[4-3\cos^2\lambda]^{1/2}\right\}^{1/2}}, \qquad (5.13)$$

and $\lambda_m(\alpha_0)$ is the magnetic latitude of the mirrorpoint which depends on the equatorial pitch angle α_0.

To a fair approximation

$$T(\alpha_0) \approx 1.30-0.56\sin\alpha_0 \quad [\text{Hamlin et al., 1961}], \qquad (5.14)$$

or alternatively

$$T(\alpha_0) \approx 1.3802-0.3198\,(\sin\alpha_0 + [\sin\alpha_0]^{1/2})$$

[Schulz and Lanzerrotti, 1974]. $\qquad (5.15)$

Other approximations are given by Davidson [1973]. Gradients of $T(\alpha_0)$ should, however, not be derived from such approximations. From Equations (5.1) and (5.10) it follows that

$$B_m = \frac{B_0}{\sin^2\alpha_0} = \frac{B_E}{L^3\sin^2\alpha_0}, \qquad (5.16)$$

where in a dipolar magnetic field $L = (R/R_E)$ is the equatorial distance of a given field line, and

$$\sin^2\alpha_0 = \frac{\cos^6\lambda_m(\alpha_0)}{[4-3\cos^2\lambda_m(\alpha_0)]^{1/2}}. \qquad (5.17)$$

Although Equation (5.17) cannot be solved explicitly for $\lambda_m(\alpha_0)$, a numerical solution is easily obtained, or one may approximate as in Hamlin et al. [1961]

$$\cos\lambda_m(\alpha_0) \approx [\sin\alpha_0]^{1/4}. \qquad (5.18)$$

It should be emphasized that using a dipolar magnetic field representation explicitly disregards any azimuthal asymmetries of the geomagnetic field. Such asymmetries do exist and become significant beyond L=5. Under such conditions a different magnetic field representation should be used, and this is outlined in Section 5.6.1.4.

5.1.2.3 Third Adiabatic Invariant. J_3 is obtained by evaluating the integral in Equation (5.2) over the particle drift motion around the earth, and averaged over gyro and bounce motion

$$J_3 = \frac{q}{c}\Phi = \frac{q}{c}\oint \mathbf{A}\cdot d\mathbf{l} \qquad (5.19)$$

where Φ is the magnetic flux enclosed by the azimuthal drift orbit and l is linear azimuthal distance. Using Stokes' theorem yields

$$\Phi = \oint \mathbf{A}\cdot d\mathbf{l} = \int_S \mathbf{B}\cdot d\mathbf{S}, \qquad (5.20)$$

where S is a surface bounded by the azimuthal drift path. In a dipolar magnetic field one calculates [Roederer, 1970]

$$\Phi = -\frac{2\pi B_E R_E^2}{L}, \qquad (5.21)$$

where L is the McIlwain [1961] L-parameter.

J_3 will remain approximately constant when the time scale of B-field change is much longer than the azimuthal drift time $\tau_d = \oint_{\text{drift}} ds/V_d$ around the earth. Determination of the azimuthal drift velocity is discussed in the next section.

5.1.3 Particle Drift Motion. In a uniform magnetic field, charged particles execute a spiral motion such that the angle between the particle velocity vector and the magnetic field direction (the pitch angle) remains constant. When the magnetic field lines converge, the particle will respond to an effective net magnetic force from

higher to lower magnetic field strengths. This is illustrated in Figure 5-7. The physical reason for this force is
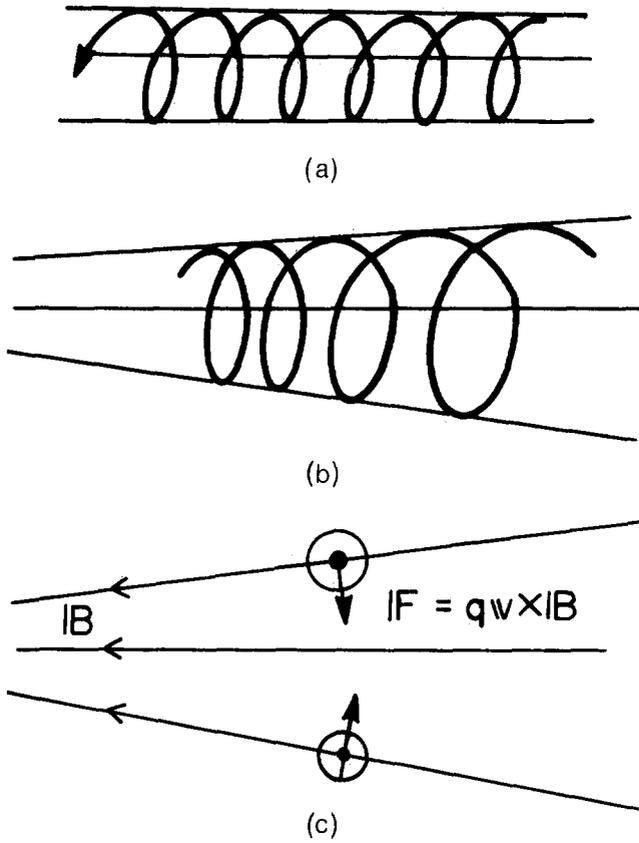

(a)

(b)

(c)

Figure 5-7. (a) Particle motion in a uniform magnetic field (uniform spiral motion).
(b) The tightening of spiral motion in a converging magnetic field.
(c) Illustration of magnetic force with gyroaveraged net component in the $-\nabla B$ direction in a converging magnetic field.

that the particle gyro motion produces an elementary current (which may be interpreted as a magnetic dipole current loop). For each such loop the effective current is

$$i_p = \frac{dq}{dt} = \frac{qP_\perp}{2\pi\rho_g m_o \gamma}, \qquad (5.22)$$

where ρ_g is the mean gyroradius over the loop. The magnetic moment of a current loop enclosing an area A is

$$M = i_p A = \frac{P_\perp^2}{2m_o \gamma B} \qquad (5.23)$$

where $A = \pi\rho_g^2$, which is the particle magnetic moment itself. The particle will therefore, averaged over its gyro motion, be subject to a net force $F = -M v_\parallel |B|$ in the direction along the field lines away from the higher field region.

In general, the magnetic field may also have an intensity gradient across the field lines. This is illustrated in Figure 5-8. Charged particles moving in such a magnetic
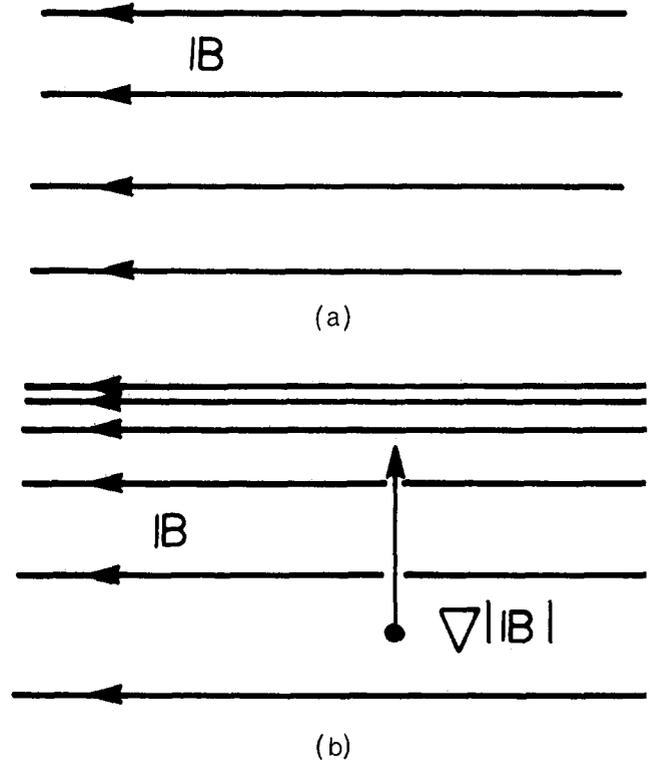

(a)

(b)

Figure 5-8. (a) A uniform B-field where field lines are represented as evenly spaced.
(b) A magnetic field with increasing strength perpendicular to B, represented as denser field lines with increasing B.

field will have a smaller gyroradius in the higher field region and a larger gyroradius in the lower field region. As a consequence, there will be a net drift velocity perpendicular to the magnetic field direction. In this figure a positive charge would drift into the paper and a negative charge out of the paper. Defining the angular gyrofrequency

$$\Omega = \frac{|q| B}{m_o \gamma c}, \qquad (5.24)$$

one can express the instantaneous vector gyroradius as

$$\rho_g = \frac{P \times B}{m_o \gamma \Omega B} = c \frac{P \times B}{qB^2}, \qquad (5.25)$$

and the drift velocity is then the time rate of change of ρ_g

$$V_d = \frac{d\rho_g}{dt} = \frac{c}{qB^2}\left(\frac{dP}{dt} \times B\right) \qquad (5.26)$$

where it is assumed that the magnetic field is constant in time. With $\mathbf{F} = \dfrac{d\mathbf{p}}{dt}$ being the net force due to the cross-B gradient, one obtains the "gradient drift"

$$\mathbf{V}_{gd} = \frac{c}{qB^3} (-M\nabla_\perp |\mathbf{B}| \times \mathbf{B}),$$

$$= -\frac{Mc}{qB^2} (\nabla_\perp |\mathbf{B}| \times \mathbf{B}), \qquad (5.27a)$$

$$= -\frac{cP_\perp^2}{2m_oq\ \gamma B^3}(\nabla_\perp |\mathbf{B}| \times \mathbf{B}),$$

which non-relativistically is just

$$\mathbf{V}_{gd} = \frac{c\epsilon_\perp}{qB^3} (\mathbf{B} \times \nabla_\perp |\mathbf{B}|) . \qquad (5.27b)$$

The earth's magnetic field is also curved (that is, the dipolar-like field lines form loops from pole to pole), and the field line radius of curvature is given by

$$R_c = \frac{R_o}{3} \cos\lambda \frac{(1+3\sin^2\lambda)^{3/2}}{1+\sin^2\lambda}, \qquad (5.28)$$

where the individual field lines are described by the dipole relation

$$R = R_o \cos^2\lambda \qquad (5.29)$$

with $R_o = R_E L$. Thus a charged particle moving in that field will experience a centrifugal force

$$\mathbf{F}_c = \frac{p_\parallel^2}{m_o\gamma R_c} \mathbf{n} \qquad (5.30)$$

where $\mathbf{n}$ is a unit vector in the direction away from the instantaneous field line center of curvature. This causes a drift velocity

$$\mathbf{V}_{cd} = \frac{c}{qB^2} \left(\frac{p_\parallel^2}{m_o\gamma R_c} \mathbf{n} \times \mathbf{B} \right) , \qquad (5.31)$$

and in the absence of significant plasma currents $\mathbf{V} \times \mathbf{B} = \mathbf{0}$ and $\nabla_\perp |\mathbf{B}| = -\dfrac{|\mathbf{B}|}{R_c} \mathbf{n}$ [Roederer, 1970], and one can write

$$\mathbf{V}_{cd} = \frac{cp_\parallel^2}{m_o\gamma qB^3} (\mathbf{B} \times \nabla_\perp |\mathbf{B}|) , \qquad (5.32)$$

which non-relativistically becomes

$$\mathbf{V}_{cd} = \frac{2c\epsilon_\parallel}{qB^3} (\mathbf{B} \times \nabla_\perp |\mathbf{B}|) . \qquad (5.33)$$

Although the effect of the earth's gravitational field is rather small compared to other forces on radiation belt particles, it can easily be included:

$$\mathbf{V}_{grav} = \frac{cm_o\gamma}{qB^2} (\mathbf{g} \times \mathbf{B}) \qquad (5.34)$$

where $\mathbf{g}$ is the vector gravitational acceleration.

The effect of a weak, externally imposed electric field is also easily taken into account:

$$\mathbf{V}_{ed} = \frac{c}{qB^2} (q\mathbf{E} \times \mathbf{B}) = c\,\frac{\mathbf{E} \times \mathbf{B}}{B^2} . \qquad (5.35)$$

The electric field drift is *independent* of particle charge and mass as long as either is non-zero. Thus, under the influence of an electrostatic field, ions and electrons drift together (plasma flow), while under the influence of an inhomogeneous magnetic field, oppositely charged particles drift in opposite directions (causing current flow).

The total particle drift velocity is then the superposition of the contributing drifts:

$$\mathbf{V}_d = c\,\frac{p_\perp^2 + 2p_\parallel^2}{2m_o\gamma qB^3} (\mathbf{B} \times \nabla_\perp |\mathbf{B}|) \qquad (5.36)$$

$$+ \frac{c}{B^2} (\mathbf{E} \times \mathbf{B}) + c\,\frac{m_o\gamma}{qB^2} (\mathbf{g} \times \mathbf{B})$$

$$\mathbf{V}_d = \frac{\epsilon_\perp + 2\epsilon_\parallel}{qB^3} (\mathbf{B} \times \nabla_\perp |\mathbf{B}|)$$

$$\qquad (5.37)$$

$$+ \frac{C}{B^2} (\mathbf{E} \times \mathbf{B}) + \frac{m_o\gamma C}{qB^2} (\mathbf{g} \times \mathbf{B}) .$$

In the dipolar magnetic field representation an approximate formula for the drift period is given by Davidson [1977]

$$T_d \approx \frac{1.43K_t}{L\gamma(V/c)^2\ (1+0.42\sin\alpha_o)} , \qquad (5.38)$$

where $K_t = 1.0308 \times 10^4$ seconds for electrons, $K_t = 5.655$ seconds for protons, and $K_t = \dfrac{4\pi\ Z_i^e\ B_E\ R_E^2}{3M_i\ C^3}$ for ions of mass M_i and charge state Z_i.

The cartoon in Figure 5-9 illustrates the principal drift effects associated with the different drift mechanisms. In Equations (5.36) and (5.37) the terms are listed in order of their importance in the radiation belts. Above ~10 keV the magnetic gradient curvature drift is generally strongest, and static electric field and gravity effects are usually neglected in radiation belt studies. The gradient-curvature drift carries energetic electrons towards the east and ions to the west. Thus there will be a net westward electrical current encircling the earth. This is the *extraterrestrial ring current*. These findings are summarized in Figure 5-10.

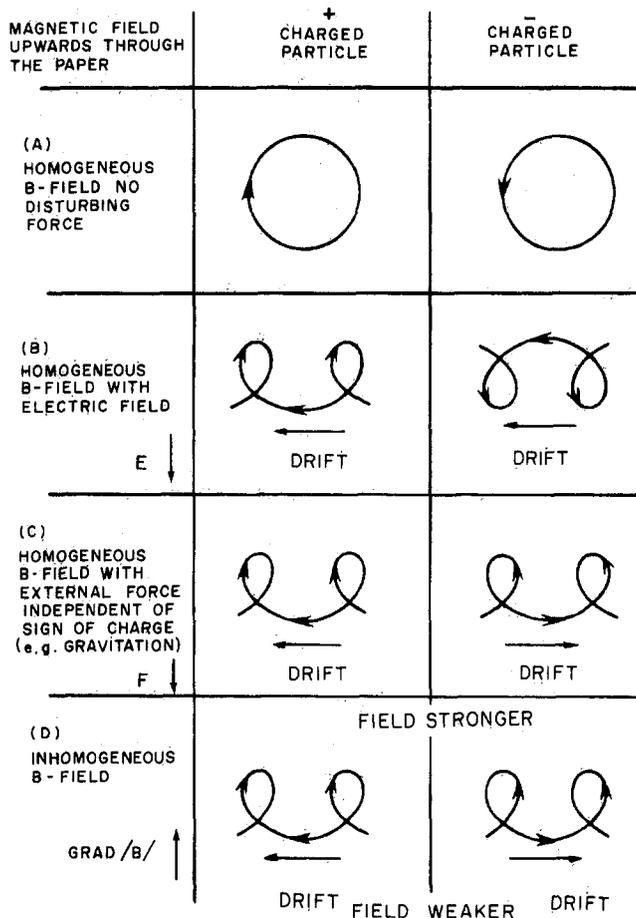| MAGNETIC FIELD UPWARDS THROUGH THE PAPER	+ CHARGED PARTICLE	− CHARGED PARTICLE
(A) HOMOGENEOUS B-FIELD NO DISTURBING FORCE		
(B) HOMOGENEOUS B-FIELD WITH ELECTRIC FIELD $E \downarrow$	DRIFT	DRIFT
(C) HOMOGENEOUS B-FIELD WITH EXTERNAL FORCE INDEPENDENT OF SIGN OF CHARGE (e.g. GRAVITATION) $F \downarrow$	DRIFT	DRIFT
(D) INHOMOGENEOUS B-FIELD GRAD /B/ $\uparrow$	FIELD STRONGER / FIELD WEAKER DRIFT	DRIFT

Figure 5-9. Summary illustration of drift of both positive and negative charged particles in a) a uniform B-field, no external force; b) a uniform B-field with a perpendicular electric field; c) a uniform B-field with an external force which is independent of electric charge such as gravity; and d) a B-field with a gradient [Alfven and Falthammar, 1963].

5.2 TRAPPED RADIATION SOURCES

Precisely where the radiation belt particles come from and how they are accelerated to energies in the keV and MeV range are still areas of research for which a comprehensive answer is not yet available.

5.2.1 Qualitative Description

A number of sources are considered responsible, and the effectiveness of each probably also varies with time:

1. Particles from the sun, including solar wind particles and energetic solar particle emissions, possibly via magnetotail storage. For a description of solar cosmic rays see Chapter 6.
2. Particles from the earth's ionosphere, including the polar wind flow into the magnetotail, particles flowing up the magnetic field lines to form the plasmasphere and particles accelerated out of the auroral ionosphere (Chapters 8 and 9).
3. Cosmic ray albedo neutron decay (CRAND) within the trapping region.
4. Particles arriving at the earth having been accelerated in interplanetary shock waves or in the magnetospheres of other planets.
5. Low energy components of galactic cosmic rays (Chapter 6).
6. *In situ* acceleration of pre-existing low energy trapped particles within the radiation belts.

The solar wind flows past the earth's magnetosphere virtually at all times (Chapter 3). Some of these particles may find their way through the outer regions of the magnetosphere to the stable trapping region [Hovestadt et al., 1978]; this process may be particularly effective during periods of southward heliospheric magnetic field. Direct transient injections of solar energetic particles probably also occur, particularly in conjunction with magnetic storms.

Ionospheric particles diffusing out of the polar ionosphere (polar wind) escape into the magnetotail region from which some may become energized and injected into the trapping region. Auroral electric fields are intermittent and can have a significant component parallel to the magnetic field, and ions and electrons from the topside auroral ionosphere can be accelerated to multi-keV energies. The wave fields associated with plasma waves may also cause particle acceleration. This could be a source of H+, He+, O+, and electrons provided other processes act to trap the particles.

Cosmic rays impacting the earth's atmosphere undergo nuclear reactions, and a flux of neutrons escapes from the top of the atmosphere. Free neutrons are unstable and decay into proton, electron and neutrino triplets on a time scale of ~1000 seconds. If the electrically charged decay products find themselves within the radiation belts, they will immediately be subject to the magnetic force and may become trapped. Empirically, this is an important source of multi-MeV protons in the innermost part of the inner radiation zone (L $\lesssim$ 1.5). There is little direct information about the efficiency of direct extraterrestrial energetic particle trapping in the radiation belts. One may surmise, however, that time variability of the geomagnetic field is needed for trapping to occur or that incident extraterrestrial energetic ions in low charge
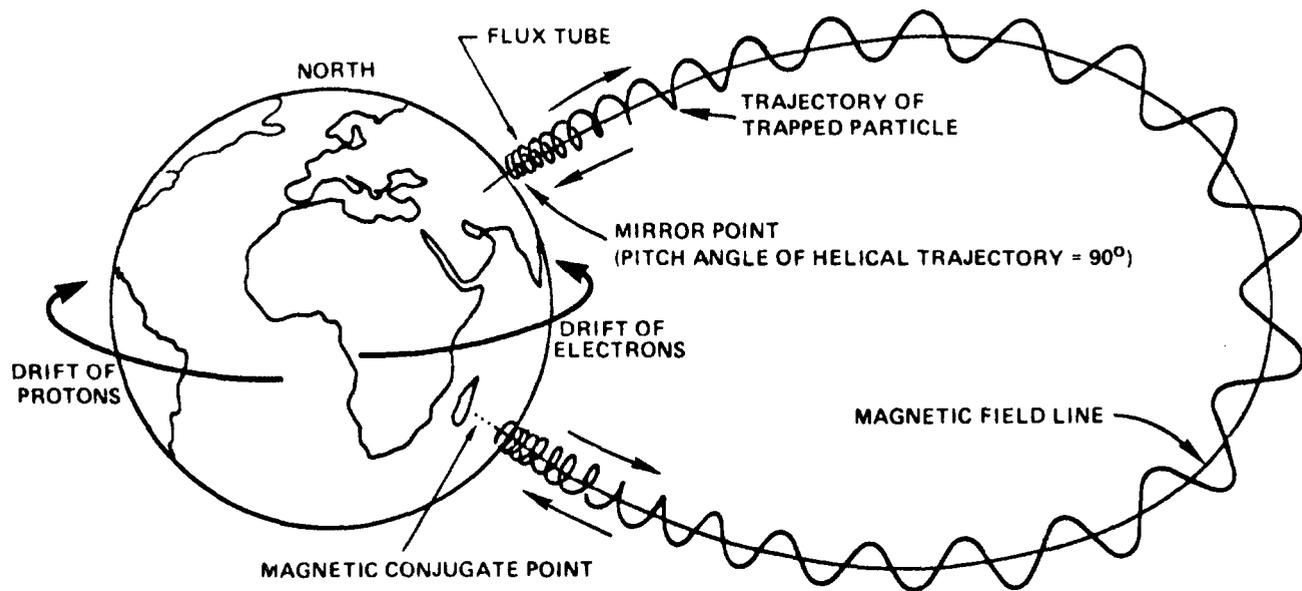
Figure 5-10. A descriptive drawing of the three types of motion of particles trapped in the earth's magnetic field.

states (for example C^+ and O^+) may charge exchange to higher charge states (for example, C^{6+} and O^{8+}) within the magnetosphere so that their gyro radii become small enough ($\rho_g = P_\perp/qB$) for trapping.

The plasma sheet in the earth's magnetotail is considered an important reservoir for radiation belt particles. However, the plasma sheet particles themselves are likely to be a mixture of particles from several of the prime sources mentioned above. During magnetospheric substorms plasma sheet particles convect inward toward the earth, and in the process can be accelerated and may become trapped in the radiation belts. Unfortunately, little is known about the specific details of the time dependent trapping process and it is not yet possible to make a quantitative evaluation of the strength and characteristics of this source.

Current research also points to the earth's ionosphere as an important contributor to the lower energy particle population below a few tens of keV, perhaps with a roughly equal contribution from solar wind particles. In contrast, the high energy particles above ~500 keV appear to have an extraterrestrial source. The former conclusion is derived from observations of dominant oxygen fluxes at times, while the latter stems from observed carbon-to-oxygen ratios of order unity. For the very important intermediate energy range where most of the radiation belt energy density is found, there is no experimental result indicating the source.

A simple theory that seeks to explain observed storm-time enhancements of radiation belt particle fluxes at tens and hundreds of keV energies has been advocated [Lyons and Williams, 1980]. Particles existing in the outer radiation zone may suddenly, during the storm main phase, be subject to an electric field that transports

them towards lower L-shells on a time scale that preserves μ and J but violates the constancy of Φ. For equatorially mirroring particles, a radial displacement from L=5 to L=3 increases the particle energy by a factor of ~5. Furthermore, if the particle spectrum follows a power law distribution $j(E) = (E/E_0)^{-u}$ with u = 3, for example, then the apparent particle flux enhancement seen at fixed energies will be a factor of 125. Seen at a fixed L-shell, the observable flux increase will be even greater if the pre-storm radial distribution falls off toward lower L-shells (as may be the case at lower radiation belt energies), and smaller if this flux gradient is negative. Given the knowledge of the storm perturbation electric field (magnitude, direction, azimuthal extent, and duration) together with observations of the pre-storm radiation belt structure, this *in situ* "source" is in principle assessable.

5.2.2 Simplifying Assumptions

For most of the radiation belt source mechanisms accurate quantitative information is still lacking. Ideally, one would like to know

1. the source strength for different particle species as a function of energy and pitch angle,
2. the effective source locations within and on the boundaries of the trapping region, and
3. the source strength as function of the different geophysical conditions during quiet and disturbed times.

Unfortunately, contemporary research has not yet yielded quantitative answers to these requirements. Without this information, how can we understand and model the earth's radiation belts?

For quiet time conditions one can solve the steady state radiation belt transport equations for the interior of the radiation belts subject to suitable outer zone *boundary conditions* on the trapped fluxes. This amounts to the assumption that the radiation belt source is capable of supplying particles to the outer radiation zone boundary at a rate sufficient to offset losses within the trapping region. The existence of long-term approximate stability of the radiation belts as a whole during extended quiet periods supports this contention, and fortunately trapped flux observations from geostationary spacecraft, such as ATS-6, of the outer zone flux levels at L = 6.6 makes this a feasible solution.

This is not a satisfactory situation for magnetic storms and other disturbances. As a consequence most radiation belt modeling has been done for steady state, quiet time conditions. Time dependent radiation belt modeling would require time dependent boundary conditions averaged over local time. It is conceivable that data from several geostationary satellites may be used for this purpose, but this has not yet been done.

5.3 TRANSPORT PROCESSES IN THE RADIATION BELTS

As we have seen, in the static geomagnetic field, radiation belt particles execute the three periodic motions: gyration around the magnetic field lines, bounce motion between mirror points, and azimuthal drift around the earth. The latter type of periodicity is caused by the gradient-curvature drift motion. Effects of gravity and electric fields cause departure from this simple picture, but both forces are primarily important at low energies typically below a few tens of keV.

5.3.1 Convection

Magnetospheric convection results from externally imposed electric fields. The solar wind flows past the earth at a velocity in the range 200-600 km/sec. This implies a "convection" electric field $E = -V/c \times B$ across the earth's magnetosphere directed from dawn to dusk. Combined with the electric field induced by the rotation of the earth a characteristic magnetospheric convection pattern is set up (Axford, 1964; Roederer, 1970). The radial corotational electric field is induced by the earth's magnetic dipole field corotating with the earth. Figure 5-11 shows model electric equipotential lines around the earth due to these electric fields in a time-independent situation. Particles of quite low energies ($\lesssim$ 1 keV) are primarily controlled by the electric field drift, and their motion approximately follows the equipotential lines as indicated by the arrows in Figure 5-11. Notice the topologically distinct regions: near the earth where the convective motion follows oval paths around the earth, and at greater distances where the drift paths are open to the magnetopause. Departures from this overall configura-
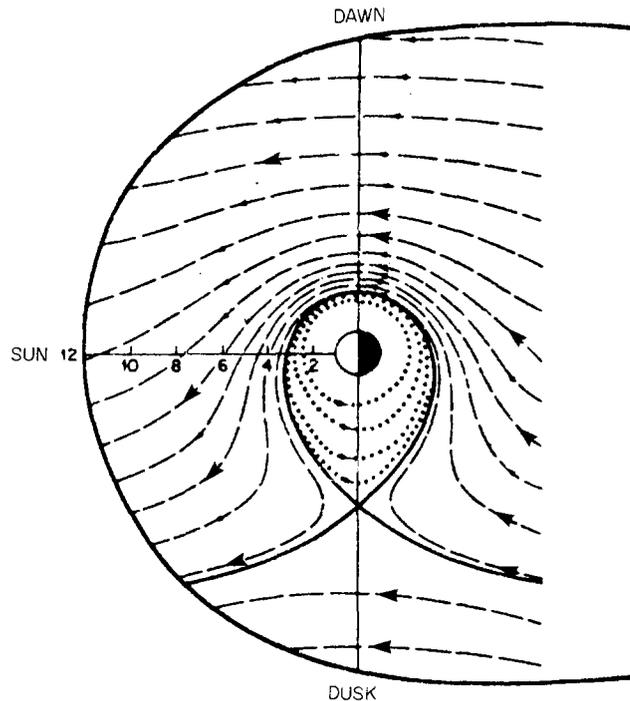

Figure 5-11. Equipotential contours for an electric field in the earth's equatorial plane (dashed lines). These are also drift paths for very low energy particles. The electric field is a superposition of a corotational E-field due to the rotation of the earth and its imbedded magnetic field and a uniform dawn-dusk electric field. The spearatix (solid curve) is the low energy particle Alfvén layer which separates the open and closed drift paths [Kivelson, 1979]. The outer oval represents the magnetopause in the equatorial plane.

tion, of course, take place during disturbed conditions when the imposed "convection" electric field is time variable and the low energy particle distributions are not in equilibrium [Harel et al., 1981 a & b].

5.3.2 Stochastic Processes: Phenomenology

At higher energies, particularly above a few tens of keV, the dominant drift of trapped particles is due to the gradient and curvature effects of the geomagnetic field. The prime drift motion is therefore circular (with gyro and bounce motion superimposed) around the earth. Departures from this pattern are due to the *fluctuating* nature of the geoelectric and geomagnetic fields induced by variations in the solar wind flow and internal magnetospheric processes. Radiation belt particles are also subject to interactions with plasma waves and suffer collisions with exospheric neutral atoms and low energy plasma particles. Common to these processes is their randomness in occurrence, and their effects are described by stochastic analysis that can be reduced to diffusion theory: radial diffusion and pitch angle diffusion. The physical ideas are illustrated in Figure 5-12. Radial diffusion transports radiation belt particles across the dipolar-like magnetic field lines in the radial direction, and pitch
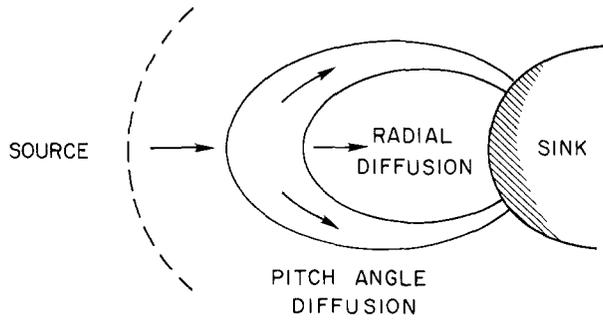
Figure 5-12. A conceptual representation of pitch angle and radial diffusion in the earth's radiation belts. Diffusion occurs in either direction, but in most cases there is a net diffusion flux in the indicated direction towards the earth's atmosphere.

angle diffusion alters the particle pitch angle (or equivalently, the mirrorpoint location). In both cases the earth's atmosphere is a sink: for radial diffusion by transport to very low L-shells, and for pitch angle diffusion by lowering the mirrorpoints into the atmosphere. In addition to diffusive processes, energy degradation from collisions with exospheric particles also occurs.

5.3.3 Effects of Field Fluctuations

Adiabatic invariants are useful substitutes for particle constants of motion. It should be kept in mind, however, that the earth's magnetic field is never perfectly static. Field fluctuations are associated with micropulsations [Jacobs, 1970], magnetospheric substorms [Akasofu, 1968], geomagnetic storms and other phenomena, and field oscillations vary considerably in magnitude, frequencies, and principal location. The adiabatic invariants are said to be violated when electric or magnetic variations take place near or above the adiabatic motion frequency in question. Even slow field variations may violate the third adiabatic invariant Φ ($T\sim$ minutes to hours) while μ-violation requires wave-like fluctuations on a time scale of $\sim$milliseconds. Macroscopically, the earth's radiation belts are subject to field fluctuations that occur at quasi-random times. Their effects are best described by stochastic methods [Chandrasekhar, 1965] that treat the mean deviations in the adiabatic invariants and the associated distribution function.

Define a particle distribution function $f = f(\mu, J, \Phi; t)$ such that the number of particles located within a parameter space volume element given by $\mu - 1/2 \, d\mu$ to $\mu + 1/2 \, d\mu$, $J - 1/2 \, dJ$ to $J + 1/2 \, dJ$, $\Phi - 1/2 \, d\Phi$ to $\Phi + 1/2 \, d\Phi$ is given by

$$dN = f(\mu, J, \Phi; t) \, d\mu \, dJ \, d\Phi$$

at a time t. The function f is thus the particle density in this parameter space spanned by the adiabatic invariants. Let $P(\mu, J, \Phi; \Delta\mu, \Delta J, \Delta\Phi)$ be the probability that a

mean change $\Delta\mu$, ΔJ, and $\Delta\Phi$ takes place in the adiabatic invariants per unit time ($|\Delta\mu| << \mu$, $|\Delta J| << J$, and $|\Delta\Phi| << \Phi$). The distribution function $f(\mu, J, \Phi; t)$ averaged over gyrophase, bounce phase, and azimuthal drift phase is then governed by the relation

$$f(\mu, J, \Phi; t) = \iiint d(\Delta\mu) \, d(\Delta J) \, d(\Delta\Phi)$$
$$f(\mu-\Delta\mu, J-\Delta J, \Phi-\Delta\Phi; t-\Delta t)$$
$$P(\mu-\Delta\mu, J-\Delta J, \Phi-\Delta\Phi; \Delta\mu, \Delta J, \Delta\Phi),$$

$$(5.39)$$

and one expands f and P in Taylor series around the unperturbed quantities to arrive at

$$\frac{\partial f}{\partial t} = - \frac{\partial}{\partial\mu} \left(\frac{<\Delta\mu>}{\Delta t} f \right) - \frac{\partial}{\partial J} \left(\frac{<\Delta J>}{\Delta t} f \right)$$

$$- \frac{\partial}{\partial\Phi} \left(\frac{<\Delta\Phi>}{\Delta t} f \right) + \frac{\partial^2}{\partial\mu^2} \left(\frac{<(\Delta\mu)^2>}{2\Delta t} f \right)$$

$$+ \frac{\partial^2}{\partial J^2} \left(\frac{<(\Delta J)^2>}{2\Delta t} f \right) + \frac{\partial^2}{\partial\Phi^2} \left(\frac{<(\Delta\Phi)^2>}{2\Delta t} f \right)$$

$$+ \frac{\partial^2}{\partial\mu\partial J} \left(\frac{<\Delta\mu\Delta J>}{\Delta t} f \right) + \frac{\partial^2}{\partial\mu\partial\Phi} \left(\frac{<\Delta\mu\Delta\Phi>}{\Delta t} f \right)$$

$$+ \frac{\partial^2}{\partial J\partial\Phi} \left(\frac{<\Delta J\Delta\Phi>}{\Delta t} f \right) \qquad (5.40)$$

+ higher order terms,

where the stochastic coefficients are defined by

$$<\Delta i> = \iiint d(\Delta\mu) \, d(\Delta J) \, d(\Delta\Phi)$$

$$P(\mu, J, \Phi; \Delta\mu, \Delta J, \Delta\Phi) \, \Delta i$$

$$(5.41)$$

$$<\Delta i\Delta j> = \iiint d(\Delta\mu) \, d(\Delta J) \, d(\Delta\Phi)$$

$$P(\mu, J, \Phi; \Delta\mu, \Delta J, \Delta\Phi) \, \Delta i\Delta j$$

with i and j being μ, J or Φ in all permutations.

The transport equation (5.41) can be greatly simplified by recognizing that violation of one adiabatic invariant is almost always uncorrelated with the process violating another. In that case all cross coefficients must vanish:

$$<\Delta\mu\Delta J> = <\Delta\mu\Delta\Phi> = <\Delta J\Delta\Phi> = 0. \quad (5.42)$$

Furthermore, $<\Delta i>$ and $\frac{1}{2} <(\Delta i)^2>$ $(i = \mu, J, \Phi)$ are related. In the absence of external sources and losses, diffusion would proceed to transport particles from overabundant regions of parameter space until all gradients in the distribution function had vanished, and for each diffusion mode

$$<\Delta i> - \frac{\partial}{\partial i} \frac{<(\Delta i)^2>}{2} = 0 \quad (i = \mu, J, \Phi). \quad (5.43)$$

Equation (5.41) then simplifies to

$$\left(\frac{\partial f}{\partial t}\right)_{transp} = \sum_i \frac{\partial}{\partial i} \left(D_{ii} \frac{\partial f}{\partial i}\right) \quad (i = \mu, J, \Phi), \quad (5.44)$$

where

$$D_{ii} = \frac{<(\Delta i)^2>}{2\Delta t} \quad (i = \mu, J, \Phi). \quad (5.45)$$

Equation (5.44) is the *diffusion equation* describing the earth's radiation belts. It is valid whenever the perturbations are small (but accumulative). Transformation to other variables, such as ϕ_1, ϕ_2, ϕ_3 is facilitated by the Jacobian $G = G(\mu, J, \Phi; \phi_1, \phi_2, \phi_3)$ such that

$$\left(\frac{\partial F}{\partial t}\right)_{transp} = \sum_i \frac{1}{G} \frac{\partial}{\partial \phi_j}, \left(D_{\phi_j \phi_j} G \frac{\partial F}{\partial \phi_j}\right) \quad (j = 1, 2, 3), \quad (5.46)$$

where

$$D_{\phi_j \phi_j} = D_{ii} \left(\frac{\partial \phi_j}{\partial i}\right)^2 \quad (i = \mu, J, \Phi), \quad (5.47)$$

and

$$F = F(\phi_1, \phi_2, \phi_3; t). \quad (5.48)$$

5.3.4 Radial Diffusion

Field fluctuations on a time scale comparable to the azimuthal drift time around the earth can violate the third adiabatic invariant Φ but preserve the μ and J invariants. This is the limit of pure radial diffusion. To study this process requires knowledge of the diffusion coefficient, sources, and losses. It is convenient to use the dipole L-shell coordinates defined through

$$\Phi = 2\pi R_E^2 \frac{B_E}{L}, \quad (5.49)$$

where $B_E \approx 0.312$ G is the equatorial B-value at the surface of the earth where L = 1.

In this case the Jacobian coordinate transformation is just

$$G(L; \Phi) = \frac{\partial \Phi}{\partial L} = -2\pi R_E^2 B_E \frac{1}{L^2}, \quad (5.50)$$

and the pure radial diffusion equation becomes

$$\frac{\partial f}{\partial t} = L^2 \frac{\partial}{\partial L} \left[D_{LL} L^{-2} \frac{\partial f}{\partial L}\right] + \underline{S} - \underline{L}, \quad (5.51)$$

where $\underline{S}$ and $\underline{L}$ represent particle source and loss functions. D_{LL} is the pure radial diffusion coefficient at constant μ and J values. It has been estimated that

$$D_{LL} \simeq D_{LL}(\alpha_0) = D_{LL} \left(\frac{\pi}{2}\right) \bar{d}(\alpha_0) \quad (5.52)$$

where $\bar{d}(\alpha_0)$ is a function only of the particle equatorial pitch angle and $D_{LL} = D_{LL} \left(\frac{\pi}{2}\right)$ is the radial diffusion coefficient for equatorially mirroring $\left(\alpha_0 = \frac{\pi}{2}\right)$ particles where $\bar{d} \left(\frac{\pi}{2}\right) = 1$. For a description of $\bar{d}(\alpha_0)$ see Schulz [1975a].

Both geomagnetic and geoelectric field fluctuations contribute to D_{LL}. For geomagnetic fluctuations it can be shown that

$$D_{LL}^{(M)} (\mu, L) = \omega_d^2 \bar{P}^{(M)} (\omega_d) L^{10} \quad (5.53)$$

where $\bar{P}^{(M)}$ is the fluctuation power spectral density evaluated at the azimuthal angular drift frequency $\omega_d = \frac{V_d}{LR_E} = \frac{2\pi}{t_d}$. Empirically $\bar{P}^{(M)} (\omega) \propto \omega^{-r}$ where the value of r most often is $r = 2 \pm 1$. When r=2, one obtains the very simple expression

$$D_{LL}^{(M)} = K^{(M)} L^{10} \quad (5.54)$$

where $K^{(M)}$ is a factor dependent on the fluctuation magnitudes. For geoelectric field fluctuations it can be shown that

$$D_{LL}^{(E)} (\mu, L) = \frac{c^2}{8B^2} \sum_{n=0}^{\infty} \bar{P}_n^{(E)} (\omega_d) L^6 \quad (5.55)$$

where $\bar{P}_n^{(E)}$ is the n-th spatial Fourier component of the electric field power spectral decomposition. For details, see Fälthammar [1968], and Cornwall [1968].

The actual calculation of $D_{LL}^{(E)}$ is fairly complicated and the reader is referred to the research literature. However, for typical substorm conditions Cornwall [1972] derived the simple relation

$$D_{LL}^{(E)} = K^{(E)} \frac{L^{10}}{L^4 + (\mu_M/Z_i)^2}, \qquad (5.56)$$

where μ_M is the magnetic moment in MeV/G and Z_i is the particle charge state number.

Both $K^{(M)}$ and $K^{(E)}$ are dependent on the geophysical activity. Likely values of $K^{(M)}$ fall in the range 2×10^{-10} to 2×10^{-8} (L-shells)^2 per day and $K^{(E)}$ may be found in the range 10^{-6} to 10^{-4} (L-shells)^2 per day. The total radial diffusion coefficient is then

$$D_{LL} = D_{LL}^{(M)} + D_{LL}^{(E)}. \qquad (5.57)$$

It should be emphasized that the relations in Equations (5.54) and (5.56) represent simplified considerations that may not always be realized. If, for example, $\overline{P}^{(M)}$ or $\overline{P}^{(E)}$ do not follow ω^{-2} dependences, then $D_{LL}^{(M)}$ will involve dependence on μ, and $D_{LL}^{(E)}$ may have a different form.

5.3.5 Pitch Angle Diffusion

The presence of plasma and electromagnetic waves in the radiation belts implies fast low-amplitude field fluctuations, and some of these waves (such as the ELF whistler mode) can violate the first adiabatic invariant μ. These fast fluctuations will, in principle, also violate Φ and J; however, for these adiabatic invariants the effect is likely to be at least in part averaged out. It is convenient to convert from μ to equatorial pitch angle coordinates

$$\mu = \frac{p^2 L^3 \sin^2\alpha_o}{B_E} \qquad (5.58)$$

whereby the applicable Jacobian is

$$G(\alpha_o; \mu) = \frac{\partial \mu}{\partial \alpha_o} = \frac{p^2 L^3 \sin 2\alpha_o}{B_E} \qquad (5.59)$$

at constant particle momentum. In the pure pitch angle diffusion limit $|p|$ is unchanged and only the particle *direction* of motion changes.

The pure pitch angle diffusion equation becomes

$$\frac{\partial f}{\partial t} = \frac{1}{\sin 2\alpha_o T(\alpha_o)} \frac{\partial}{\partial \mu} \left[\overline{D}_{\alpha_o\alpha_o} \sin 2\alpha_o T(\alpha_o) \frac{\partial f}{\partial \alpha_o} \right]$$
$$+ \underline{S}^* - \underline{L}^* \qquad (5.60)$$

where $\underline{S}^*$ and $\underline{L}^*$ are the source and loss functions appropriate for the pitch angle diffusion process. $\overline{D}_{\alpha_o\alpha_o}$

is the bounce averaged pure pitch angle diffusion coefficient related to the local pitch angle diffusion coefficient $D_{\alpha\alpha}$ by

$$\overline{D}_{\alpha_o\alpha_o} = \frac{1}{\tau_b} \int_0^{\tau_b} D_{\alpha\alpha} \left(\frac{\partial \alpha_o}{\partial \alpha}\right)^2 dt. \qquad (5.61)$$

The actual calculation of $\overline{D}_{\alpha_o\alpha_o}$ from observed plasma wave distributions in the magnetosphere is quite complicated. The reader is referred to the research literature [Lyons et al., 1971, 1972; Retterer et al. 1983 and references therein].

In general, pitch angle diffusion can come about by violation of μ only (that is change in $p_\perp$) by violation of J only (change in $p_\parallel$), or by a combined violation of both μ and J. The pure pitch angle diffusion limit is ideally realized when both μ and J are violated so that the ratio of $p_\perp/p_\parallel$ changes while $|p|$ remains almost constant. When this happens, there is essentially no energy exchange between waves and particles. Physically, this can mean that the principal interaction is between the particle and the magnetic field of the wave.

5.3.6 Energy Diffusion

Particles can become energized when interacting with waves (wave damping) or can lose energy to the waves (wave instability). One may write a pure energy diffusion equation in the form

$$\frac{\partial f}{\partial t} = G^\dagger \frac{\partial}{\partial \epsilon} \left[D_{\epsilon\epsilon} G^\dagger \frac{\partial f}{\partial \epsilon} \right] + S^\dagger - L^\dagger. \qquad (5.62)$$

However, such an equation has not been used much in radiation belt physics, since almost inevitably α_o also changes. The more general case of coupled energy and angular diffusion and the associated diffusion coefficients needs further research. For information relating to such coupled processes, see Schulz and Lanzerotti [1974].

5.4 LOSS MECHANISMS

Energetic particles residing in the radiation belts are subject to collisional interactions with coexisting particle populations. The most important of these are the earth's main atmosphere, the atomic hydrogen exosphere, and the plasmasphere. Near the earth (that is, at very low L-shells or for small equatorial pitch angles) such collisions constitute a dominant energetic particle loss mechanism. But even in the central parts of the radiation belts Coulomb collisions and charge exchange can be quite significant. Pitch angle scattering of particles into the atmospheric bounce loss cone (where particle-particle collisions are dominant) is also of great significance, especially for radiation belt electrons.

5.4.1 Exosphere

The terrestrial exosphere (or geocorona) is a continuation of the atmosphere to great altitudes where collisions are infrequent and the constituents follow ballistic trajectories. The principal constituent is thought to be atomic hydrogen with a density ranging from $\sim 10^4$ atoms/cm^3 at 10^3 km altitude to $\sim 10^2$ atoms/cm^3 at 3×10^4 km altitude. Table 5-1 gives the mean atomic

Table 5-1. Number density of neutral hydrogen at the equator for an exospheric temperature of 950 K and for average geomagnetic conditions [Tinsley, 1976].

T = 950 K			
L-Shell	[H] (1/cm^3)	L-Shell	[H] (1/cm^3)
1.1	15000.	1.5	16000.
2.0	3700.	2.5	1500.
3.0	800.	3.5	470.
4.0	300.	4.5	210.
5.0	148.	5.5	120.
6.0	98.	6.5	83.

hydrogen number density [H] as function of L-shell at the equator [for example, Tinsley, 1976] and it is thought to be an average representation for an exospheric temperature of ~ 950 K. The exospheric temperatures and densities will of course change with solar and geomagnetic activity.

Also overlapping the radiation belts is the terrestrial plasmasphere consisting of thermal ions and electrons and contained within an L-shell range roughly below about L-4 to 6 by the effect of the corotational electric field of the earth. Figure 5-11 shows the electric equipotential lines in the equatorial plane formed by the combination of the corotational electric field and the solar wind induced dawn-dusk "convection" electric field. The separatrix between closed (around the earth) and open equipotential lines is related to the static plasmapause, although in a dynamic, time variable situation no simple relation between the two exists. Empirically, there is a much higher density of cold (1000 – 10 000 K) plasmaspheric particles below the plasmapause than beyond it. Based on data deduced from ducted VLF wave propagation experiments, Cornwall [1972] estimated the following average plasmaspheric particle densities:

$$[e] = 250 \ (L/L_0)^K \ cm^{-3} \ for \ L \le L_0$$

$$(5.63)$$

$$[e] = \ 13 \ (L/L_0)^K \ cm^{-3} \ for \ L > L_0$$

where $L_0 \approx 4.1$ and $K \approx 4.64$.

It is well known that the plasmasphere deviates frequently and strongly from this functional form. It is

nevertheless thought that this formula represents average long-term cold plasma densities appropriate for long-term steady state radiation belts studies. Further improvement, including storm and substorm variability, will be needed when time dependent radiation belt models are developed.

5.4.2 Coulomb Collisons

Coulomb collisions are inelastic interactions between charged particles. A radiation belt particle "colliding" with an exospheric neutral hydrogen atom, for example, will interact with the internal atomic electric field whenever the impact parameter is less than the atomic radius, or with the electric field from a thermal (plasma) proton or electron out to the particle's Debye shielding distance. The encounter will result in energy transfer from the energetic (incident) particle, and in deflection (angular scattering) of both particles. Changes in ionization states of either or both particles can also occur. On the average, angular scattering is important for radiation belt electrons, but usually not so important for the much heavier radiation belt ions. The collisional scattering process is qualitatively illustrated in Figure 5-13.
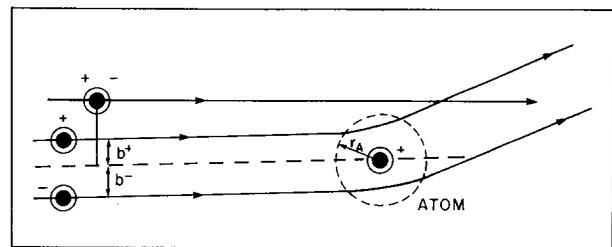

Figure 5-13. Deflection of a positive and negative particle in the internal atomic electric field of the target atom. b$^+$ and b$^-$ are impact parameters and r_A is the atomic radius. If the impact parameter is greater than r_A, no interaction occurs. For plasma particles r_A is replaced by the Debye shielding distance λ_D.

Radiation belt particles are much more energetic than exospheric particles and energy is transferred from the energetic ion to the atomic bound electron(s) or plasma electrons. The changes in the energy spectrum and directional characteristics of particles traversing a material substance whose effective thickness is greater than the collision mean free path is a difficult mathematical problem. Great simplification is, however, obtained when the differential collision cross sections are small enough to overwhelmingly favor very small energy losses and directional changes in each collision. Fortunately, this is true for Coulomb collisions in which the classical Rutherford cross section is valid. See Rossi and Olbert [1970] or Jackson [1975] for details.

One finds that the average energy loss rate for an

energetic particle passing through a gas of atomic particles is given by

$$\frac{d\epsilon}{dt} = -4Z_i^2 \; Z_t \; [n] \; r_e \; (m_e c^3 / \beta) \; F(\beta, Z_t) \qquad (5.64)$$

where Z_i is the net charge state number of the incident particle, Z_t is the nuclear charge number of the target gas atoms, m_e is the electron mass, r_e is the classical electron radius, c is the speed of light, $\beta = V/c$ and $F(\beta, Z_t)$ is a slowly varying function determined quantum mechanically by

$$F(\beta, Z_t) = -2.9 + \ln\left[\pi^2 m_e^2 c^4 / (1-\beta^2)^{3/2} \; I^2(Z_t)\right]$$

for energetic electrons, (5.65)

and

$$F(\beta, Z_t) = -2\beta^2 + \ln\left[4 m_e^2 c^4 \beta^4 / (1-\beta^2)^2 \; I^2(Z_t)\right]$$

for energetic ions (5.66)

where $I(Z_t) = 13.5 \; Z_t$ (in eV) is an approximate value of the ionization potential for the gas atoms [Rossi and Olbert, 1970].

Let $f = f(\mu, J, \Phi; t)$ denote the distribution function for equatorial radiation belt particles. The changes due to stochastic energy loss from the energetic particles can be described by

$$\left(\frac{\partial f}{\partial t}\right)_{\text{Coulomb}} = -\frac{\partial}{\partial \mu} (<\Delta\mu/\Delta t> f) - \frac{\partial}{\partial J} (<\Delta J/\Delta t> f),$$

(5.67)

and the stochastic time average $<\Delta\mu/\Delta t>$ and $<\Delta J/\Delta t>$ are then simply given by

$$<\Delta\mu/\Delta t> = \left(\frac{\partial \mu}{\partial \epsilon}\right)\left(\frac{d\epsilon}{dt}\right) \qquad (5.68)$$

and

$$<\Delta J/\Delta t> = \left(\frac{\partial J}{\partial \epsilon}\right)\left(\frac{d\epsilon}{dt}\right). \qquad (5.69)$$

Cornwall [1972] noted that it is possible to treat the slowly varying logarithmic term in the expression for $\frac{d\epsilon}{dt}$ as an approximate constant. By including contributions from energetic particle plasma electron collisions as well as from energetic particle exospheric atom collisions, one derives the expression valid for equatorially mirroring ($\alpha_0 = \pi/2$) particles:

$$\left(\frac{\partial f}{\partial t}\right)_{\text{Coulomb}} = G_C(L) \; \mu^{-1/2} \left(\frac{\partial f}{\partial \mu}\right) \qquad (5.70)$$

The Coulomb collision loss factor is given by

$$G_C(L) = (50 \sqrt{2} \; \pi \; e^4 \; \sqrt{m_H} \; L^{9/2} / (m_e B_E^{3/2})) \; [H] \; Z_i^2$$

(5.71)

where $m_H = 1.67 \times 10^{-24}$ grams is the hydrogen atom mass and $e = (4.80286 \pm 0.00009) \times 10^{-10}$ esu is the unit charge. Z_i is the ionic charge state number for incident energetic ions [Cornwall, 1972; Spjeldvik, 1977]. For a fuller treatment of the collisional process the reader is referred to the treatise by Mott and Massey [1952] or Rossi and Olbert [1970].
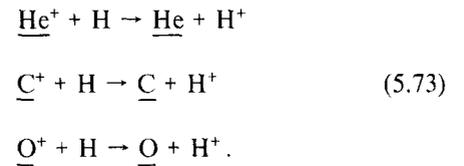
5.4.3 Charge Exchange

Collisional encounters may also change the ionization state of the colliding particles. This may entail ionization of the "target" atom and/or alteration of the net ionic charge of the incident particle. The latter is of importance for radiation belt ions since almost all of the physical processes depend directly on their charge state. The simplest of the charge exchange reactions is the one that neutralizes radiation belt protons (H):

$$\underline{H}^+ + H \rightarrow \underline{H} + H^+ \qquad (5.72)$$
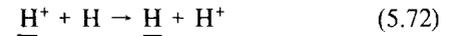
where underlying denotes energetic particles. The above reaction is an example of the electron capture process in which the incident proton picks up (or captures) the orbital electron from the thermal hydrogen atom, which then becomes a low energy proton. Once neutralized, the incident proton (now fast neutral hydrogen) is no longer subject to the magnetic deflecting force and escapes from the trapping region. Macroscopically these events occur at random, and fast neutral atoms thus exit the radiation belts in all directions. Since the speed of these particles greatly exceeds the earth's gravitational escape speed, many disappear to outer space. Some of these fast neutral atoms move towards the earth where they produce secondary interactions upon entering the atmosphere.

In a similar manner, other singly charged ions can be neutralized in such collisions:

$$\underline{He}^+ + H \rightarrow \underline{He} + H^+$$

$$\underline{C}^+ + H \rightarrow \underline{C} + H^+ \qquad (5.73)$$

$$\underline{O}^+ + H \rightarrow \underline{O} + H^+ .$$

These newly generated thermal hydrogen ions (protons) make a contribution to the earth's plasma envelope; however, their rate of formation is probably less than the rate at which such ions are supplied from the topside

ionosphere. One may note that the total charge is conserved in the radiation belts under the charge exchange reactions.
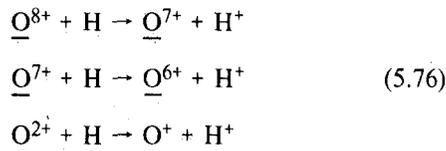
There is also another class of ion charge exchange; this results from electron stripping reactions by which the energetic ions (necessarily heavier than hydrogen) lose one or more of the remaining bound electrons. For example, there is a finite probability that an ion (say O^+) in a collision with a thermal hydrogen atom loses several of its electrons:

$$O^+ + H \rightarrow O^{5+} + H^+ + 4e^- \qquad (5.74)$$
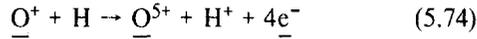
In this example four electrons are stripped off. Whether the fast O^+ ion actually loses one or more of its electrons or captures one from the hydrogen atom strongly depends on the energy of the incident ion and the details of the collision. Since this type of reaction preserves a non-zero ionic state, the ion remains trapped within the radiation belts. For this reason one distinguishes between "internal" charge exchange reactions such as the stripping reactions:

$$O^{2+} + H \rightarrow O^{3+} + H + e^-$$
$$\qquad\qquad\qquad\qquad (5.75)$$
$$O^{3+} + H \rightarrow O^{7+} + H + 4e^-$$
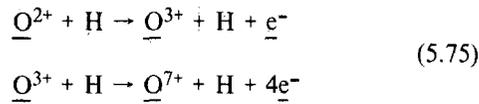
with their reverse reactions such as

$$O^{8+} + H \rightarrow O^{7+} + H^+$$
$$O^{7+} + H \rightarrow O^{6+} + H^+ \qquad (5.76)$$
$$O^{2+} + H \rightarrow O^+ + H^+$$

on one hand, and reactions that produce immediate particle loss (lowest charge state to neutral) noted above on the other. Notice also that to become neutralized, an O^{8+} ion requires a minimum of eight separate collisions with hydrogen atoms (since only one electron may be captured in each collision). This should be contrasted with electron stripping reactions in which the multiple charge state changes occur in a single collisional encounter. The principal features of the charge exchange chemistry are illustrated in Figure 5-14.

The probability that a given charge exchange process actually takes place in a collision is expressed as a reaction cross section. Such cross sections derive from laboratory studies of collision processes; however, for many ions the pertinent cross sections have not yet been measured over a sufficiently large range of particle energies. Figure 5-15 shows the cross sections for the charge exchange of protons incident on atomic hydrogen from a compilation by Spjeldvik [1977]. Notice that the charge exchange cross section is quite high $(\sigma_{10}^P > 10^{-15}$ cm$^2)$

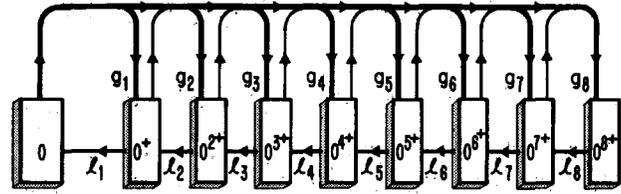below about 20 keV, but falls off sharply with higher energies.

Figure 5-14. Flow diagram for energetic oxygen ion charge exchange. This figure illustrates that while multiple charge state increases are possible in a single encounter, only single step charge state reductions can occur in a hydrogen atom gas. Oxygen ions in lower charge states may be further ionized (through single or multiple electron stripping) in single collisional encounters with the exospheric gas atoms. The ions may lose net charge in collisions by capturing the bound electron from a thermal hydrogen atom. To become neutralized, a fully ionized oxygen ion requires a minimum of eight separate collisions.
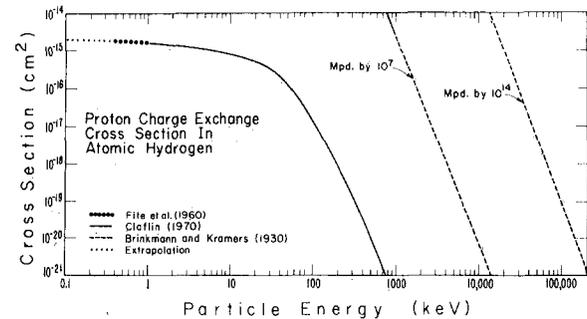

Figure 5-15. Proton charge exchange cross section as function of proton energy. It is worth noting that this cross section is high ($\sigma 10^P \sim 10(^{-15})$ cm^2) below a few tens of keV causing short proton lifetimes at those energies, and it falls off rapidly towards higher energies. The values between 0.4 and 1 keV are from the experimental work of Fite et al. [1960], the data from 1 keV are due to a compilation by Claflin [1970], and above 1000 keV the theoretical results from Brinkmann and Kramers [1930] have been used [Spjeldvik, 1977].

For ions heavier than protons, multiple potential charge states are available. For helium ions, one must consider not only the cross section for the neutralization reaction but charge state changes: state 1 → state 2 and state 2 → state 1 as well. Thus, for helium there are three important cross sections to be included. A point worth noting is that the process transforming He^+ to He^{2+} dominates over the charge state reducing reactions in the high energy part of the radiation belts, essentially above 800 keV. This is explicitly depicted in Figure 5-16 which shows the three charge exchange cross sections for radiation belt helium ions.

Charge exchange cross sections for the heavier ions such as carbon and oxygen have been measured over a small fraction of the radiation belt energy range. The situation is particularly severe for carbon ions where
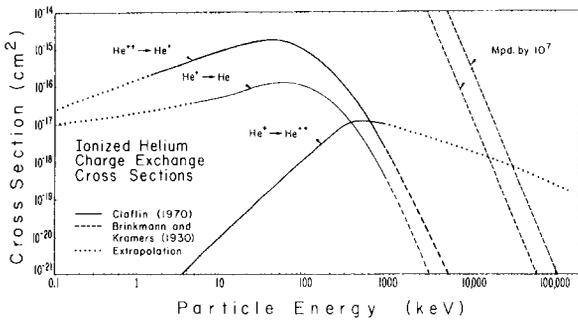
Figure 5-16. Helium ion charge exchange cross section as function of energy. Solid lines show the values compiled by Claflin [1970] from many experiments, and the dotted lines are extrapolations. The dashed lines are computed from the theoretical work of Brinkmann and Kramers [1930]. The three pertinent charge exchange cross sections are: $He^+ \rightarrow$ He (ion neutralization), $He^{2+} \rightarrow He^+$ and $He^{2+} \rightarrow He^+$. The extrapolated curve above 1000 keV (for $He^+ \rightarrow He^{2+}$) is progressively unreliable towards higher energies [Spjeldvik and Fritz, 1978b].

almost no measurements have been made. For oxygen ions there exist a number of measurements, but unfortunately the laboratory work used particles other than atomic hydrogen as targets. Figure 5-17 shows estimated
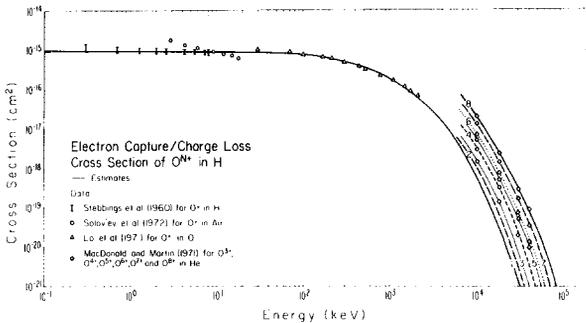

Figure 5-17. Charge exchange cross sections for (atomic) oxygen ions in an atomic hydrogen gas: Charge loss/Electron capture cross sections $O^{i+} \rightarrow O^{(i-1)+}$ estimated from sparse available data. Stebbings et al. [1960] give data with H-targets up to 8 keV, Lo et al. [1971] give data with O-targets and MacDonald and Martin [1971] give data with He-targets. Also shown are results with rarefied air-targets [Solov'ev et al., 1972]. The cross sections for reactions with i>1 have not been measured below ~ 10 MeV [Spjeldvik and Fritz, 1978a].

ion charge loss (electron capture) cross sections based on a compilation of a number of measurements using H, air and O as target particles [Spjeldvik and Fritz, 1978a]. Estimates of the charge gain (electron loss) cross sections have been made from limited data available. Examples are illustrated in Figure 5-18. For the remaining reactions between the multiple charge states, no laboratory measurements have been reported, and one must use crude estimates [Spjeldvik and Fritz, 1978a].

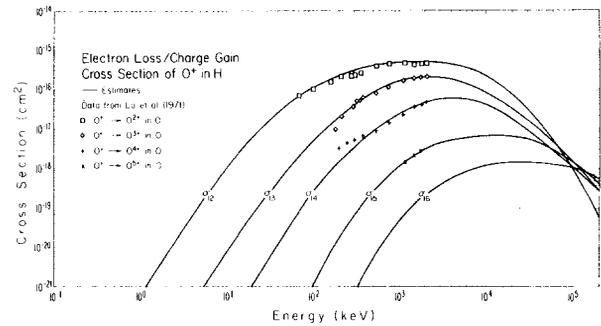The mathematical description of the effects of the

Figure 5-18. Charge exchange cross sections for (atomic) oxygen ions in an atomic hydrogen gas: Charge gain/Electron loss cross sections $O^+ \rightarrow O^{(1+j)+} + j\,e$. The data shown are from Lo et al., [1971] for O-targets. The solid lines are crude estimates made by Spjeldvik and Fritz [1978a]. More reliable cross sections for oxygen ions and other heavy ions need to be established.

charge exchange processes on radiation belt ion distribution functions is through loss and gain terms. For radiation belt protons one has the expression

$$\left(\frac{\partial f}{\partial t}\right)_{\text{Charge Exchange}} = -\Lambda_{10}\, f \qquad (5.77)$$

since the loss rate is proportional to the number of protons present (or more precisely, the distribution function f), and also proportional to the factor $\Lambda_{ij} = <V\sigma_{ij}\,[H]>$ where V is the ion speed and σ_{ij} the charge exchange cross section for transformation state $i \rightarrow$ state j. To describe the heavier ions where more than one charge state applies, one considers a distribution function for each charge state. For helium ions, let f_1 and f_2 be the distribution functions for He^+ and He^{2+} ions respectively. The charge exchange processes are then represented by

$$\left(\frac{\partial f_1}{\partial t}\right)_{\text{Charge Exchange}} = -\Lambda_{10}\, f_1 + \Lambda_{21}\, f_2 - \Lambda_{12}\, f_1$$
$$(5.78)$$

$$\left(\frac{\partial f_2}{\partial t}\right)_{\text{Charge Exchange}} = -\Lambda_{21}\, f_2 + \Lambda_{12}\, f_1 \qquad (5.79)$$

and this provides a coupling between the distribution functions.

In general, for an ion species with s available charge states one obtains charge exchange expressions of the form

$$\left(\frac{\partial f_i}{\partial t}\right)_{\text{Charge Exchange}} = -\sum_{j=0}^{s} \Lambda_{ij} f_i + \sum_{j=1}^{s} \Lambda_{ji} f_j \qquad \text{for } i \neq j,$$
$$(5.80)$$

and when the exosphere predominantly consists of

atomic hydrogen (as in the case of the earth) the first summation contains contributions from $j = i - 1$ only.

5.4.4 Wave-Particle Interactions

Plasma waves play an important role in radiation belt physics. Different conditions for wave propagation, growth and decay in the magnetosphere have led to delineation into numerous *wave modes*. For a detailed classification of these modes see Stix [1962] or Kennel et al. [1979]. In a previous section, the radiation belt transport equation was given; here we shall outline some of the concepts concerning the interactions.

Angular scattering can result from interactions with electromagnetic waves. As an example, consider gyro (or cyclotron) resonance: a radiation belt particle spiraling around a magnetic line of force (the guiding center locus field line) will gyrate at a rate determined by the magnetic field strength, mass, and charge of the particle. An electromagnetic wave (with electric and magnetic wave vectors) also propagating along that field line will rotate according to its wave frequency. When both the sense of rotation and the rotation frequency match for both wave and particle, the particle will be subject to an essentially constant "wave" field for the duration of the encounter. The particle can exchange energy with the wave through the electrical interaction and/or deflection can occur through the magnetic interaction. Higher order resonances can also take place, for example, if the rotation rates differ by a factor of two. When the particle-wave interaction is primarily via the magnetic wave vector (as in the case of the radiation belt electron – whistler mode hiss wave interaction) the result is primarily angular scattering; this is the pure pitch angle scattering limit. Other resonances including bounce resonance and drift resonance can also be important.

These waves in the radiation belts may remain in the area where they were generated (very small group velocity) or propagate afar (large group velocity). They have frequency and wave length, and there are different polarization properties. Propagation properties are determined by a dispersion relation [Stix, 1962] that in part depends on the density of the plasma in which the wave exists and the geomagnetic field. Stability or instability of the waves is frequently determined by the energetic particles with which the waves can interact.

Plasma waves are said to be unstable to growth if interactions with the charged particles transfer energy to the waves; if the transfer is from the waves to the particles the waves are said to be damped. If plasma waves interact with radiation belt particles in such a way as to have their principal interactions locally, then it is possible to self-consistently give a theoretical treatment of both wave and particle properties. On the other hand, if the waves have significant spatial propagation so that they, for example, gain energy from one particle population

and propagate to interact further with another particle population elsewhere, then the latter process is termed "parasitic". Both types of processes are of major significance in the radiation belts.

5.4.4.1 Pitch Angle Scattering Into the Loss Cone.
Interactions between energetic particles and plasma waves can significantly affect the trapped particle population's energy and angular distribution. If the pitch angle is altered so that the particle finds itself within the atmospheric bounce loss cone, it will have a high probability of becoming lost upon entering the atmosphere. For ions this probability is virtually 100% while for energetic electrons a certain fraction of the precipitated particles are backscattered up into the magnetosphere only to encounter the conjugate hemisphere during the succeeding bounce motion.

The directional change in the angular scattering process due to plasma wave or collisional interactions is random: to lowest order it is just as likely for a single particle to be scattered from lower to higher pitch angles as in the opposite direction. However, when the particles are *anisotropically* distributed in pitch angle (for example, with $\frac{\partial f}{\partial \alpha_0} > 0$), the number of particles scattered from the higher particle density region towards the lower density region is greater than the number scattered the other way. As a consequence, the stochastic process is biased by the particle pitch angle distribution and a net *diffusion flux* occurs. This pitch angle diffusion flux is just

$$F_{\text{diff}} = -\overline{D}_{\alpha_0 \alpha_0} \sin 2\alpha_0 \, T(\alpha_0) \frac{\partial f}{\partial \alpha_0} \qquad (5.81)$$

so that the diffusive transport term in (5.45) may be written as simply

$$\left(\frac{\partial f}{\partial t}\right)_{\text{diff}} = -\frac{1}{\sin 2\alpha_0 T(\alpha_0)} \frac{\partial F_{\text{diff}}}{\partial \alpha_0} . \qquad (5.82)$$

Atmospheric particle losses within the bounce loss cone generally cause $f(\alpha_0 < \alpha_{\text{OLC}})$ to be near zero (except under conditions of extremely strong scattering). This generally favors a positive pitch angle anisotropy (loss cone distribution), and particles can be lost to the atmosphere at any L-shell due to the pitch angle scattering process. Of course, $\partial f / \partial \alpha_0$ may be negative under certain conditions, and thus net reverse diffusion can take place. Examples are an atmospheric *source cone* in the auroral zone as a consequence of auroral electric fields, effects of L-shell splitting due to the deviations from the dipolar azimuthal symmetry of the magentic field [Roederer, 1970], or particle injections during disturbed times.

Analysis of resonant wave-particle interactions violating the first adiabatic invariant have generally considered waves with frequencies near the gyro frequency of the energetic particles. The condition for resonance between waves of angular frequency ω and particles at the gyro-frequency Ω is given by

$$\omega - k_\| \, v_\| = n \, \Omega; \; n = 0, \pm 1, \pm 2, \pm 3, \ldots \; [\text{Lyons, 1979}], \tag{5.83}$$

where $k_\|$ and $v_\|$ are the parallel (to **B**) wave vector and particle velocity respectively. For a given wave mode there is a dispersion relation linking ω and **k**. The *cyclotron harmonic resonances* have the (Doppler shifted) wave frequency equal to a harmonic ($n = \pm 1$, $n = \pm 2$, $n = \pm 3$, ...) of the particle gyrofrequency, and the classical *Landau resonance* ($n = 0$) has the wave parallel phase velocity $v_\| = \omega/k_\|$. All these resonances result in particle diffusion in both energy and equatorial pitch angle α_0.

The Landau resonance results in diffusion solely in $v_\|$, conserving $v_\perp$. Thus the pitch angle change $\Delta\alpha$ at a given location along the particle trajectory is related to the parallel velocity change $\Delta v_\|$ by

$$\Delta\alpha = -\frac{\sin^2\alpha}{v_\perp} \, \Delta v_\|. \tag{5.84}$$

The cyclotron harmonic resonance can likewise produce pitch angle changes resulting from the energy exchange, or the interaction can be primarily with the magnetic wave vector causing pitch angle scattering more directly with little energy exchange. The latter process is particularly important for electrons.

In general, the study of wave-particle interactions requires an extensive mathematical treatment, and the necessary derivations and analysis are beyond the scope of the present chapter. The interested reader is referred to a number of works on the subject [Stix, 1962; Sagdeev and Galeev, 1969; Lerche, 1968; Kennel and Engelman, 1966; Lyons et al., 1971, 1972; Retterer et al., 1983].

5.4.4.2 Scattering of Energetic Electrons. Pitch angle scattering is particularly important for radiation belt electrons. Here, we bypass the extensive mathematical treatment found in Lyons et al. [1971, 1972]. The different resonances are illustrated in Figure 5-19 which depicts the regions of cyclotron resonance in velocity space resulting from waves distributed over a band of parallel wave vectors $\Delta k_\|$. Resonance at each cyclotron harmonic occurs over a band of parallel velocities $\Delta v_\|$; for simplicity, relativistic effects for electrons >500 keV are not included. No cyclotron harmonic interaction occurs for $v < v_{\|\min}$, and the value of $v_{\|\min}$ depends on the actual $k_\|$ band over which the wave energy is distributed. This is locally true where the geomagnetic field may be considered uniform on the scale of the gyroradius.

REGIONS OF CYCLOTRON RESONANCE IN MOMENTUM SPACE

PITCH ANGLE $\alpha = \text{TAN}^{-1} \, P_\perp / P_\|$
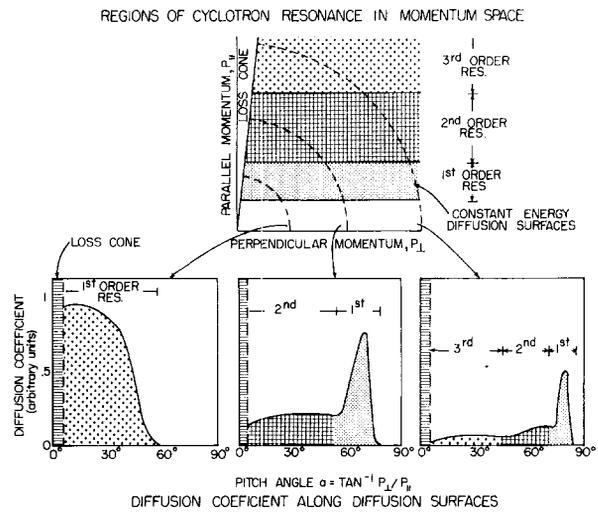DIFFUSION COEFICIENT ALONG DIFFUSION SURFACES

Figure 5-19. Radiation belt electron ELF whistler mode wave interactions: Regions of cyclotron resonance in momentum space. Upper panel shows the effects of pure pitch angle diffusion (conserving electron energy) for the resonance with plasmaspheric ELF whistler mode turbulence. Lower panels show the effect upon progressively more energetic electrons, and that for the most energetic electrons the high order resonances become increasingly important as the electrons diffuse in pitch angle towards the atmospheric bounce loss cone. The resulting pitch angle diffusion coefficient thus becomes a strong function of pitch angle [Lyons et al., 1972].

The earth's magnetic field is, however, quite inhomogeneous when considered in its totality, and the wave energy is, in general, unevenly distributed over the space of the radiation belts. During the particle bounce motion, as the particles move away from the geomagnetic equator along its trajectory, the increasing magnetic field strength causes both particle pitch angle and parallel velocity to change. The increase in the local pitch angle as a particle moves away from the equatorial plane (see Equation 5.10) implies that cyclotron resonance can occur for all equatorial parallel particle energies greater than a minimum value $E_{\|\min}$.

Figure 5-20 illustrates radiation belt electron and ELF whistler mode wave propagation. The significant wave-particle interactions for energetic electrons are shown. Note that the wave propagation does not necessarily follow magnetic field lines, and therefore the particles may interact with waves generated over a significant volume of the magnetosphere. For comparison, the inner and outer radiation zones (for electrons) are indicated.

Satellite measurements have shown that a band of whistler mode waves centered around a few hundred hertz exists essentially continually within the plasmasphere. Because of the persistence and audio frequency range, this type of wave is called *hiss*. Ray tracing studies have shown that the plasmaspheric hiss can readily propagate across the geomagnetic field lines [Lyons and Thorne, 1970] and thus fill a great volume of the inner

magnetosphere with wave energy. These waves are believed to be generated in the outer regions of the plasmasphere, and within the plasmasphere the ELF hiss turbulence is the dominant wave component that interacts with radiation belt electrons. Waves that may influence trapped particles can also be generated by earth-based radio sources.
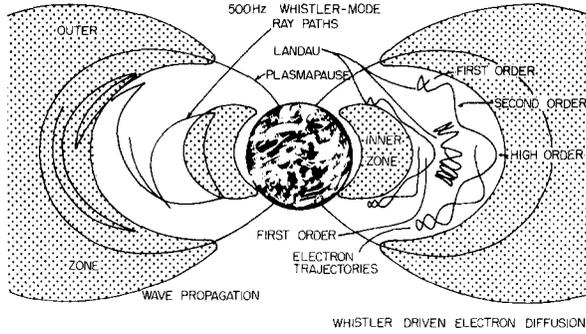

Figure 5-20. Spatial illustration of radiation belt electron wave-particle interactions. Characteristic locations for the inner and outer electron radiation zones are shaded, and the magnetic field line approximating the average plasmapause location is also indicated. Left side: 0.5 kHz whistler-mode ray paths in the radiation belts showing internal reflection and cross-L propagation characteristics [from Lyons and Thorne, 1970]. Right side: Typical energetic radiation belt electron trajectories indicating the spiral motion between the magnetic mirror points. The spatial regions where the Landau and different cyclotron resonances are most effective are noted [Lyons et al. 1972].

Based on typical observed wave characteristics, Lyons et al. [1972] calculated the pitch angle diffusion coefficient for both cyclotron and Landau resonances shown in Figure 5-21. They also computed lifetimes for energetic electrons subject to this wave-particle interaction process. An example of these lifetimes for average modeled wave parameters and a normalized wave amplitude of 35 mγ is shown in Figure 5-22. These lifetimes take on great significance in the modeling of the radiation belt electron structure and will be discussed in more detail in the modeling section.

5.4.4.3 Limit On Radiation Belt Particle Fluxes.

Plasma waves generated by radiation belt particles locally will have their growth rates in part controlled by the intensity of the trapped energetic flux of those particles in resonance with the waves. While radiation belt electrons within the plasmasphere are controlled by the parasitic type of interaction mechanisms, it has been found that the radiation belt particle fluxes beyond the plasmasphere can be effectively limited by the self-generating wave mechanism. In the following a few principal aspects of the radiation belt saturation process are outlined; for a more detailed mathematical treatment the reader is referred to Kennel and Petschek [1966] or Schulz [1975b].
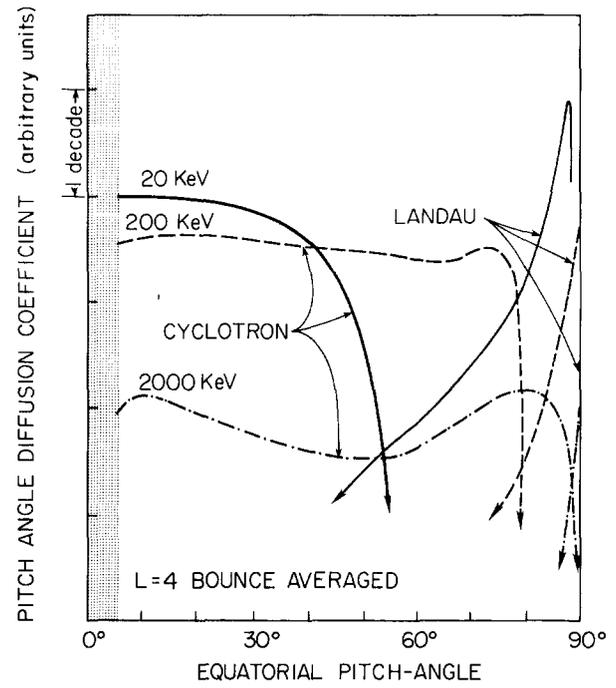
5-20

Figure 5-21. The bounce averaged electron pitch angle diffusion coefficient $D\alpha_0\alpha_0$ calculated for all cyclotron harmonic resonances and the Landau resonance. Note that at each energy there is a region of very low pitch angle diffusion (for 20 keV electrons, near 87°); this "bottleneck" in the pitch angle diffusion coefficient is the cause of the "bumps" in the actual electron pitch angle distributions giving rise to the so-called bell-shaped distributions [Lyons et al., 1972].

It has been demonstrated that there is a limiting value I' that the radiation belt integral omni-directional flux I cannot exceed without provoking a cyclotron wave instability. Schulz and Lanzerotti [1974] estimated this limit to be about I' = 10^{11} L^4 particles cm^{-3} sec^{-1} integrated over all energies and pitch angles. The linear wave growth rate is γ_g, and therefore the growth rate for wave energy is $2\gamma_g$. An incipient wave undergoes a partial reflection (reflection coefficient R $\leq$ 1) upon traveling a distance d $\sim$ L R$_E$; the remaining fraction, 1-R, of the wave is lost from the radiation belts. The time interval between wave reflections is T = L R$_E$/V$_g$ where V$_g$ = ($|d\omega/dk|$) is the group wave velocity. The condition for marginal stability is that the waves on the average do not grow further in time; that is, the decrease in the wave amplitude upon reflection is restored in one traversal between bounces:

$$R \exp\left[2\gamma_g LR_E/V_g\right] = 1. \qquad (5.85)$$

This defines the marginal growth rate to be

$$\gamma_g = (V_g/2LR_E)\,|\ln R|. \qquad (5.86)$$

If I exceeds I' (that is, if γ exceeds γ_g) the consequence is a net growth of wave energy, and the stronger waves
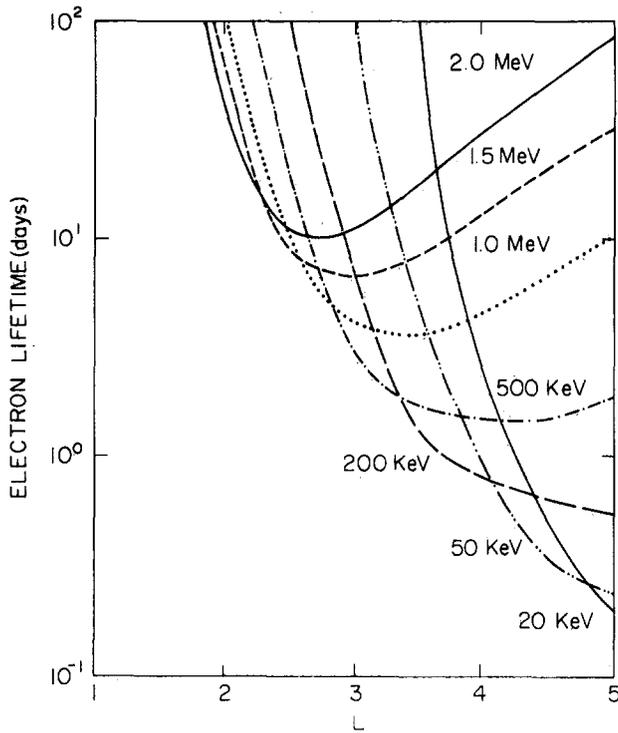
Figure 5-22. Radiation belt electron precipitation lifetimes due to electron pitch angle scattering into the atmospheric bounce loss cone. These lifetimes are given for an average whistler wave amplitude of $B_{wo} = 35$ mγ_o. Notice that there is generally a minimum in these lifetimes at each energy, and that this minimum is displaced towards lower L-shells with higher electron energy. At 2000 keV this minimum occurs at $L \simeq 2.7$ while at 500 keV it is substantially broader and occurs at $L \simeq 4.2$. This minimum electron lifetime is an important factor for the electron "slot" location defining the separation between the two radiation belts.

scatter the particles in pitch angle resulting in precipitation into the atmosphere and reduction in the particle flux until I no longer exceeds I'. If an external particle *injection source* is strong enough to more than offset this maximum loss rate then the radiation belt particle fluxes will increase beyond the stably trapped flux limit I'; this may indeed happen for impulsive sources associated with disturbed conditions. The aftermath of such an injection will, however, be a rapid reduction to the stably trapped flux intensity level.

Figure 5-23 shows a comparison of the theoretical radiation belt flux limit with data [Kennel and Petschek, 1966]. Notice that most of the time the outer radiation zone particle fluxes are just below the theoretical characteristic flux limit.

5.4.4.4 Strong Diffusion Limit. There is, however, another important limit to consider, namely the upper limit on the rate at which radiation belt particles can become lost to the atmosphere by scattering into the bounce loss cone. Consider the effect of very rapid pitch angle scattering. The particle pitch angle distribution will then become essentially isotropic; that is, the flux per
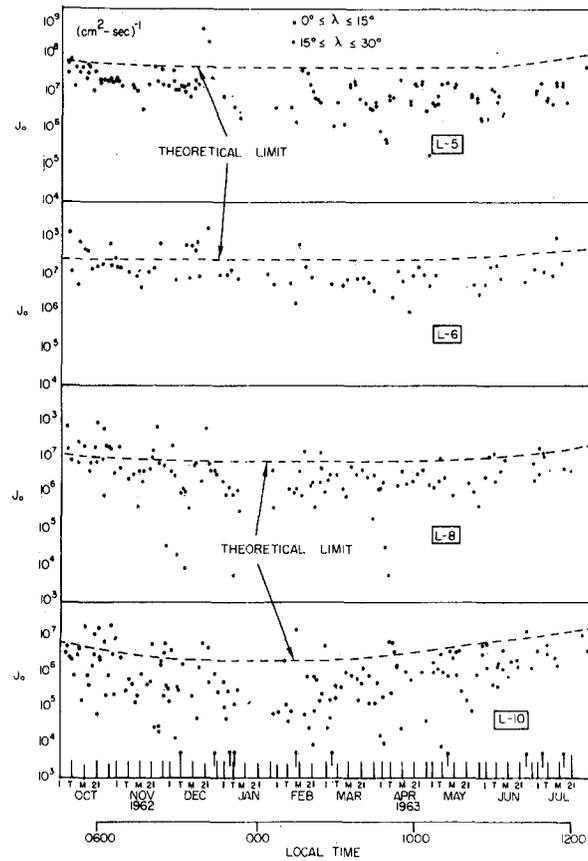

Figure 5-23. Comparison of the predicted whistler self-excitation limit with E>40 keV electron data recorded with the Explorer 14 spacecraft [Kennel and Petschek, 1966].

differential solid angle interval will be the same at all pitch angles, even within the loss cone. Within the loss cone ($\alpha_0 \leq \alpha_{OLC}$) the particles will be lost from the radiation belts on a time scale τ_b, and for the *strong diffusion limit* to be reached, the scattering mechanism must be faster than this. The solid angle of the loss cone is just $\Omega_{LC} = 2\pi(1-\cos\alpha_{OLC})$ and the maximum particle flux loss rate δ is then

$$\delta = \frac{\Omega_{LC}}{\tau_b} . \tag{5.87}$$

The only exception to this concept occurs when the loss cone becomes a source cone due to the auroral electric field parallel to the magnetic field, and a source cone distribution exiting one hemisphere can become lost through direct precipitation into the conjugate hemisphere.

5.5 THEORETICAL RADIATION BELT MODELS

Two types of radiation belt models now exist: empirical models based on compiled observations and theoretical models derived from our knowledge of radiation belt

5-21

CHAPTER 5

physics. The ideal empirical models represent the standards with which the theoretical models must be compared, and they are also useful for engineering purposes. However, they give only a smoothed statistical picture of the time period when the data were obtained, and the data collection process is subject to experimental errors and misinterpretations. Theoretical models, on the other hand, can be used to simulate and predict radiation belt behavior under a variety of conditions: quiet times, disturbed times, or magnetic storms. They can be used to study ionic species and charge state distributions for which no experimental information is available. Such models are only as valid as the physical approximation they are based on, however. In the following sections simple theoretical models are outlined.

5.5.1 Quiet Time, Steady State Models

Studies of quiet geomagnetic conditions using theoretical radiation belt models serve as an important test of our current understanding of the trapped radiation environment. It is assumed that under quiet time conditions the radiation belts can be described in terms of an equilibrium balance between sources, internal transport, and losses. Symbolically one writes

$$\frac{\partial f}{\partial t} = \left(\frac{\partial f}{\partial t}\right)_{source} + \left(\frac{\partial f}{\partial t}\right)_{transport} + \left(\frac{\partial f}{\partial t}\right)_{loss} = 0 \ . \quad (5.88)$$

The sources are considered to be located on the boundary of the trapping region (and thus describable via a boundary condition on the trapped flux for each species) as well as in the interior of the trapping region (such as the CRAND-source). The transport mechanisms are radial diffusion and pitch angle diffusion. Particle losses are caused by charge exchange ion neutralization, energy degradation, and pitch angle diffusion into the bounce loss cone. Particles diffusing outward may encounter the magnetopause and become lost from the magnetosphere. Radiation belt theoretical models constitute the combination of these processes.

5.5.1.1 Formulation of Boundary Conditions. For steady state conditions one needs in general boundary conditions on the particle distribution function f:

(1) At $L = L_{max}$ (outer boundary) one specifies the particles energy spectra and angular distributions, which defines f at the outer boundary.

(2) At $L = L_{min} = 1$ (inner boundary formed by the surface of the earth) the particle distribution function vanishes (f = 0).

(3) At $\alpha_o = \pi/2 : \partial f/\partial \alpha_o = 0$.

(4) At $\alpha_o = 0$ or $\pi : \partial f/\partial \alpha_o = 0$.

(5) At $P = P_{max}$ (or $E = E_{max}$):f = 0 where $E_{max} \gtrsim 100$ MeV.

(6) By symmetry $f(\alpha_o) \equiv f(\pi - \alpha_o)$ so that one needs to consider only the range $0 \leqq \alpha_o \leqq \pi/2$.

The complete radiation belt modeling can be simplified in a way that retains much of the essential physics but greatly simplifies the mathematics, namely separating radial diffusion from pitch angle diffusion. One treats radial diffusion for $\alpha_o = \pi/2$ particles only, and with given $f(\alpha_o = \pi/2)$ the pitch angle diffusion process at fixed L-shells only. This approach is not strictly correct when there is significant interaction between the pitch angle and radial diffusion modes, but it reduces an almost unmanageable numerical problem to cases where solutions can be found. The results should therefore be treated with some caution.

5.5.1.2 Electron Model. Radiation belt electrons are described by the diffusion equation

$$\frac{\partial f}{\partial t} = L^2 \frac{\partial}{\partial L}\left[D_{LL}L^{-2}\frac{\partial f}{\partial L}\right] + \frac{1}{\sin 2\alpha_o T(\alpha_o)}\frac{\partial}{\partial \alpha_o}\left[D_{\alpha_o \alpha_o}\right. $$

$$\left. \sin 2\alpha_o \ T(\alpha_o) \ \frac{\partial f}{\partial \alpha_o}\right] + G_e(L)\mu^{-1/2}\frac{\partial f}{\partial \mu} \ , \quad (5.89)$$

where $G_e(L)$ is the Coulomb loss term for electrons. Lyons and Thorne [1973] separated radial and pitch angle diffusion by substituting for Equation (5.71) the two equations

$$\frac{\partial f}{\partial t} = L^2 \frac{\partial}{\partial L}\left[D_{LL}L^{-2}\frac{\partial f}{\partial L}\right] - \frac{f}{\tau_w} - \frac{f}{\tau_{cc}} \quad (5.90)$$

and

$$\frac{\partial f}{\partial t} = \frac{1}{\sin 2\alpha_o T(\alpha_o)}\frac{\partial}{\partial \alpha_o}\left[D_{\alpha_o \alpha_o}\sin 2\alpha_o T(\alpha_o)\frac{\partial f}{\partial \alpha_o}\right]. \quad (5.91)$$

They solved Equation (5.91) under an assumed angular distribution preserving exponential decay conditions and obtained the lowest normal mode pitch angle distribution and electron precipitation lifetimes τ_w. Their results are shown in Figures 5-24 and 5-25 respectively. The precipitation lifetimes were calculated assuming a mean ELF Whistler mode wave amplitude of 35nT. For other wave amplitudes, these lifetimes scale as $(B_w/35m\gamma)^{-2}$.

Using these characteristic electron scattering precipitation lifetimes it is possible to solve the steady state radial diffusion Equation (5.90) for equatorially mirroring radiation belt electrons. The results are shown in Figure 5-25.

A simplification in this work was *a priori* approximation of the Coulomb collision "loss time" which was defined as $\tau_{cc} \approx \epsilon(d\epsilon/dt)^{-1}$ where $d\epsilon/dt$ is given by Equation (5.64); this is a rather crude approximation for the last term in (5.90), since τ_{cc} really depends on the distribution function itself as given by Equation (5.66).
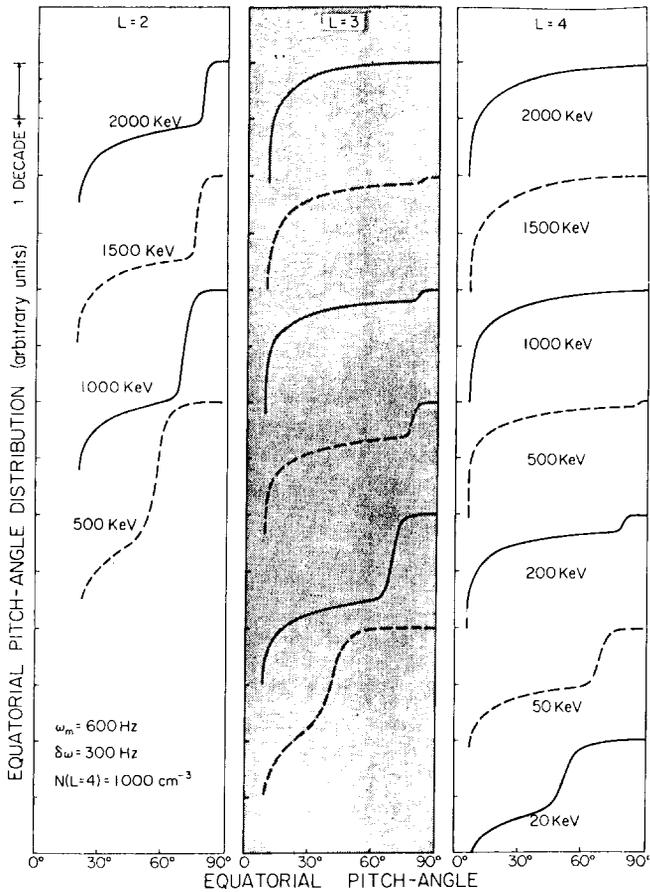
Figure 5-24. Predicted radiation belt electron pitch-angle distributions [Lyons and Thorne, 1973]. The example shown was calculated using a Gaussian ELF whistler mode hiss turbulence frequency distribution peaked at 600 Hz and with a bandwidth of 300 Hz.
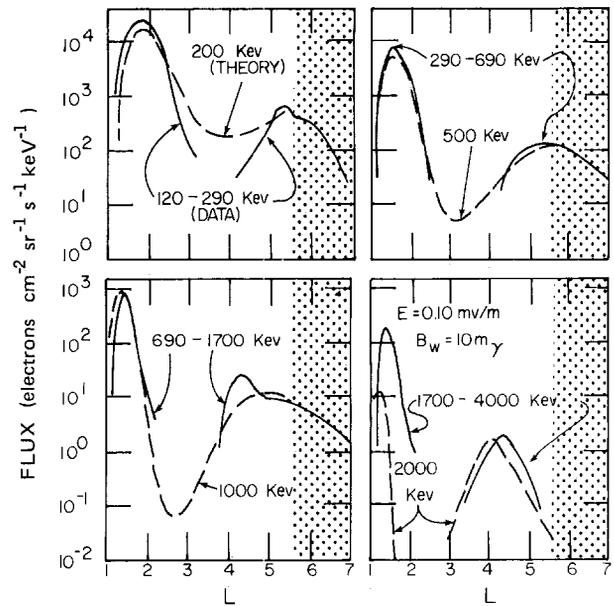

Figure 5-25. Theoretical and observed radiation belt electron radial flux distributions at the geomagnetic equator. The theoretical results (dashed curves) are calculated from radial diffusion of energetic electrons subject to pitch-angle scattering due to the (resonant) ELF whistler mode turbulence (hiss) within the plasmasphere. The data (solid lines) are taken from the OGO 5 spacecraft. Notice how well the theory simulates the location and width of the observed radiation belt separation (slot) region over a wide range of electron energies leaving essentially only the finer details of the equilibrium distribution for future investigation [Lyons and Thorne, 1973].

Much of the essential radiation belt electron physics is retained, however. Notice how well the electron slot region that separates the radiation zone into two belts is reproduced compared with actual data from the OGO-5 spacecraft, both in width and L-shell location for different energies. Perfect agreement in all details should not be expected since the theory treats average conditions based on parametrized wave characteristics, while the data are for a specific time when the recordings were made.

From such calculations we have learned that for energetic electrons, wave-particle interactions are the cause of the division into *two distinct belts*, since electrons in the "slot" region are lost to the atmosphere at a fast rate. Those few electrons that survive the cross-L transport to arrive in the inner radiation zone became very stable since the time scale for wave particle scattering is very long there.

5.5.1.3 Proton Model. Empirically, radiation belt protons are not distributed into two radiation zones. At constant proton energy there is generally a single peak in the

proton flux radial distribution and this peak is located on lower L-shells with higher proton energy. No specific wave mode has yet been identified that interacts in a dominant way with >100 keV protons below the average plasmapause location. On the other hand, protons (like all ions) are subject to the charge exchange process.

Neglecting pitch angle scattering, the radial diffusion equation for equatorially mirroring ($\alpha_0 = \pi/2$) protons may be written

$$\left(\frac{\partial f}{\partial t}\right) = L^2 \partial/\partial L \left[D_{LL} L^{-2}(df/dL)\right] - \Lambda_{10} f +$$

$$\tag{5.92}$$

$$G(L)\, \mu^{-1/2}(\partial f/\partial \mu)$$

where $\Lambda_{10} = <\sigma_{10}^P [H]\, v>$ is the charge exchange loss frequency per unit distribution function f. To simulate the steady state radiation belts (that is $\frac{\partial}{\partial t} \to 0$) this equation can likewise be solved when suitable boundary conditions are imposed. The boundary conditions are established by using a measured outer zone proton flux spectrum, and by covering an energy range sufficiently large that $f(L,\mu) \approx 0$ at $\mu > \mu_{max}$ where μ_{max} corresponds to the upper limit of the radiation belt trapping

energies considered. Figure 5-26 shows the computed
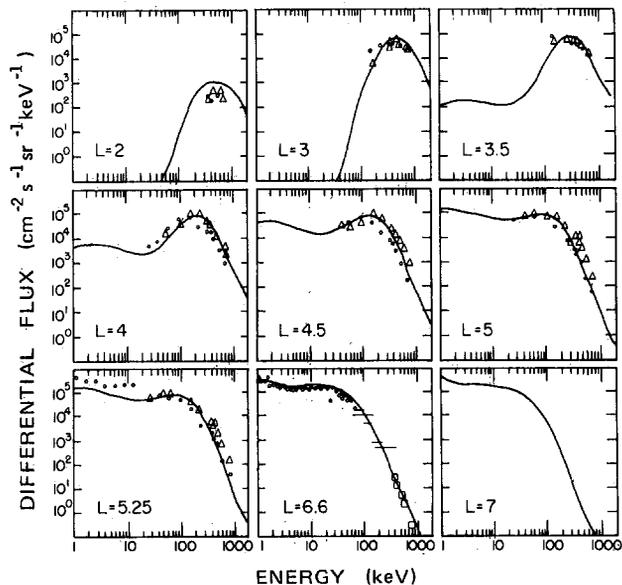

ENERGY (keV)

Figure 5-26. Radiation belt proton energy spectra obtained from a theoretical calculation based on proton radial diffusion subject to Coulomb collisions and charge exchange losses. No wave-particle interactions were considered. Boundary conditions were imposed at L-6.6 with data from the ATS-6 spacecraft, and the computed spectra at lower L-shells are compared with available equatorial data from Explorer 45. The results of the theoretical calculations below a few tens of keV energies may be inaccurate since convection processes may dominate over diffusion at these low energies [Spjeldvik, 1977].

radiation belt proton spectra obtained with this method, and data are shown for comparison (taken from Explorer 45 below L = 5.3). Notice that the spectral maximum found at L<5 generally is displaced towards higher energies with lower L-shells. The flux values computed below a few tens of keV are below radiation belt energies (convective processes also operate in that range) and should not be considered reliable. The comparison with data is quite good, however, giving support to the usefulness of the radial diffusion theory above at least 100 keV.

A complementary view of the theoretical radiation belt proton fluxes is given in Figure 5-27 which depicts the computed radial distributions for different proton energies. Qualitatively similar to the observations, the radial flux maxima are displaced towards lower L-shells with higher proton energy. On L-shells well beyond the flux radial peak location, the characteristic time scales of diffusive transport are substantially shorter than that of the loss processes. This situation is called diffusive equilibrium. There is also an important connection with the magnitude of the radial diffusion coefficient. As D_{LL} increases, the diffusive equilibrium radial range extends towards lower L-shells, and the radial peak location is found at lower L. Also, the absolute magnitude of the flux radial peak increases as D_{LL} increases. An enhanced
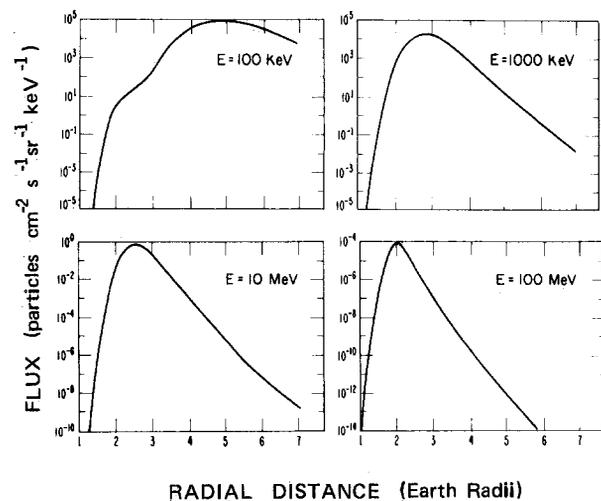

RADIAL DISTANCE (Earth Radii)

Figure 5-27. Theoretical proton radial distributions calculated from proton radial diffusion subject to Coulomb collision energy losses and charge exchange loss. Notice there is no division (or slot) within the trapping region. The curves now show that the radial flux maximum is displaced towards lower L-shells with higher proton energy. For details about the numerical calculations see Spjeldvik [1977].

D_{LL} causes a substantial increase in the trapped fluxes on L-shells below the peak flux location. Proton models that treat other than equatorially mirroring pitch angles in a comprehensive manner have not yet been developed. The reason is partially that $D_{\alpha_0\alpha_0}$ is not know for protons, and partially that solving the simultaneous proton radial and pitch angle diffusion problem subject to the simultaneous μ-variations is mathematically difficult owing to the great inhomogeneity in the coefficients.

5.5.1.4 Heavy Ion Models.
Besides electrons and protons, the earth's radiation belts contain appreciable fluxes of energetic helium, carbon, oxygen, and other ions. Theoretical modeling of these ion populations can be carried out by a generalization of the proton model. One must consider a distribution function for each charge state of a given radiation belt species, as well as the coupling between charge states imposed by the charge exchange chemistry. For *helium ions* one may write the coupled equations for equatorially mirroring ions:

$$\left(\frac{\partial f_1}{\partial t}\right) = L^2 \partial/\partial L \left[D_{LL_1}L^{-2}(\partial f_1/\partial L)\right] +$$

$$(5.93)$$

$$G_1(L) \; \mu^{-1/2}(\partial f_1/\partial \mu) - \Lambda_{10}f_1 + \Lambda_{21}f_2 - \Lambda_{12}f_1$$

and

$$\frac{\partial f_2}{\partial t} = L^2 \partial/\partial L \left[D_{LL_2}L^{-2}(\partial f_2/\partial L)\right] +$$

$$(5.94)$$

$$G_2(L) \; \mu^{-1/2}(\partial f_2/\partial \mu) - \Lambda_{21}f_2 + \Lambda_{21}f_1$$

where the subscripts indicate the ion charge state.

These equations have also been solved numerically [Cornwall, 1972; Spjeldvik and Fritz, 1978a], and some of the findings are illustrated in Figure 5-28. Notice that
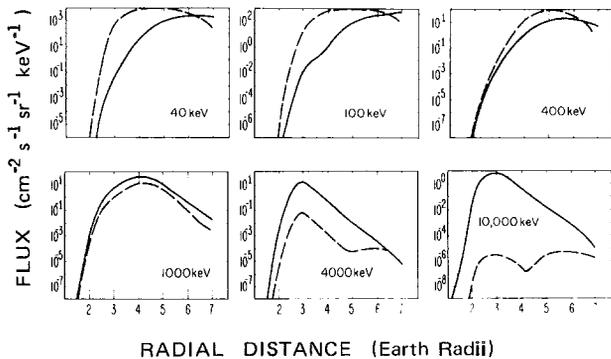

RADIAL DISTANCE (Earth Radii)

Figure 5-28. Theoretical helium ion radial distributions calculated from radial diffusion theory with Coulomb collisions and charge exchange. Solid curves show equatorially mirroring fluxes of He^{++} while the dashed curves depict He^+. Notice that He^+ is dominant below $\sim$ 1 MeV while He^{++} is dominant at higher energies [Spjeldvik and Fritz, 1978].

there is a transition from charge state 1 (He^+) to the state 2 (He^{2+}) at energies around 1 MeV, so that the lower charge state of helium ions is most abundant at the lower energies and the higher charge state at the higher energies. The spectral features computed for helium ions below $\sim$1 MeV stem from the energy dependence of the radial diffusion coefficient D_{LL} and the loss rates. These have yet to be verified or refuted by observations.

For even heavier ions a multitude of charge states are available to the radiation belt heavy ions: for carbon ions there are six positive charge states, and for oxygen ions there are eight. In general, for a given ion charge state of an elemental species with s available states, the radial diffusion equation for equatorially mirroring ions may be written

$$\frac{\partial f_i}{\partial t} = L^2 \partial/\partial L \left[D_{LL_i} L^{-2}(\partial f_i/\partial L)\right] + G_i(L)\mu^{-1/2}(\partial f_i/\partial \mu)$$

$$- \Lambda_{io}f_i - \sum_{j=0}^{s} \Lambda_{ij}f_i + \sum_{j=1}^{s} \Lambda_{ji}f_j \quad \text{for } i \neq j$$

(5.95)

where Λ_{ij} denotes charge state transformation from state i to state j, so that $\Lambda_{ij} = 0$ for i = j [Spjeldvik, 1979].

The radial diffusion equation has been solved for equatorially mirroring radiation belt oxygen ions [Spjeldvik and Fritz, 1978b], and one of the findings is that oxygen ions can be more numerous than protons at multi MeV energies. The oxygen ion charge state distribution is predicted to vary from a dominance of O^+ ions at energies below $\sim$ 100 keV to successively higher charge states at the higher energies; for example at 4 MeV the

fourth charge state should be most abundant. A significant finding, illustrated in Figure 5-29, is that the radiation belt charge state distribution in the interior of the radiation belts (L < 5) is almost completely independent of the charge state distribution of the outer radiation zone source. In fact, this figure shows that regardless of the source being ionospheric (source charge state 1) or solar (source charge state 6 dominant) a steady state radiation belt distribution over ion charge states evolves that is independent of the source characteristics in the interior of the trapping region.
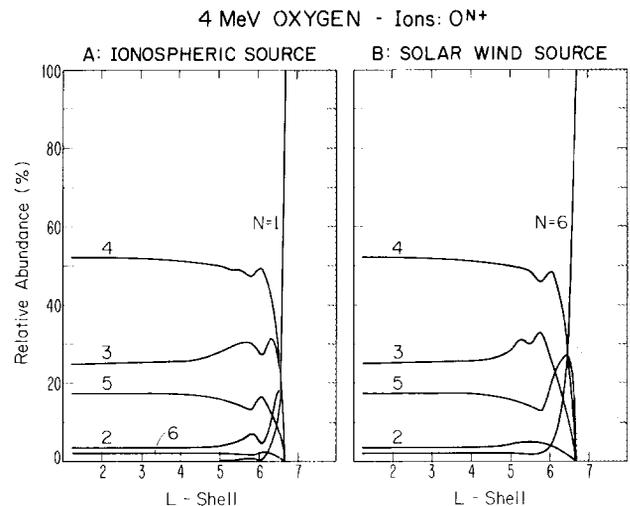

Figure 5-29. Relative charge state distribution for radiation belt oxygen ions. Left panel: an ionospheric source of O^+ ions is assumed; Right panel: a solar (wind) source of O^{6+} ions is assumed. One finds the steady state radiation belt charge state distribution in the interior of the trapping region becomes largely independent of the source charge state characteristics.

The findings concerning charge states of energetic radiation belt ions may be summarized as follows:
1. Higher charge states are crucially important for the overall structure of the heavy ion component of the earth's radiation belts above $\sim$ 100 keV.
2. Charge state redistribution processes are of major importance throughout much of the radiation belts and at all energies.
3. Radiation belt charge state distribution becomes largely independent of source charge state characteristics because of the frequent "internal" charge exchange.
4. Relative charge state distribution is to a large extent independent of the diffusive transport rate in much of the inner magnetosphere.

The last two conclusions are valid below a charge state redistribution zone adjoining the particle injection region in the outer radiation zone.

5.5.1.5 Theoretical Radiation Belt Ionic Composition.

Because of experimental difficulties, only very limited information is available concerning the actual composition of radiation belt ion fluxes. For this reason we present a theoretical prediction of radiation belt protons, helium and oxygen ion fluxes at L = 3.25 (in the center of the radiation belts). This is shown in Figure 5-30. It must
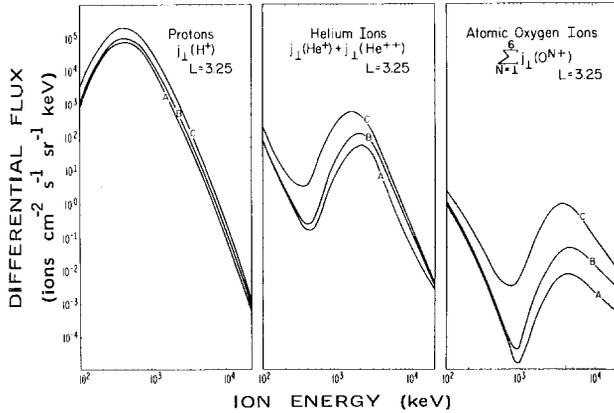

Figure 5-30. Theoretical model of the radiation belt ion fluxes: Comparison of theoretically predicted energy spectra of proton, helium and oxygen fluxes at L=3.25 for different diffusion coefficients [Spjeldvik, 1979].

be kept in mind that these predictions have yet to be verified or refuted by experimental observation, particularly in the 100–1000 keV range. The prediction is that protons should be the dominant ion species from 0.1 to 1 MeV, helium ions should dominate at 1 to several MeV per ion, and at higher energies oxygen (and possibly also carbon) should dominate. These comparisons are done at *equal total ion energy.* If comparison is made at *equal energy per nucleon,* then protons would be the dominant constituent at almost all radiation belt energies beyond a few tens of keV.

5.5.2 Geomagnetic Storms

Most radiation belt modeling deals with equilibrium conditions appropriate for quiet time conditions. There is at the present time no fully comprehensive radiation belt model for the effects of geomagnetic storms and other disturbances. The reason is partially the incomplete knowledge of the radiation belt particle source mechanisms, and in part that disturbed time modeling is difficult because of the changes in magnetic field and time varying electric fields that must be also incorporated. Research is being conducted in this area, but no definite models are available as of this writing.

Specific types of disturbances and associated time variability have, however, been analyzed. Among these are studies of the post-geomagnetic storm decay of energetic particle fluxes following the (yet not fully explained)

injection events. Lyons and Thorne [1973] have demonstrated that the radiation belt electron particle scattering lifetime can explain quantitatively the restoration of the radiation belt slot region after it becomes filled in during the storm injection process. Spjeldvik and Thorne [1975] subsequently demonstrated that the precipitating electron flux into the middle latitude ionosphere following such storms causes enhanced D-region ionization of sufficient magnitude to explain VLF radio wave phase anomalies observed at such times. Spjeldvik and Lyons [1980] have suggested a simplified prediction model for these effects.

There is reason to think that magnetic storms differ considerably from one another, not only by the magnitude of the ring current storm index D_{st} but also in the injection characteristics of energetic ion fluxes. Once injected, radiation belt particles become subject to the normal processes in the trapping region discussed earlier. For specific magnetic storms, the post-storm decay of protons and heavy ions has also been studied, and fair agreement between predictions and observations has been reported in limited energy ranges where the data were available [Spjeldvik and Fritz, 1981a & b].

5.5.2.1 The Variability of the Parameters.

Within the framework of radiation belt diffusion theory, the injection of particles is described by a (time variable) source term $S(L, P, \alpha_0; t)$. The boundary conditions may also be time variable, reflecting dynamic conditions on the outer edge of the stable trapping region $f(L_{max}, P, \alpha_0; t)$, and the transport coefficients, D_{LL} and $\bar{D}_{\alpha_0\alpha_0}$, will also be time variable reflecting the geomagnetic activity level. Based on limited data, Lanzerotti et al. [1978] estimated that the radial diffusion coefficient might vary with the K_p geomagnetic index as

$$D_{LL}^{(M)} = 10^{-\xi} L^{10} \qquad (5.96)$$

with

$$\xi = -(9.6 - 0.07 \sum_{1/2 \, day} K_p). \qquad (5.97)$$

It is not yet known how $D_{LL}^{(E)}$ and $\bar{D}_{\alpha_0\alpha_0}$ might vary with geomagnetic conditions. It is known however that the exospheric neutral density varies with activity (because of the heating of the upper atmosphere), and the plasmaspheric densities certainly vary strongly. A first approach may be to solve the appropriate transport equations using perturbation theory for the different variables. Some geomagnetic conditions may, however, be too drastically altered to be treated as perturbations, so caution is in order. At the present time there are many unknowns, and specific models have yet to be developed.

5.5.2.2 Magnetic Topology Variations.

During the early phase of magnetic storms the earth's magnetic field

becomes compressed on the dayside. It has been observed that the subsolar magnetopause can be pushed inward from an average location of $\sim 10 R_E$ to $\sim 5 R_E$ during large storms. This implies a large B-field change. Depending on the rapidness of the field change, the particle population may respond adiabatically or non-adiabatically. However, most magnetic storms do not cause such a large perturbation of the magnetic field. Increase in the lower energy (~ 10–500keV) radiation belt ion fluxes produces an enhanced *ring current* (see Section 5.7) that depresses the earth's magnetic field earthward of the enhanced particle flux region, and causes adiabatic deceleration of the trapped radiation belt particle fluxes. These effects must also be incorporated into storm-time radiation belt prediction models.

On the other hand, geoelectric fields penetrating into the trapping region during disturbed conditions [Harel et al., 1981a, b] can cause cross-L non-diffusive transport and thus adiabatic acceleration of the particle population [Lyons and Williams, 1980]. The relative influence of these processes depends on particle energy.

5.6 EMPIRICAL RADIATION MODELS

Since the discovery of the earth's radiation belts, the population of trapped particles has been measured with ever improving instrumentation. The early Geiger counters flown on the first few spacecraft had little or no particle identification capabilities. Subsequent instruments used foil techniques, solid state detectors, magnetic and/or electric deflection techniques and electronic signal discrimination. This led to a clear separation of electrons and ions (which were then assumed to be solely protons). During the later years of space exploration the presence of a multitude of different ion species was established. The purpose of this section is to provide a brief overview of existing radiation belt data, as a source guide for those who require crude numerical estimates of the radiation environment. It is emphasized that the older empirical "proton" model in reality represents contributions from many ion species, and that sometimes the heavy ion contribution may be dominant.

5.6.1 Data Acquisition and Processing

Empirical radiation belt models are compiled by NASA/National Space Science Data Center, Goddard Space Flight Center in Maryland [Vette et al., 1979 and references therein]. These models represent a systematic effort to compile many years of data containing a large number of disparate satellite observations into a few key models. These observations were separated in space and time, and made with highly varying instrumentation so that subjective judgments were necessary regarding data quality. The complexity of the task is appreciated if one considers the volume of space to be covered and the time variation in the particle fluxes. Most of the data used in the NASA models were obtained in the 1960's and early 1970's. For example, the present AP-8 model for protons is a combination of 94 different instrument energy detector channels from instruments flown on 24 satellites [Sawyer and Vette, 1976]. The combined data sets were smoothed to obtain omnidirectional flux distributions in the B, L parameter space. The fluxes were integrated over all pitch angles and, therefore, directional information was not utilized. Other limitations in the data sets are variations in instrument response and the lack of local time dependence considerations. Also note that the flux models are compiled from a data base obtained over a brief time period in comparison with other geophysical and solar time scales. Long term dynamical changes in the radiation belts are not well understood so that extrapolation to different epochs must be done cautiously. For example, much higher fluxes than the models give have recently been observed. One example of very long term effects is the adiabatic energization of inner belt protons by the secular variation of the earth's magnetic field [Schulz and Paulikas, 1972].

5.6.1.1 Protons (Ions). It has become customary to refer to energetic protons located below L $\sim$ 2 as inner belt or inner zone protons. This is a misnomer, however, since the proton fluxes normally have only one radial flux peak. Sawyer and Vette [1976] have completed an extensive model of the trapped "proton" environment out to L = 6.6 for energies above 100 keV. The measured ions were labeled "protons", although no actual ion identification was made. The model is composed of two parts, AP8MIN and AP8MAX, which correspond to observations made during the 1960-1970 sunspot minimum and maximum conditions, respectively. The difference between these two models is thought to result in part from differences in upper atmosphere heating during solar active periods such that the trapped particle collision rate (due to the exospheric expansion) was increased. AP8MAX differs from AP8MIN for altitudes less than about 1000 km and for L values less than 2.9. Steep spatial gradients in the ion fluxes at lower altitudes are difficult to determine accurately.

An equatorial profile of the ion (proton) fluxes as given by AP8MIN is shown in Figure 5-31. Note the presence of >400 MeV protons for L < 2. This is consistent with higher energy protons being produced by the decay of neutrons produced in the atmosphere by cosmic rays (the CRAND source). The lower energy fluxes can arise from inward radial diffusion as discussed in the theoretical modeling section.

The AP8 proton models include no data after 1970 and very little data above 100 MeV energies [Vette et al., 1978]. Although the "proton" belt is considered far more static than the electron belts, significant enhancement
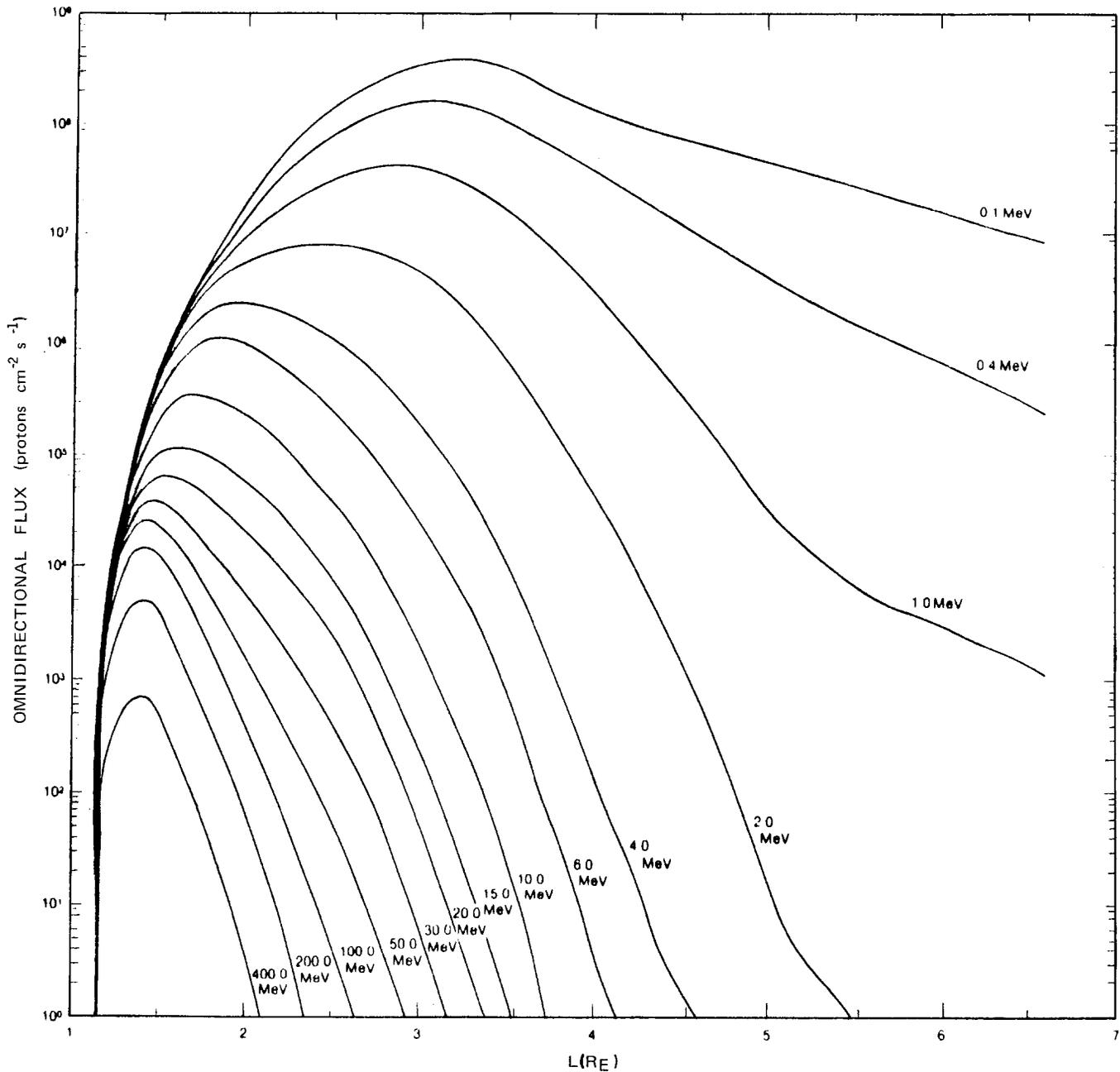
Figure 5-31. Radial distribution of AP8MIN omnidirectional fluxes of protons in the equatorial plane with energies above threshold values between 0.1 and 400.0 MeV [Sawyer and Vette, 1976].

and depletions have been observed. A secondary equatorial proton peak (40-110 MeV) of unknown origin was observed by McIlwain [1965]. This peak moved from L = 2.25 to L = 2.1 earth radii between January 1963 and January 1965. During the large May 1967 magnetic storm 2.2 – 8.2 MeV proton fluxes were observed to increase more than a factor of 10 at L = 2.2 [Bostrom et al., 1971]. Lower energy (0.26-0.65 MeV) protons were observed to be preferentially enhanced during the same

storm at L = 3.0 [Rothwell and Katz, 1973]. Beyond L = 5 earth radii, order-of-magnitude fluctuations occur on time scales as short as 10 minutes [Sawyer and Vette, 1976]. Very large increases in MeV *heavy* ion fluxes at L = 2 – 5 were observed during the August 1972 magnetic storm event [Spjeldvik and Fritz, 1981a,b,c]. For this reason engineering applications should consider large deviations from the mean models.

Off-equatorially mirroring ions intercept the upper

atmosphere at higher equatorial pitch angles on lower L-shells. For example, Figure 5-32 shows the B/B_0 distribution for three different L-values just above the
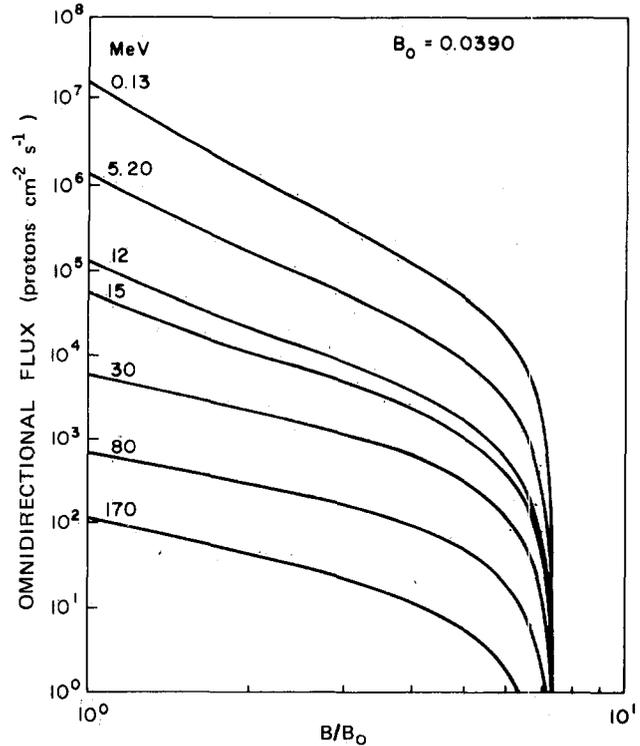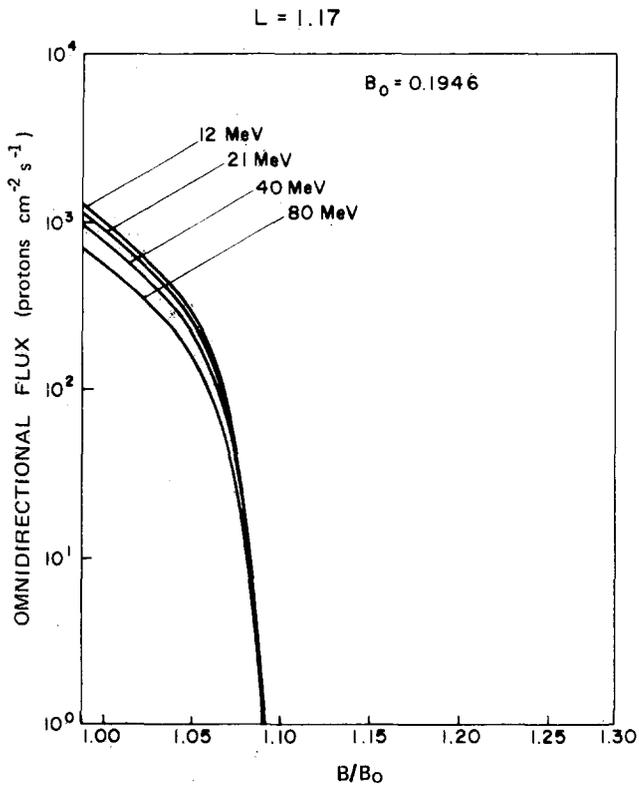
FLUX VS. B/B_0 DISTRIBUTIONS

L = 1.17

L = 2.00

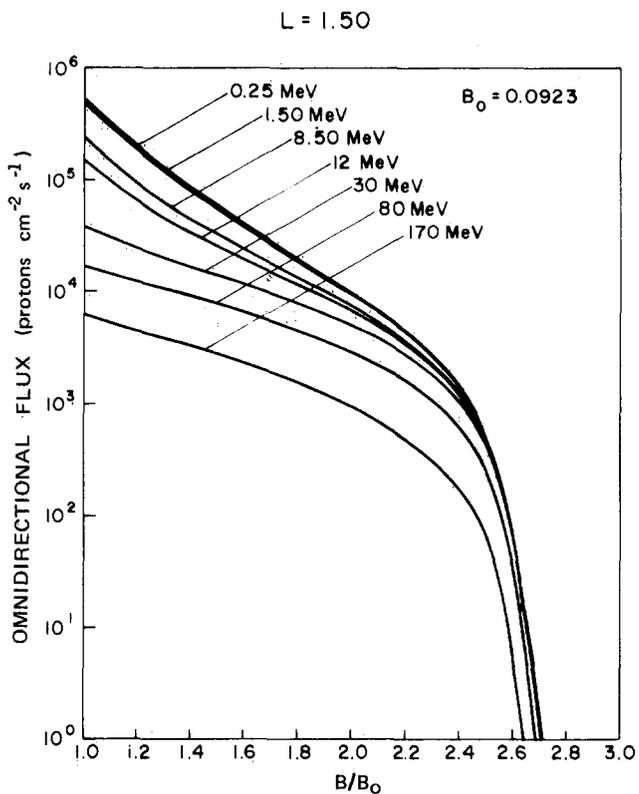
Figure 5-32. Empirical inner zone radiation belt proton (ion) flux vs B/B_0 for three representative L-shells, L=1.17, 1.50, and 2.0, and several representative energies as given by the AP8MIN proton model [Sawyer and Vette, 1976].

L = 1.50

atmosphere. At L = 1.17 the equatorial pitch angle distributions have very steep loss cone gradients such that the particle flux vanishes at $\alpha_{oc} \leq 73°$. At L = 1.50 this "cut off" is $\alpha_{oc} \sim 37°$ and for L = 2.00, $\alpha_{oc} \sim 21°$. These cutoffs come about because the atmospheric bounce loss cone is wide at the lower L-shells as seen in equatorial pitch angle.

The South Atlantic Magnetic Anomaly has a controlling effect on the inner zone particle fluxes in the vicinity of the loss cone. This anomaly arises from the earth's magnetic field being less intense at a latitude/longitude region located near the coast of Brazil. Trapped particles at these low L-shells will encounter their lowest mirroring altitude (H_{min}) and thus the densest atmosphere in this longitude region. Figure 5-33 shows omnidirectional proton flux contours in protons cm^{-2} sec^{-1} MeV^{-1} at 750 km altitude. These contours were derived from 5 to 7 MeV (dashed lines) and 28 to 45 MeV (solid lines) data channels on the AFGL particle identifier instrument flown on AF Satellite 72-1 in 1972. The data show that the location of the proton peak flux in the South Atlantic is dependent on energy. The 5 to 7 MeV peak is located around L = 2 while the 28 to 45 MeV peak is located around L = 1.3.

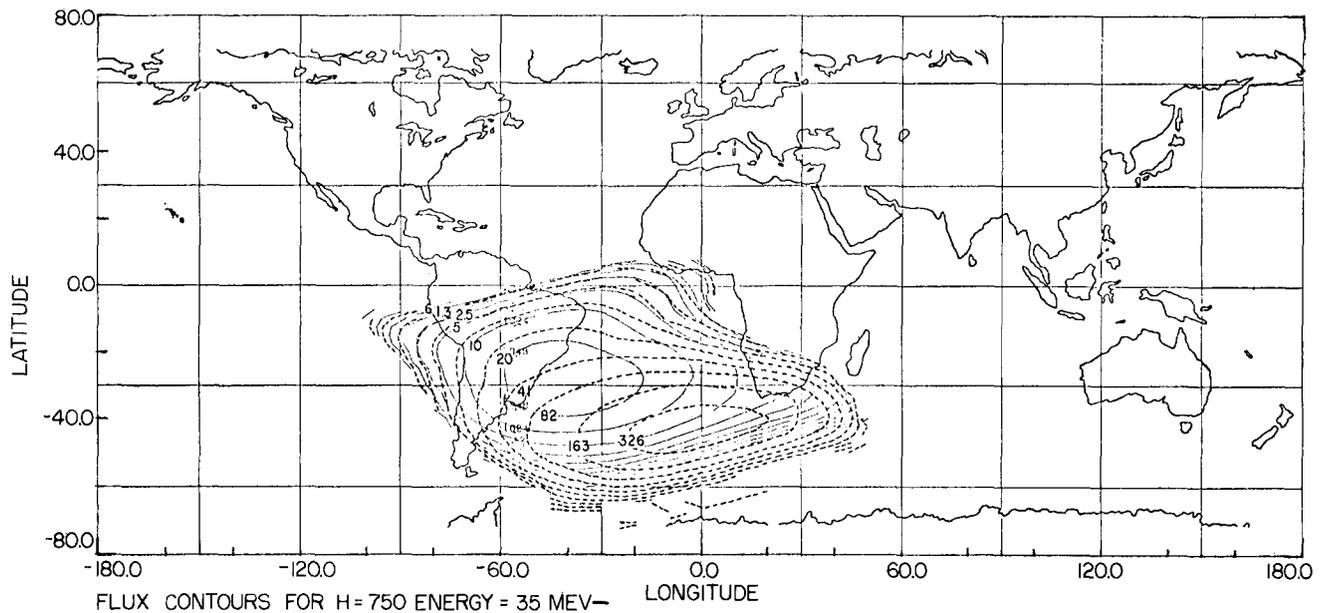FLUX CONTOURS FOR H = 750 ENERGY = 35 MEV—   LONGITUDE

Figure 5-33. Proton isointensity flux contours as measured in the South Atlantic anomaly at an altitude of 750 km. The solid lines depict 28-45 MeV proton (ion) fluxes and the dashed lines 5-7 MeV proton fluxes. The flux units are particles/(cm²-s-MeV).

The azimuthal drift around the earth of radiation belt particles through the South Atlantic anomaly region produces a "windshield wiper" effect. Electrons present in the enhanced loss cone created by the locally low B-field region are lost. These electrons are subsequently replenished by pitch angle diffusion during their drift around the earth outside the anomaly.

Solar cycle variations and high altitude nuclear detonations that modify the atmospheric composition significantly affect the trapped particle populations. A 15-year time study of inner belt 55 MeV protons concluded that the observed flux variations were consistent with expected atmospheric loss processes [Parsignault et al., 1981].

5.6.1.2 Heavy Ions. The abundance of trapped heavy ions give clues to the origin of the radiation belt particles. At high energies they also constitute a hazard to operational space systems. Over the last decade data have been acquired to sketch the spectral and angular dependence of the helium and carbon-nitrogen-oxygen (CNO) fluxes.

Helium Ions: Helium ions are sometimes referred to as alpha particles, although in a strict sense an alpha particle is only the totally ionized state (H_e^{2+}) of a helium ion. Figure 5-34 shows average equatorial helium ion spectra over a range of L-shells during quiet-time conditions [Fritz and Spjeldvik, 1979]. Notice that these spectra are very steep at $L \gtrsim 4$, become much harder with lower L-shells, and are almost flat at $L \sim 3$. This is expected since the lower energy helium ions are preferentially lost through the ion exchange mechanism and Coulomb collision energy degradation, as the particles diffuse

radially inward. The observed ratio between helium ion and proton fluxes simultaneously observed are given in Figure 5-35. Care must be exercised whether the ratio is
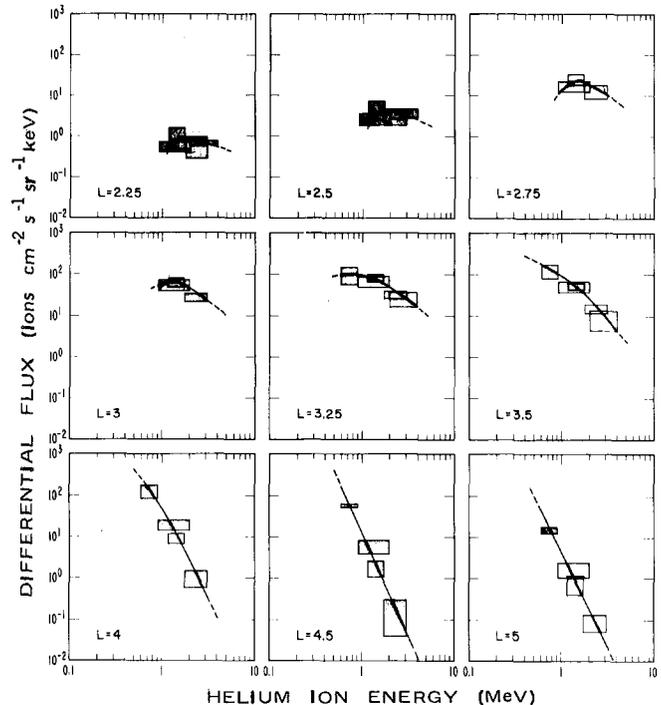

HELIUM ION ENERGY (MeV)

Figure 5-34. Energy spectra of equatorial radiation belt helium ions deduced from mass ion observations on Explorer 45 during the geomagnetically quiet period June 1-15, 1972. The data are given at L = 2.25, 2.5, 2.75, 3, 3.25, 3.5, 4, 4.5, and 5 [Fritz and Spjeldvik, 1979].
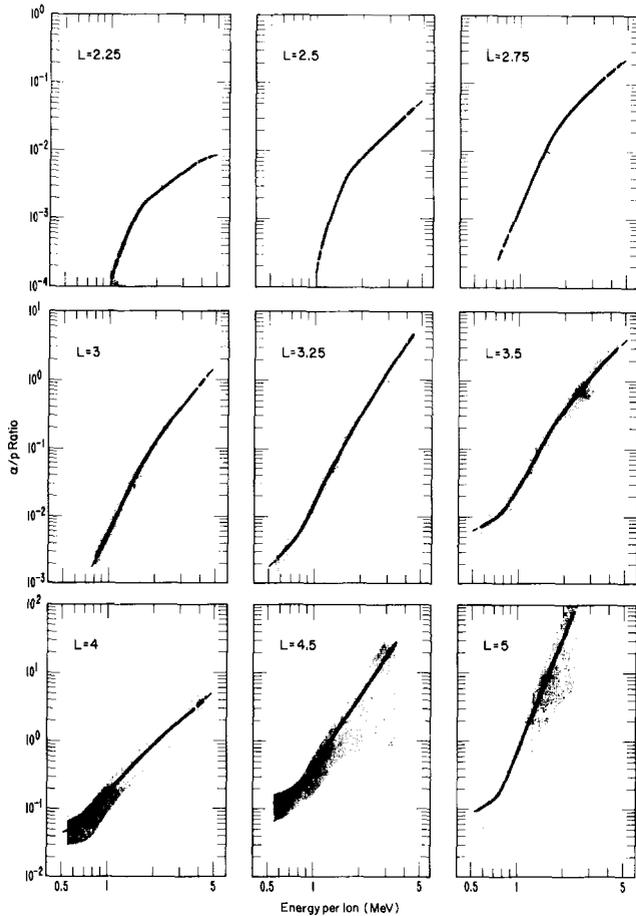
5-30

Figure 5-35. Quiet time He/p ion flux ratios in the equatorial radiation belts of the earth deduced from Explorer 45 observations during June 1-15, 1972. The ratios are calculated from flux observations at equal energy per ion. The shaded areas depict the experimental uncertainty in the data [Fritz and Spjeldvik, 1979].

defined at the same total ion energy or (as in this figure) at the same energy per nucleon. At higher total ion energies the heavy ion flux may be dominant over the proton flux at some L-shells (Figure 5-35) while at the same energy per nucleon proton fluxes usually dominate.

The equatorial helium ion pitch angle distribution is generally more anisotropic than the comparable proton pitch angle distribution. For L-values between 2.5 and 4.5 the proton fluxes most often vary as $\sin^n\alpha_0$ where $n = 4 \pm 2$ and α_0 is the equatorial pitch angle while for helium ions $n \approx 10 \pm 4$. Beyond $L \sim 5$ the helium fluxes are quite dynamic and characteristic quiet-time values are difficult to define. During magnetic storms the fluxes of energetic helium ions can increase by orders of magnitude in the heart of the radiation belts ($L \sim 2$-5), and the relative abundance of the different ion species can vary. At higher L-shells substorm effects can be significant. For example, during the 18 June 1974 substorm, helium ions were more numerous than protons at geosynchronous altitude for $E \geq 800$ keV/ion [Fritz and Wilken, 1976]. Blake and Fennell, [1981] also have noted that a

strictly sinusoidal pitch-angle distribution did not completely describe the 98-240 keV/nucleon ion fluxes at the geosynchronous altitude ($L \sim 6.6$).

Carbon-Nitrogen-Oxygen (CNO): Trapped oxygen ions can at times be much more numerous than protons particularly at $L \geq 5$, when compared at equal total ion energy. Figure 5-36 shows the radial flux profiles of carbon and oxygen ions as measured by the ISEE 1 spacecraft [Hovestadt et al., 1978]. At equal total ion energies in the MeV range the carbon to oxygen flux ratio is of the order of 0.5, and at equal energy per nucleon the carbon flux can dominate. This indicates an extraterrestrial source for the very energetic trapped heavy ions since the ionospheric C/O-ratio is $< 10^{-5}$ [Blake, 1973]. The CNO flux pitch angle anisotropy is even more pronounced than that of helium, having a value of the anisotropy n-index typically between 12 and 16. At the higher total energies (>800 keV) and at geosynchronous altitudes the CNO flux has been measured to be higher than that of protons and helium.

Very Heavy Ions: Ions heavier than oxygen are also present in the earth's radiation belts in small quantities. It has been demonstrated that substantial injection of ions with nuclear charge $Z \geq 9$ can take place during some magnetic storms, and many orders of magnitude flux intensity enhancements at $\epsilon \geq 10$ MeV have been observed lasting for many months [Spjeldvik and Fritz, 1981c]. During such disturbed conditions the trapped fluxes of other ions (He, O, etc.) can also be greatly enhanced [Spjeldvik and Fritz, 1981a,b].

5.6.1.3 Trapped Electrons. Empirical flux models have been developed that describe the inner and outer electron radiation belts. The National Space Science Data Center at NASA/Goddard Space Flight Center has developed two inner belt models: AE-6 [Teague et al., 1976] for sunspot maximum, and AE-5 epoch 1975 [Teague and Vette, 1974] for sunspot minimum conditions. There is also an outer belt electron model called AE-4. An updated outer belt model, AE-7, is now under development. In this section a brief description of the models is given and typical electron flux versus L-shell profiles, energy spectra, and pitch angle distributions are quoted.

Inner Belt Electrons: The empirical data AE-5 model is based on flux data from five satellites, OGO 1, OGO 3, 1963-38C, OV3-3 and Explorer 26 [Teague and Vette, 1972]. This data base covered the period from December 1964 to December 1967, representing a transition from solar (sunspot) minimum towards maximum conditions. During this period the time-averaged Zurich sun spot number R_z ranged in value from about 10 (December 1964) to around 100 (December 1967). In constructing the AE-5 model it was assumed that the total inner belt electron flux is composed of four components: 1) quiet day flux at solar minimum, 2) quiet day flux at other
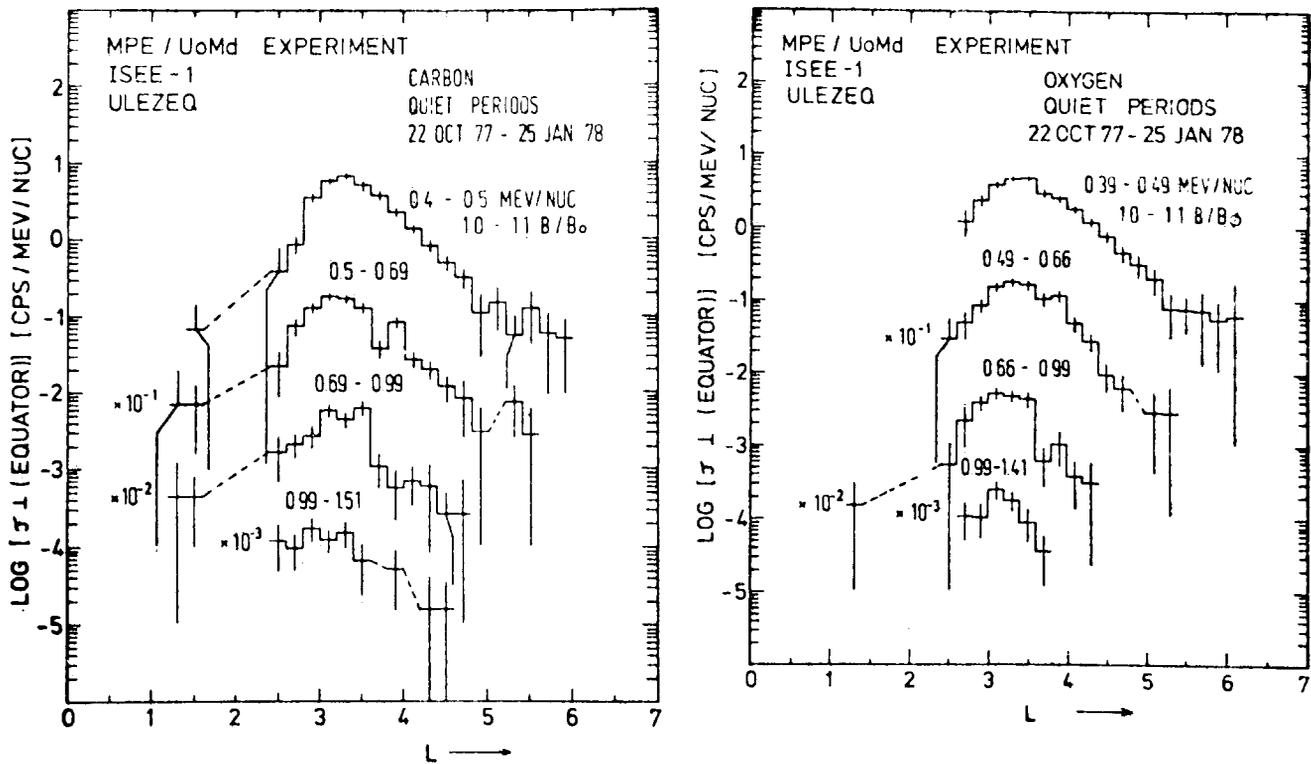
Figure 5-36. Equatorially trapped carbon and oxygen ion fluxes measured from October 1977-January 1978 during quiet times. Count rates may be approximately converted to omnidirectional flux units: ions/(cm²-s keV) by multiplying by 50/ΔE where ΔE is the appropriate energy passband in keV [Hovestadt et al., 1981].

times during the solar cycle, 3) storm time flux and 4) residual flux from the 1962 high altitude Starfish nuclear explosion. By late 1967 the Starfish generated energetic electron flux at $\epsilon < 1$ MeV had decayed to insignificant levels. It should be noted that for energies $\epsilon > 690$ keV the available data for the inner belt AE-5 model were quite limited. For example, within the observing range of the instruments the monthly averaged OGO 1 and OGO 3 data showed non-zero counts in this energy range only when the Starfish fluxes were still present or during storm times.

The quiet day solar cycle variation was defined by taking the ratio of the omnidirectional flux measured from solar minimum to a standard reference epoch (chosen as October 1967). Insufficient data necessitated the assumption of B-field (and therefore particle pitch angle distribution) independence for the geospace solar cycle variation. Also, the presence of Starfish residual energetic electrons restricted the analysis to later times when these man made radiation belt electron fluxes had decayed away. It should be emphasized that the solar cycle variation has been determined for only one specific cycle and that it may not apply to others.

The effect of magnetic storms on the time averaged inner radiation belt electron flux depends on 1) the frequency at which magnetic storms occur, 2) the magnitude of the storm time electron flux enhancement over

quiet time values, and 3) the duration and characteristics of the magnetic storms. The inner-belt electron flux increases are infrequent but substantial and long-lasting, so that a model storm effect was not extractable from this NASA data base. However, the average long term impact of magnetic storms was estimated by forming the ratio R_S which is the average electron flux (June 1966–December 1967) divided by the quiet-time electron flux (October 1967). The results are shown in Figure 5-37 and reflect a pronounced flux peaking at 1 MeV. Of course, the largest relative storm time energetic electron flux enhancements are found in the electron "slot-region" located at $L \sim 2 - 4$, depending on energy.

An inner belt electron model for solar minimum was derived from the model discussed above [Teague and Vette, 1974]. This is called the *AE-5 Epoch 1975 Projected Model* and was constructed by removing the estimated temporal variations. For example, the Starfish residual energetic electron flux component (L < 1.6 R$_E$, $\epsilon > 700$ keV) was removed, using the residual Starfish electron model of Teague and Stassinopolous [1972].

Similarly a *solar maximum model, AE-6,* was constructed using the AE-5 model at solar maximum values (epoch 1967) and with the estimated Starfish residual (background) energetic electron fluxes also subtracted out. This model is called *AE-6 Epoch 1980.*
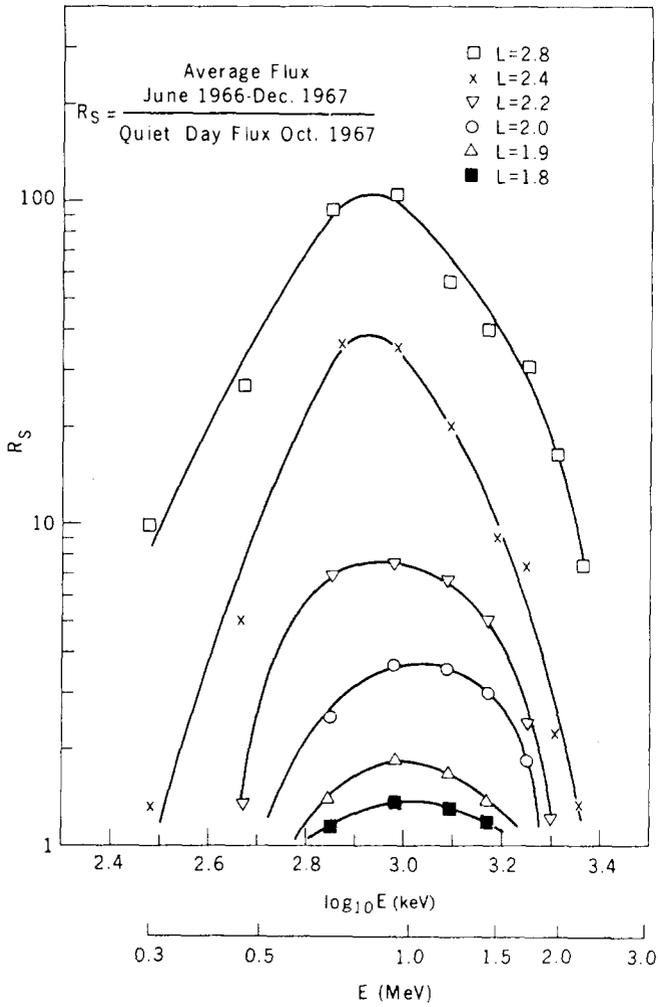
Figure 5-37. Estimate of the relative average effect of substorms on inner belt electron fluxes (Teague and Vette, 1972). It is cautioned that different disturbances can have different effects.
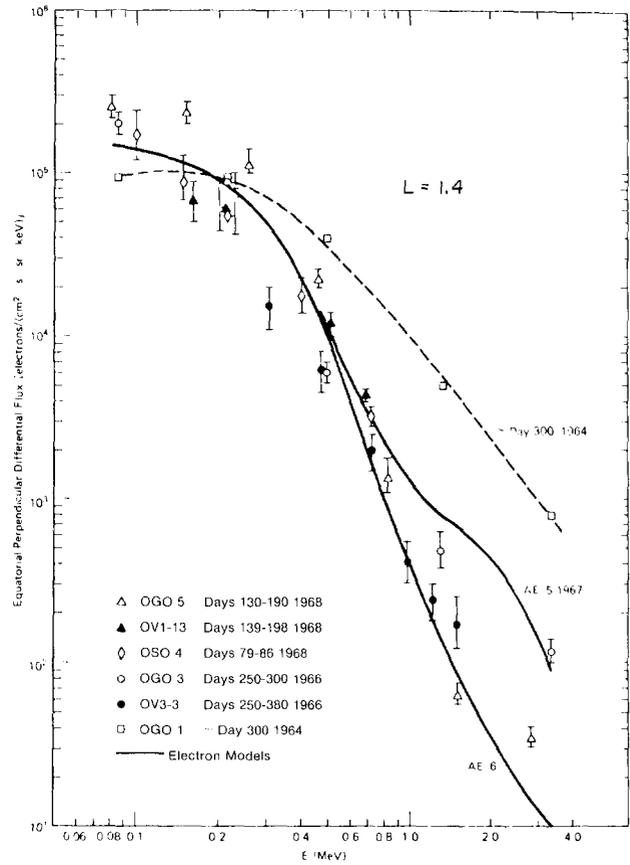

Figure 5-38. Empirical radiation belt electron fluxes at L = 1.4: Energy spectra comparison of the AE-5 1967 and AE-6 inner belt electron models with experimental data taken from the listed satellites for the times shown [Teague et al., 1979].

The electron models were verified by comparing them with additional data sets from the spacecraft OV3-3, OV1-13, OV1-19, OGO 5, OGO 1, OGO 3, 1963-038C, and OGO 4 [Teague et al., 1979]. These additional data were also obtained before 1970 and substantiate the model mean values for that particular epoch. Figure 5-38 shows a comparison between these data sets and the AE-6 and AE-5 1967 models. This is the quiet time energy spectra of equatorially mirroring electrons as measured at L = 1.5. The OGO 1 day 300 1964 results are evidently seriously contaminated by the Starfish detonation residual energetic electrons. Otherwise, these results show fair agreement between the AE-6 electron model and the different data. Figure 5-39 shows comparison of the model and measured equatorial pitch angle distributions at L = 1.4. The AE-5 1967 (solar maximum) model and the AE-5 1975 (solar minimum) model bracket the data within a factor ±2 to 3, except at very low equatorial pitch angles.

The quiet day inner belt electron fluxes for E < 690 keV at 1.3 < L < 2.4 can be represented by an analytic formula based on the empirical data [Teague and Vette, 1972]. The energetic electron flux is parametrized as follows:

$$j(\alpha_0, L, \epsilon) = A(\alpha_0, L) \, \epsilon \, \exp [\, \epsilon/\epsilon_0(\alpha_0, L)] \qquad (5.98)$$

where L is the McIlwain L-shell parameter, α_0 is the equatorial pitch angle and the parameters, $A(\alpha_0, L)$, $\epsilon_0(\alpha_0, L)$, are related to the equatorial values ($\alpha_0 = 90°$) by the following empirical expressions:

$$A(\alpha_0, L) = A(90°, L) \, \frac{\sin^m (\alpha_0 - \alpha_{OLC})}{\sin^m (\, \phi - \alpha_{OLC})} \qquad \phi > \alpha_0 \geq \alpha_c$$

$$= A(90°, L) \qquad\qquad 90° \geq \alpha_0 \geq \phi$$

$$(5.99)$$

$$\epsilon_0(\alpha_0, L) = \epsilon_0(90°, L) \sin^n \alpha_0/\sin^n \phi \qquad \phi > \alpha_0 \geq \alpha_c$$

$$= \epsilon_0(90°, L) \qquad\qquad 90° \geq \alpha_0 \geq \phi.$$
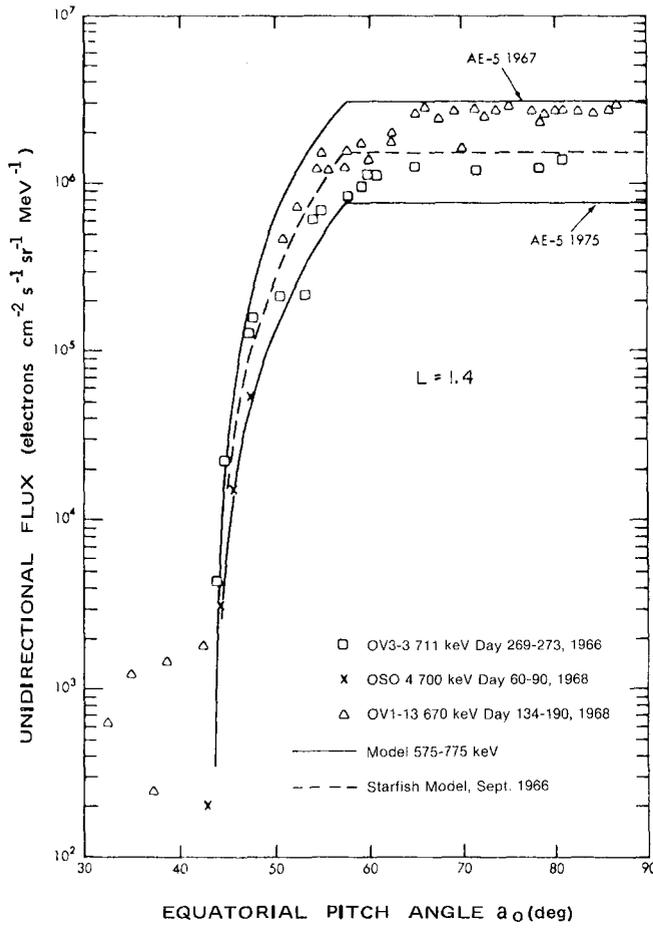
$$(5.100)$$

Figure 5-39. Empirical radiation belt electron fluxes: a pitch angle distribution comparison of the inner belt electron models with satellite data taken at L=1.4 [Teague and Vette, 1974].
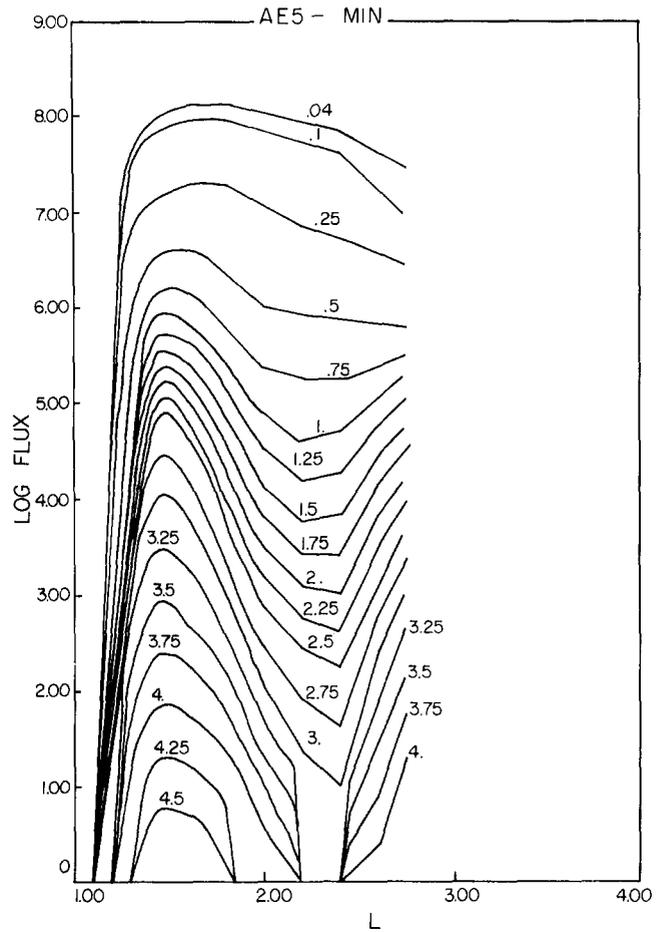

Figure 5-40. Empirical radiation belt electron observations: Equatorial flux versus L-shell for the AE5-MIN model as taken from the National Space Science Data Center (NSSDC) computer models. The flux is in units of electrons/cm^2-s), and the energy range is 0.04-4 MeV.

Values for ϕ, α_c, n, m, ϵ_0 ($\alpha_0 = 90°$, L) and A ($\alpha_0 = 90°$, L) for a given L-shell are given in Table 5-2.

In Equations (5.99) and (5.100) the equatorial electron pitch angle distributions are fairly flat out to an angle, ϕ, where they rapidly drop as $\sin^n \alpha$. The parameter α_{OLC} is the minimum allowed equatorial pitch angle (the loss cone angle) and corresponds to a 100 km electron mirroring altitude. These formulas should be used with caution, however, since they represent extrapolations based on an imperfect and incomplete data set. The dipole approximation gives α_{OLC} in terms of B_c from Table 5-3

$$\alpha_{OLC} = \arcsin\left[\left(\frac{B_E}{B_C L^3}\right)^{1/2}\right].$$ (5.101)

where B_C is the magnetic induction at the 100 km altitude level. Figures 5-40 and 5-41 show the equatorial electron flux profiles as given by AE-5 (1975 projected) and AE-6.

Outer Belt Electrons: The outer belt trapped electron fluxes are located between ~ 3.5 and ~ 11 R_E. Rapid changes in the magnetic field and background plasma can modify the electron flux levels within minutes. Because of the apparent coupling between magnetospheric substorm process and the outer belt trapped electron fluxes, time-averaged models have been developed. There are discernible changes in the average flux over the time period studied so that the model is given for two epochs. The NASA models are called AE-4 epoch 1964 (solar minimum) and AE-4 epoch 1967 (near solar maximum) [Singley and Vette, 1972]. The data base was acquired between 1959 and 1968 from 23 instruments on 11 satellites.

Because of the lack of azimuthal symmetry of the geomagnetic field in the outer radiation zone, studies of the radiation belt electron structure beyond L $\sim$ 5 requires the conventional B-L coordinate system (calculated from the earth's internal magnetic field) to be augmented with the additional coordinate local time, LT.

Table 5-2. Flux model parameters for quiet-day inner belt electrons. See text for details [Teague and Vette, 1972].

Quiet-Day Model Parameters (Inner Belt Electrons)							
Reference Pitch Angle = 90 Degrees							
EPOCH = 10/67							
L (R$_E$)	J(α_o = 90°) (cm^{-2} sec^{-1} sr^{1})	A(α_o = 90°) (cm^{-2} sec^{-1} sr^{-1} keV^{-1})	ϵ_o(α = 90°) (keV)	M	N	PHI (deg)	B$_c$ (G)
1.30	1.20E07	1.71E03	83.7	2.80	0.670	67.1	0232
1.35	1.70E07	2.39E03	84.3	2.20	0.660	61.4	0.234
1.40	2.23E07	3.08E03	85.1	1.70	0.650	57.5	0.238
1.45	2.81E07	3.81E03	85.7	1.20	0.640	59.0	0.241
1.50	3.41E07	4.56E03	86.5	0.93	0.630	65.0	0.245
1.55	3.99E07	5.21E03	87.5	0.92	0.620	66.0	0.249
1.60	4.49E07	5.74E03	88.4	0.91	0.610	67.0	0.253
1.65	4.79E07	6.08E03	88.8	0.90	0.600	66.5	0.257
1.70	5.10E07	6.42E03	89.1	0.89	0.590	66.0	0.262
1.75	5.46E07	6.81E03	89.5	0.88	0.580	68.0	0.265
1.80	5.77E07	7.16E03	89.8	0.87	0.570	70.0	0.268
1.85	6.00E07	7.57E03	89.0	0.86	0.545	76.0	0.271
1.90	6.11E07	7.93E03	87.8	0.85	0.520	86.0	0.274
1.95	5.84E07	7.80E03	86.5	0.83	0.500	90.0	0.277
2.00	5.38E07	7.50E03	84.7	0.80	0.480	90.0	0.280
2.10	4.69E07	7.15E03	81.0	0.79	0.470	90.0	0.286
2.20	4.15E07	7.00E03	77.0	0.78	0.460	90.0	0.292
2.30	3.61E07	6.50E03	74.5	0.77	0.450	90.0	0.298
2.40	3.11E07	6.00E03	72.0	0.76	0.440	90.0	0.304

The empirical LT dependence of the outer radiation belt electron fluxes has been determined to be

$$\log J\,(\alpha_o) \sim C(E,L)\,\cos\left[\pi\,\frac{LT - 11}{12}\right] \quad (5.102)$$

with LT in hours and $C(E, L \le 5) = 0$ [Vette, et al., 1976]. This is only valid in a time average sense, and it was found that at a given local time the electron flux intensity levels varied by at least factors of 10 to 50 over the data acquisition period stated.

Given the equatorial flux ($\alpha_o = \pi/2$ or B=B$_o$) the off equatorial outer belt integral electron flux ($\alpha_o \neq \pi/2$) can be estimated by [Singley and Vette, 1972]

$$J\,[> E, B, L] = J\,[> E, B = B_o, L]\,G\,[B, L] \quad (5.103)$$

and

$$G\,[B, L] = (B/B_o)^{-m}\left(\frac{B_c - B}{B_c - B_o}\right)^{m+1/2};\ B < B_c \quad (5.104)$$

$$G\,[B_1\ L] = 0 \qquad\qquad ;\ B \ge B_c\,.$$

The parameters m, B$_c$ and B$_o$ are all empirical functions of L and are given in Table 5-3. The parameter B is the magnetic field value at the desired location off the geomagnetic equator, and B$_c$ is the value of the magnetic field at 100 km altitude on the same field line.

Figures 5-42 and 5-43 show the AE-4 equatorial omnidirectional model electron fluxes from .04 to 4.50 MeV. Epoch 1964 represents solar minimum and epoch 1967 solar maximum. Using the above expressions with Table 5-3 and Figures 5-42 and 5-43, flux estimates can be made at non-equatorial latitudes.

Measurements from the OV1-19 satellite have indicated that the AE-4 model fluxes may be significantly too low, particularly at higher energies beyond 1 MeV [Vampola, 1977]. These newer data were averaged over periods which included two magnetic storms in 1969. The OV1-19 instrumentation measured radiation belt electrons in the 53 keV to 5.1 MeV energy range in 24 differential energy bands, which significantly improved the high energy data coverage over that which was available to construct the AE-4 models. The OV1-19 data has been incorporated into a new NASA model called AE-7 H1. Figure 5-44 shows the equatorial electron flux versus L-shell profile as predicted by the AE-7 H1 model. Note,

CHAPTER 5

Table 5-3. Flux model parameters for outer belt electrons. See text for details [Singley and Vette, 1972].

AE-4 B/B Model Parameters (Outer Belt Electrons)[o]			
L (R$_E$)	m	B$_o^*$ (G)	B$_c$ (G)
3.00	1.12	0.01154	0.580
3.10	0.87	0.01046	0.582
3.20	0.71	0.009511	0.585
3.40	0.66	0.007929	0.588
3.60	0.63	0.006680	0.593
4.00	0.60	0.004870	0.596
4.50	0.60	0.003420	0.599
5.00	0.60	0.002493	0.600
5.50	0.60	0.001873	0.601
6.00	0.60	0.001443	0.601
6.50	0.60	0.001134	0.602
7.00	0.60	0.000909	0.602
7.50	0.60	0.000739	0.603
8.00	0.60	0.000609	0.603
8.50	0.60	0.000507	0.6035
9.00	0.57	0.000428	0.6035
9.50	0.52	0.000363	0.604
10.00	0.44	0.000312	0.604
10.50	0.35	0.000269	0.604
11.00	0.24	0.000234	0.604

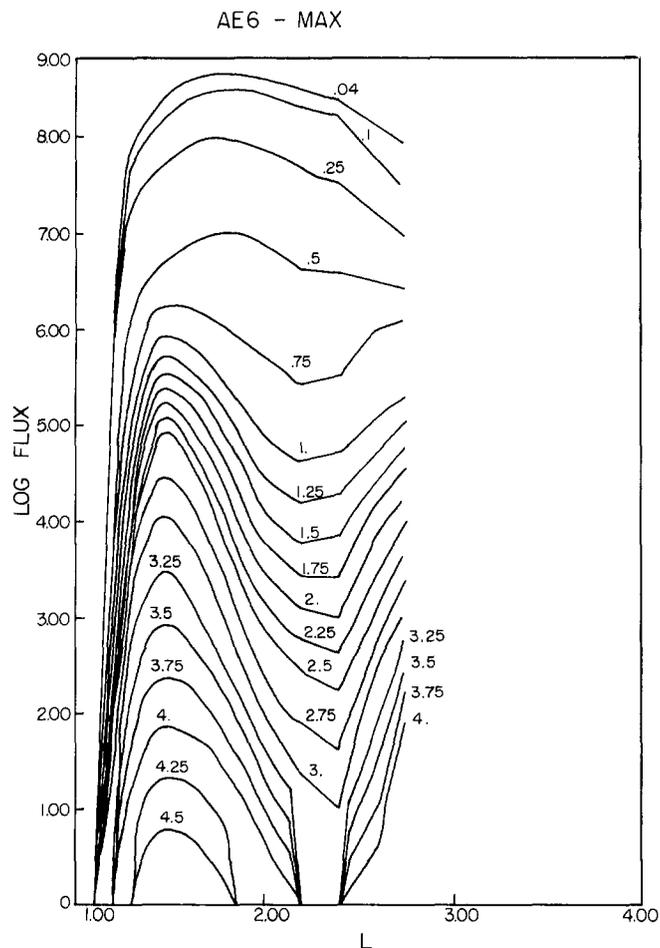$$*B_o = \frac{0.311654}{L^3}$$

Figure 5-41. Empirical radiation belt electron observations: Equatorial flux versus L profiles for the AE-6 model as taken from the (NSSDC) computer models. The flux is in units of electrons/(cm^2-s), and the energy range is 0.04-4 MeV.

however, that no direct equatorial measurements have been included in the empirical model for electrons (E > 300 keV) above 8000 km and below L = 5. Much of the data base was acquired from satellites orbiting at a significant inclination to the magnetic equator, making equatorial flux representations based on these data uncertain.

Figure 5-45 shows the differences between the AE-4 and the AE-7 models at energies above 1 MeV. The AE-7 LO model is based on data taken on the AZUR satellite and is shown in Figure 5-46. Note that $\epsilon \leq 1$ MeV electrons are most likely to penetrate spacecraft shielding and contribute to the accumulated radiation dosage and damage. It is partially for this reason that the empirical model uncertainties are of interest to spacecraft designers.

Magnetic storms may cause large energetic electron flux enhancements that last for several weeks in the radiation belts. Figure 5-47 shows an example of an electron flux enhancement as observed on OGO-5 [West et al. 1981] during 1968. This example shows that the electron flux at 1.53 MeV increased by more than four orders of magnitude during one particular magnetic storm. Figure 5-48 shows the mean exponential decay time of these electron flux enhancements in days for a wide

range of L-shells and energies. Also plotted are the predicted electron lifetimes [Lyons et al., 1972] (see Section 5.5.1.2 on theoretical electron models) which in this comparison appear to agree with the experimental data.

5.6.1.4 Shell Splitting Effects. The outer belt particle pitch angle distributions are particularly interesting due to a phenomenon called shell-splitting. Here we shall qualitatively describe the physical process; for analytic considerations, see Roederer [1970]. Shell-splitting arises from the lack of local time (azimuthal) symmetry of the earth's magnetic field, particularly at greater distances from the earth. It is usually considered important for L > 4, but it should also exist at lower L-shells where the earth's magnetic multipoles become significant. Shell-splitting arises because particles drifting in longitude preserving the first two adiabatic invariants modify their pitch angle and radial location according to the asymmetric magnetic field. While the concept of dipole L-shell is useful to describe principal features of trapped particles, actual non-dipolar geometry with azimuthal asymmetry requires more generalized coordinates. One such is
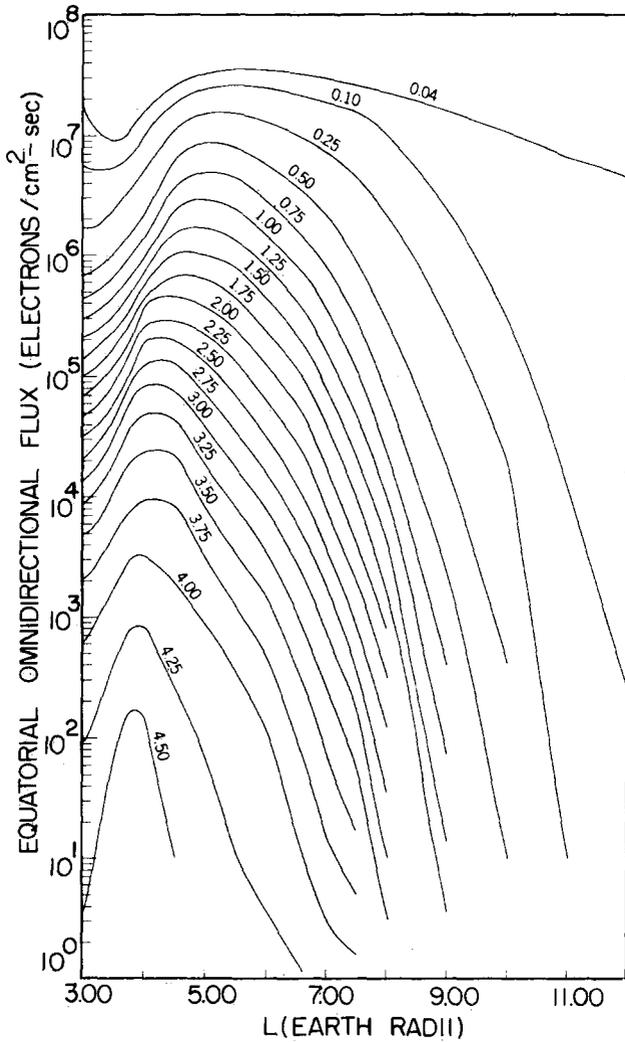
Figure 5-42. Empirical radiation belt electron fluxes: AE-4 radial profile of equatorial omnidirectional flux for various energy thresholds, *epoch 1964* [Singley and Vette, 1972].

Figure 5-43. Empirical radiation belt electron fluxes: AE-4 radial profile of equatorial omnidirectional flux for different energy thresholds, *epoch 1967* [Singley and Vette, 1972].

the (strictly non-invariant) McIlwain parameter L_m [McIlwain, 1961; Stone, 1963]. L_m is defined as the equivalent dipole L-shell of a test particle having the same magnetic mirror field B_m, second adiabatic invariant, and energy as a corresponding particle in the actual, non-dipolar geometry (Figure 5-1). Shell splitting can also result from asymmetric electric fields. For mathematical details see Schulz and Lanzerotti [1974]. Figure 5-49 shows particles on the same L-shell at local noon in the noon-midnight meridian plane. When radiation belt particles drift around the earth to the midnight sector they move to a lower L-shell and smaller equatorial pitch angles preserving their first adiabatic invarient values. Those particles starting closer to the equator at noon drift to lower L-shells at midnight. Conversely, Figure 5-50 shows the position of particles at local noon having initially been on the same L-shell at local midnight. Those starting closer to the equator at midnight move closer to the magnetopause on the dayside. If they
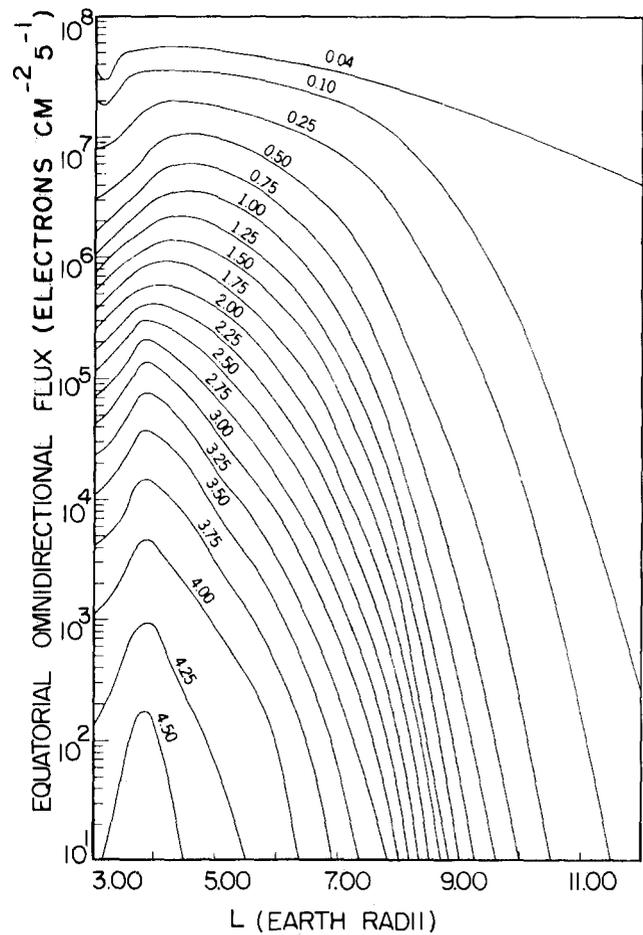
encounter the magnetopause they may become lost and there is a preferential depletion near $\alpha_o = 90°$. This gives rise to the so-called outer zone *butterfly* distribution which is a pitch angle distribution with a minimum around an equatorial pitch angle $\alpha_o = \pi/2$. Figure 5-51 shows a survey of the energetic electron pitch angle distributions in the near equatorial magnetosphere as measured by West [1979]. The butterfly distributions are clearly predominant in the afternoon sector after the eastward (counterclockwise) drifting electrons have interacted with the magnetopause.

Shell splitting also causes a coupling between pitch angle and radial diffusion. Any type of pitch-angle diffusion may be accompanied by radial diffusion if the B-field is azimuthally asymmetric. The direction of the radial displacement depends on the longitude at which pitch angle diffusion took place. Particles near the equator that move to lower pitch angles on the dayside will be radially displaced further from the earth on the nightside. Conversely, displacement to lower pitch angles on the nightside leads to an inward particle flux on the dayside. It is estimated that particles spend 2/3 to 3/4 of their
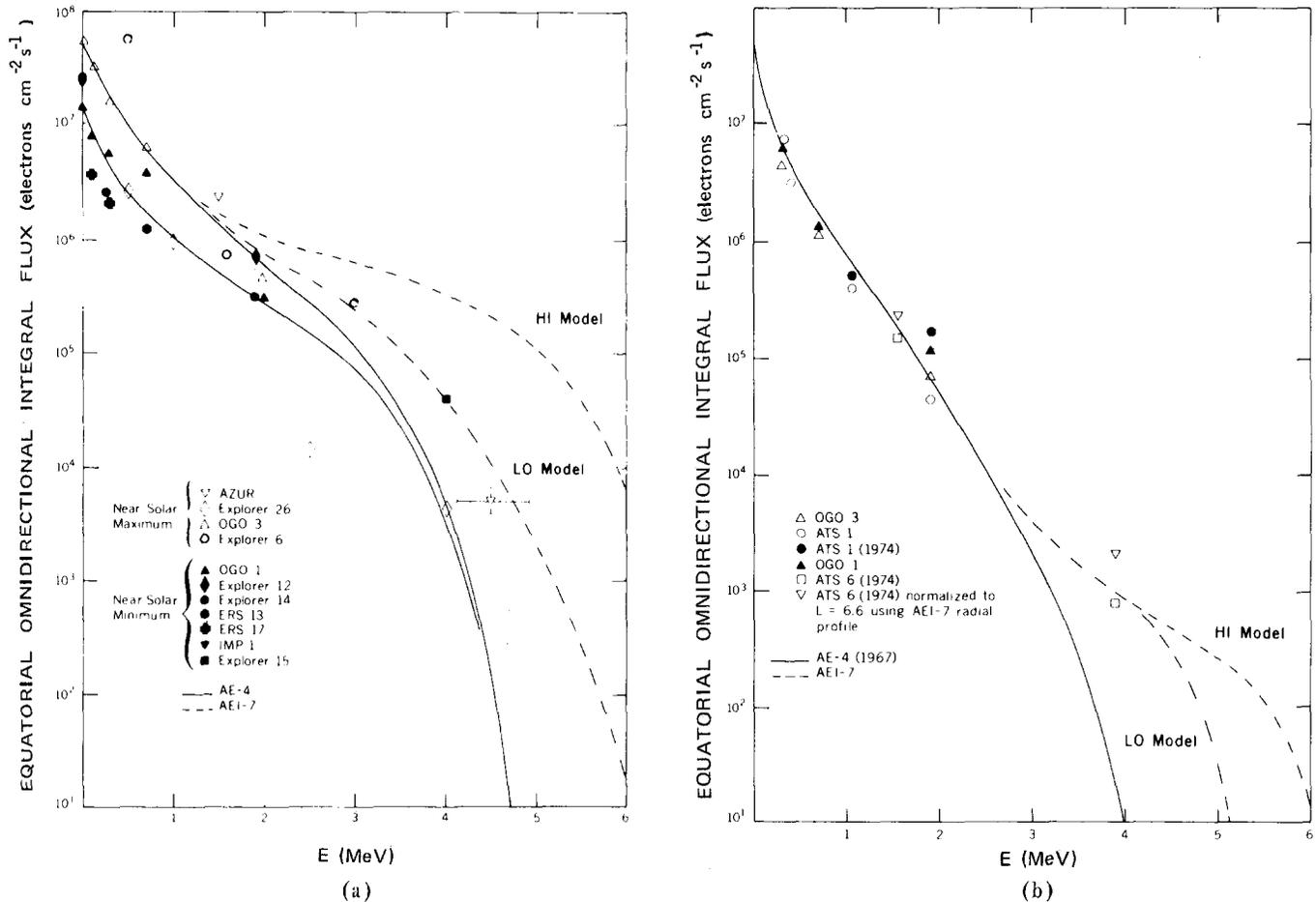
Figure 5-44. Empirical radiation belt electron fluxes:
    (a) Comparison of AEI-7 Model Spectra with a number of data sets at L=4. The HI model curve is mainly based on the OVI-19 observations from Vampola.
    (b) Comparison of AEI-7 Model Spectra with a number of data sets at L-6.6 [Vette et al., 1978].

drift period on the effective dayside so that pitch angle diffusion could lead to a net energy conserving outflow of particles [Roederer, 1970]. First and second adiabatic invariant conserving inward radial diffusion as described in the theoretical modeling section would increase particle energy with inward radial motion. After undergoing many cycles of outward ϵ-conserving diffusion and inward μ-conserving diffusion, a significant local energization of trapped particles could result [Schulz and Lanzerotti, 1974 and Theodoridis, 1968], but this needs to be investigated further.

5.6.2 Geosynchronous Altitude Region (L ≈ 6.6)

Geosynchronous altitude is 3.6×10^4 km which corresponds to an L-shell value of about 6.6. A satellite at this altitude in the plane of the earth's equator will remain fixed over the same geographical location. This feature is highly useful for communication and surveillance satellites. The natural geosynchronous charged particle environment impacts the life-time and reliability of satellites

through radiation effects and spacecraft charging [Chapter 7]. Many studies of the geosynchronous environment have been made [for example, Paulikas and Blake, 1979; Young, 1979; Garrett, 1979; Baker et al., 1981; Mullen and Gussenhoven, 1983].

Near local midnight the magnetic field lines at geosynchronous altitude often depart strongly from any resemblance of dipolar shape during magnetically active periods. This effect is associated with changes in the pitch angle distribution of the particle fluxes from being peaked perpendicular to the magnetic field line to a more isotropic distribution. This and other flux changes have been used as diagnostic devices to study underlying magnetospheric processes [Higbie et al., 1978; Belian et al., 1978; Baker et al., 1978; Baker et al., 1980; Belian et al., 1981].

In this section the long term temporal behavior of energetic (> 1 MeV) electrons and the plasma environment is emphasized. Energetic electrons penetrate spacecraft shielding and may cause radiation degradation of microelectronic components. The plasma environment, of which the ions are an important component, modifies
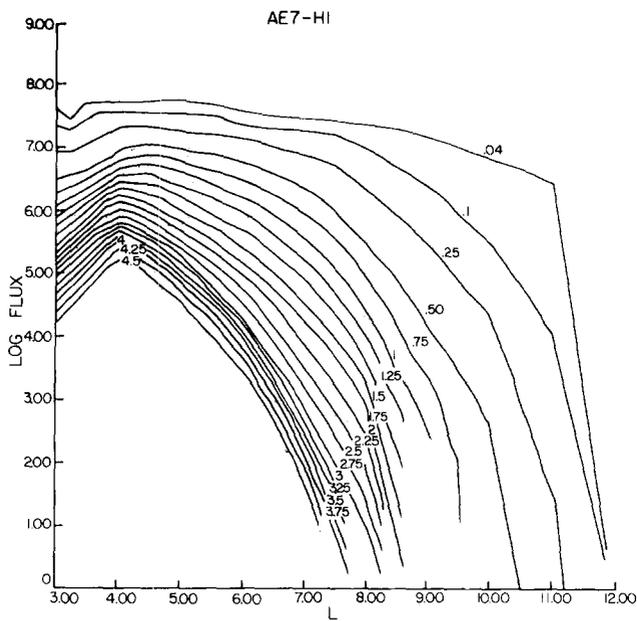
Figure 5-45. The NSSDC AE7-HI interim outer belt model for equatorial electron fluxes as a function of L. The listed energy is in MeV and the flux in units of electron/(cm²-s). The discontinuous portions of these curves highlight the model's areas of least accuracy.
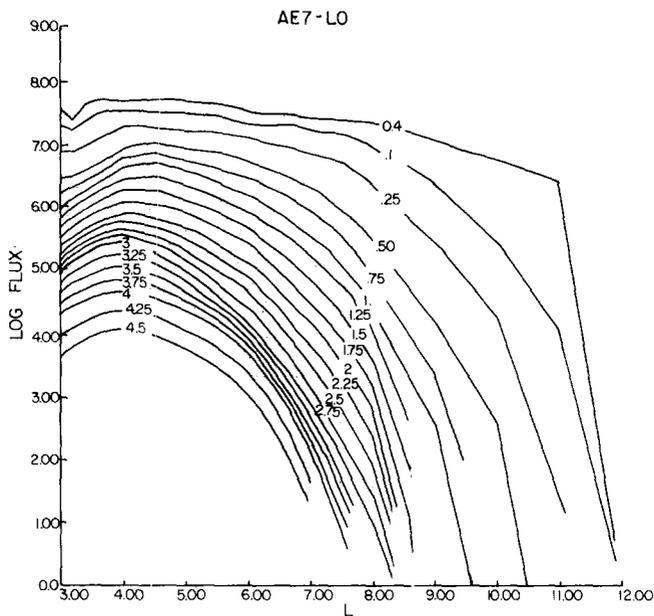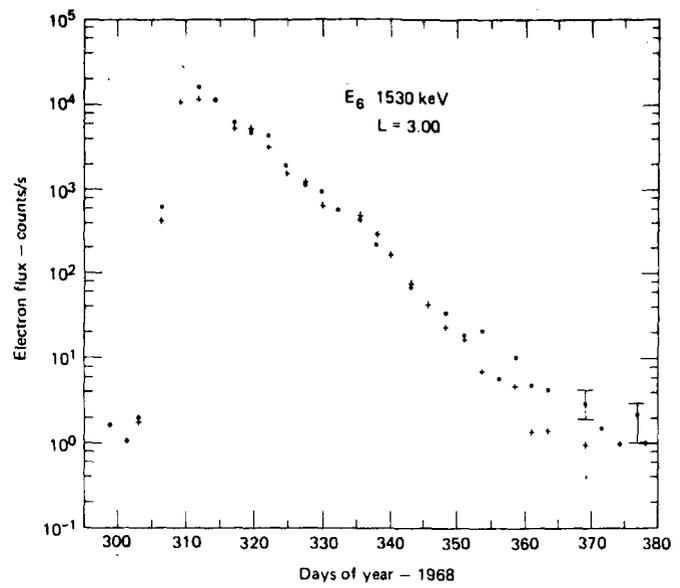

Figure 5-47. Radiation belt electron observations: An intense injection of energetic (1.53 MeV) electrons at L=3 as reported by West et al. [1981] during October 1968. Note the four orders of magnitude increase and the subsequent exponential decay.

Figure 5-46. The NSSDC AE7-LO interim outer belt model for equatorial electron fluxes as a function of L. The listed energy is in MeV and the flux in units of electrons/(cm²-s). The discontinuous portions of these curves highlight the model's areas of least accuracy.

the voltage to which a satellite will charge. Results from the SCATHA (Spacecraft Charging at High Altitude) satellite show that the ion composition at geosynchronous is a function of magnetic activity and local time [Mullen and Gussenhoven, 1983].

Energetic trapped electron flux intensities ($\epsilon \geq 1.0$ MeV) at geosynchronous altitude have been shown to be positively correlated with the average solar wind speed [Paulikas and Blake, 1979]. The 3.9 MeV integral electron flux [J(> 3.9 MeV)], for example, has been observed to vary by about a factor of 5 from a solar wind speed of 400 km/sec to one of 800 km/sec. Lower energy electron fluxes (140–600 keV), on the other hand show little such correlation. Sufficiently long time averages ($\leq$ 1 year) empirically remove the solar wind speed effects and reflect the overall average stability of the electron fluxes over longer time scales. For details see Paulikas and Blake [1979].

Energy spectra of energetic electrons in the geosynchronous altitude region measured with the SCATHA spacecraft are shown in Figure 5-52 [Mullen and Gussenhoven, 1983]. These data represent 75-day averages taken between February 1979 and February 1980, and on the average may be represented by a power law spectral dependence. Integration of the fitted curves gives integral flux levels that are consistent with the AE-4 and AE-7 models (Figures 5-42, 43, 45 and 46). This implies that the long term temporal averages of the electron fluxes at geosynchronous altitude did not materially change during the 1970's. The scatter of the individual SCATHA flux data measurements about the mean time-averaged flux is substantial. At times the observed electron fluxes differed from the mean values by well over an order of magnitude. The flux models, therefore, should be used with caution.
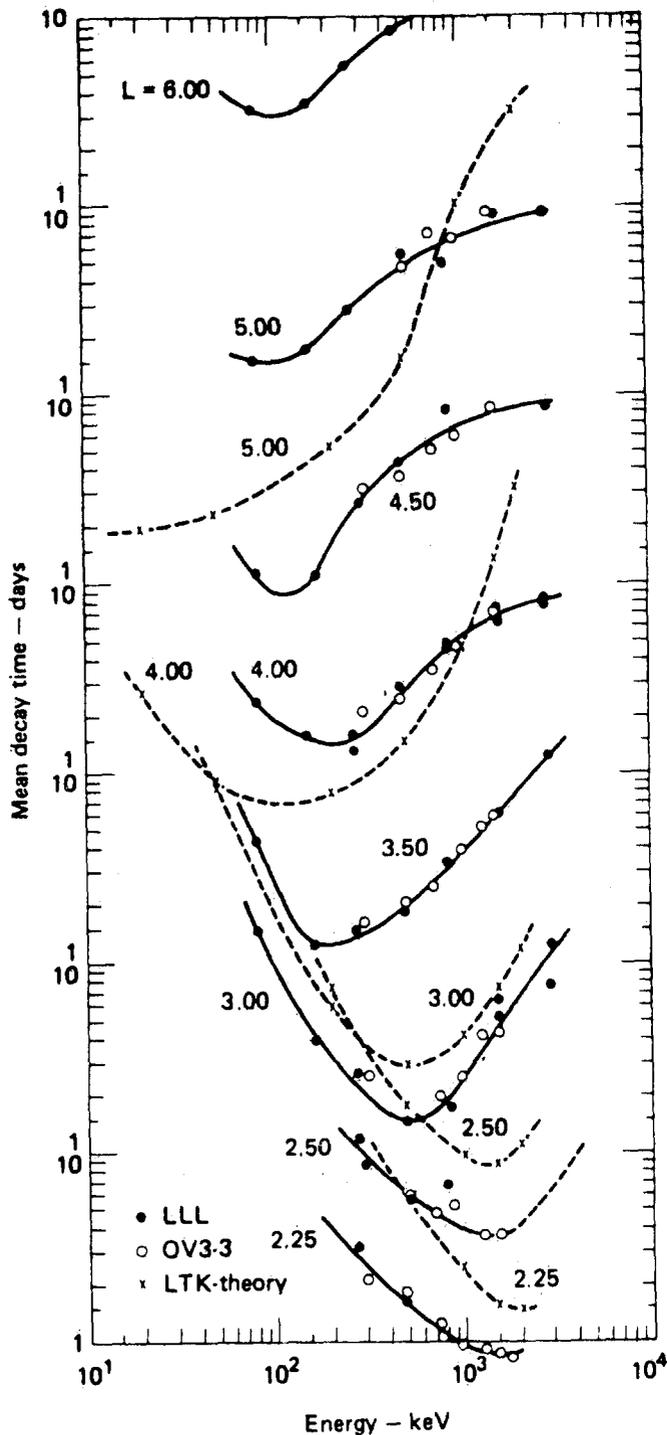
Figure 5-48. Radiation belt electron observations: Pitch angle diffusion lifetimes at constant L were in part derived from the data in the previous figure, and the predicted electron precipitation lifetimes are those of Lyons et al. [1972] [West et al., 1981].
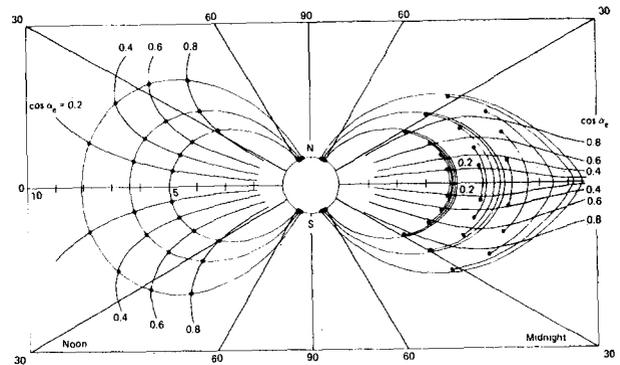

Figure 5-49. Theoretically computed shell splitting effects for particles starting on common field lines in the noon meridian. Dots represent the particles' mirror points. The curved lines give the position of mirror points for constant equatorial pitch angle α_0 [Roederer, 1970].
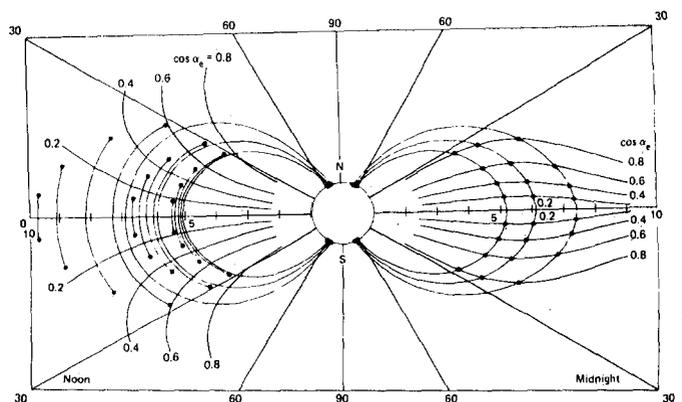

Figure 5-50. Theoretically computed shell splitting effects for particles starting on common field lines in the midnight meridian [Roederer, 1970].

It is useful to estimate the percentage of time that the electron flux will exceed a certain value. Figure 5-53 shows the cumulative probability distribution for the SCATHA 1.4 ~ 2.6 MeV energy channel in four L intervals. For example, from this figure one would

expect to find 1.4–2.6 MeV electrons with a flux intensity greater than 10 electron cm^{-2} sec^{-1} sr^{-1} keV) 50% of the time in the 5.5–6.0 L-shell region. On the other hand, from the same bar graph fluxes above 100 electron cm^{-2} sec^{-1} sr^{-1} keV are expected less than 10% of the time.

Ions are a dynamic component of the radiation environment at geosynchronous altitudes. The ion composition at low energies varies with magnetic activity as illustrated in Figure 5-54 [Mullen and Gussenhoven, 1983]. During magnetically active periods (high Kp) the O^+ component becomes enhanced relative to protons. An explanation for O^+ enhancement [Kaye et al., 1981; Fennell et al., 1981] is that the storm enhanced O^+ ions are accelerated up along the magnetic field lines from the auroral ionosphere, while the protons probably also originate from the magnetotail plasma sheet that moves closer to the earth during magnetically active periods. Oxygen ion enhancements also increase the particle
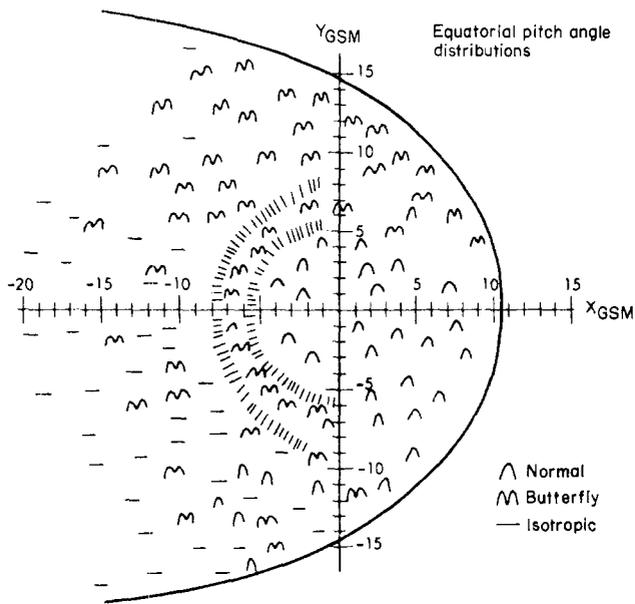
Figure 5-51. Survey of energetic electron pitch angle distributions observed in the near equatorial magnetosphere [West et al., 1979].

Figure 5-52. Time-averaged energetic electron energy spectra measured near geosynchronous altitude from February 1979 to February 1980. These curves represent a 75 day average and approximate a power law curve. Individual data show, however, that deviations two orders of magnitude from these means are not uncommon [Mullen and Gussenhoven, 1982].

energy density relative to that of the magnetic field. Figure 5-55 [Mullen and Gussenhoven, 1982] shows the geosynchronous altitude ratio β of the particle energy density to the magnetic field energy density as a function of local time. The individual curves represent various levels of K_p where higher K_p is a measure for higher magnetic activity [Jacobs, 1970]. A β value greater than unity
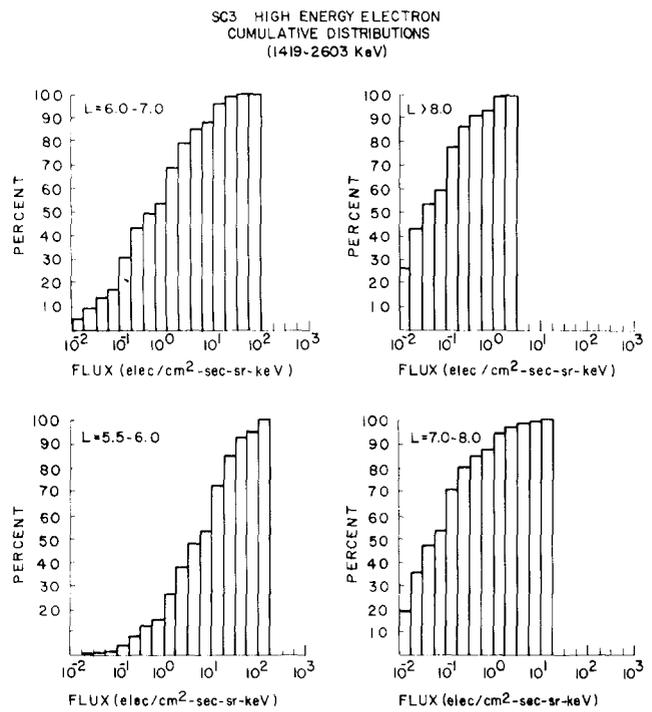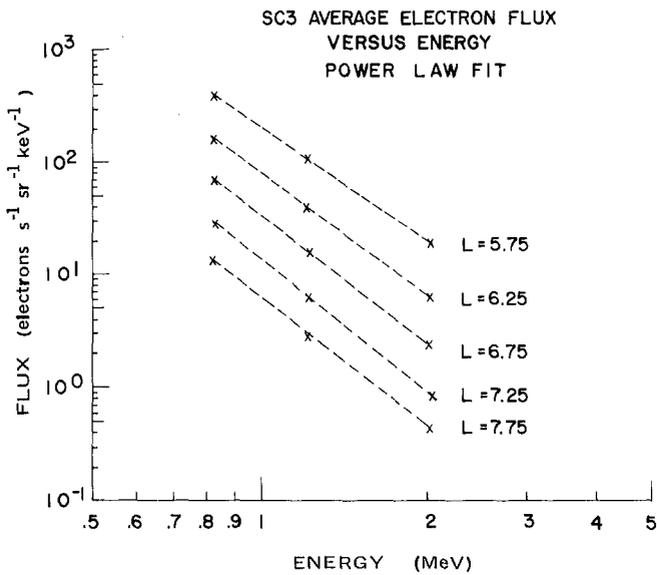

Figure 5-53. Cumulative probability that the high energy electron flux (at energies 1419-2603 keV) is less than the shown levels. This figure gives an estimate of the "spread" in the individual measurements used to obtain Figure 5-51 [Mullen and Gussenhoven, 1982].
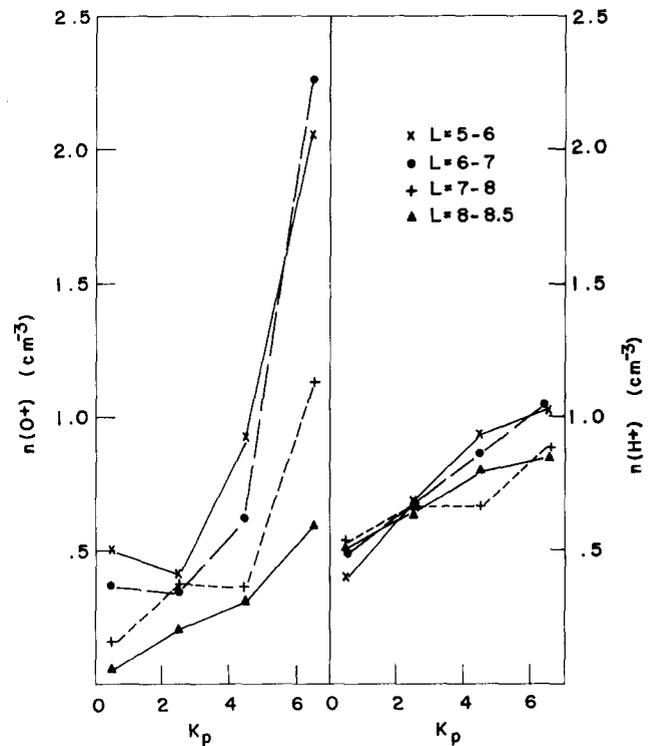

Figure 5-54. Average Oxygen (left) and hydrogen (right) number densities as determined from the Lockheed ion composition measurements on the SCATHA spacecraft (for energies 1-32 keV) versus K_p for various L-shell intervals [Mullen and Gussenhoven, 1982].
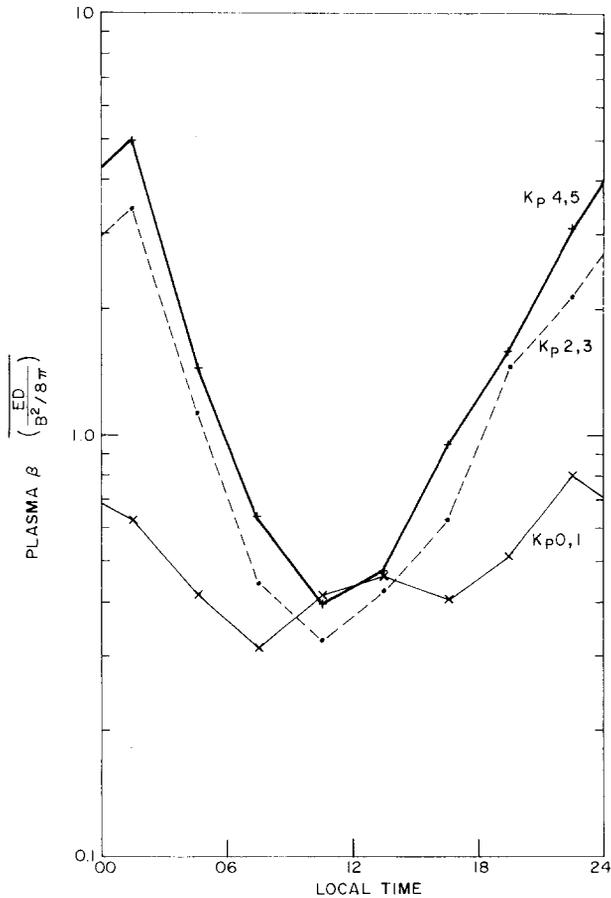
Figure 5-55. Time-average of the ratio of the particle energy density to the magnetic field energy density $(B^2/8\pi)$ as a function of local time. Higher K_p implies higher magnetic activity. These data represent over 90 days averages at of geosynchronous altitude (L=6.65) obtained during February 1979 to February 1980 [Mullen and Gussenhoven, 1982].

implies that the particles are not strongly confined by the magnetic field. A β value significantly less than unity suggests particle confinement in this region. These results indicate that the plasma processes that are operative during active periods at geosynchronous altitude are substantially different than those operative during quiet times. Garrett [1979] gives more details of the geosynchronous plasma environment.

5.7 THE RING CURRENT

The gradient-curvature drift of radiation belt particles causes differential motion that is mass and charge dependent: electrons drift eastward and positive ions drift towards the west. This constitutes an electrical current around the earth in the westward direction, called the extraterrestrial ring current. During geomagnetic disturbances, such as magnetic storms, the population of trapped particles at $\sim 1 - 800$ keV energies is substantially enhanced on L-shells between L = 3 and L = 6. As a consequence, the ring current is intensified and magnetic disturbances at the earth result.

5.7.1 Electrical Current Relations

The ring current itself produces a magnetic field that is superimposed on the earth's magnetic field. Enhancement in the ring current constitutes the cause of the magnetic field *depression* observed at mid-latitudes on the surface of the earth during the main and recovery phases of geomagnetic storms as well as magnetic field *enhancement* beyond $L \sim 6$–7, as illustrated in Figure 5-3. For this reason we shall consider the magnetic effects of the trapped particles.

As one can see from Equations (5.36) and (5.37), the particle gradient-curvature drift velocity is proportional to the particle energy. With the equatorial pitch angle, α_0, one may write

$$\mathbf{V}_d = \frac{\epsilon}{qB^3} \, (1 + \cos^2\alpha_0)(\mathbf{B} \times \nabla \, |\mathbf{B}|) \,, \qquad (5.105)$$

where electric field and gravity effects have been disregarded. Here $\mathbf{B}$ is the magnetic field due to the main (earth's internal) dipole moment and $\mathbf{M} = M \, \hat{\theta}$ where $\hat{\theta}$ is a unit vector in the magnetic northward direction. At the magnetic equator

$$\mathbf{B} = \frac{M}{r^3} \, \hat{\theta} = \frac{B_E}{L^3} \, \hat{\theta} \,. \qquad (5.106)$$

For simplicity in the presentation, we shall consider equatorially mirroring particles only, that is, $\alpha_0 = \pi/2$; for the mathematical treatment of the general case of an arbitrary pitch angle α_0, see Dessler and Parker [1959]. We then get

$$\mathbf{V}_d = -c \, \frac{3\epsilon}{qM} \, r^2 \, \hat{\phi} = c \, \frac{3\epsilon}{qB_E} \, L^2 \, \hat{\phi} \qquad (5.107)$$

where $\hat{\phi}$ is a unit vector in the eastward azimuthal direction around the earth. From Maxwell's equations (the Biot-Savart law; [Jackson, 1975]) the magnetic field generated by the drift motion of each particle is

$$B_d = -i \int_0^{2\pi r} \frac{d\ell}{r^2} \, \hat{\theta} \qquad (5.108)$$

where i is the magnitude of the single-particle drift "current":

$$i = \frac{q \, |\mathbf{V}_d|}{2\pi r} \,, \qquad (5.109)$$

and thus

$$\mathbf{B}_d = - \frac{3\epsilon}{M} \, \hat{\theta} \,. \qquad (5.110)$$

The minus sign indicates that the particle azimuthal drift generated field opposes the main (internal) dipole field earthward of the ring current particle population.

There is also a magnetic effect of the particle's spiral motion around the field lines. Each gyro-loop may be considered a small dipole moment $\mu = \frac{\epsilon}{B}$ (since for $\alpha_0 = \pi/2$, $\epsilon = \epsilon_\perp$), and the associated magnetic field is

$$B_g = \frac{\mu}{r^3} = \frac{\epsilon}{Br^3} = \frac{\epsilon}{B_E R_E^3} = \frac{\epsilon}{M} , \qquad (5.111)$$

which is in the direction of the internal dipole. The total perturbation at the origin due to a single equatorially mirroring particle is then

$$\Delta B_s = B_d + B_g = -\frac{2\epsilon}{M} . \qquad (5.112)$$

At the equatorial surface of the earth the unperturbed (internal) dipole field is just $B_E = \frac{M}{R_E^3}$ so that

$$\frac{\Delta B_s}{B_E} = -\frac{2\epsilon}{B_E^2 R_E^3} = -\frac{2\epsilon R_E^3}{M^2} , \qquad (5.113)$$

and noting that the total energy in the earth's unperturbed dipole field above the earth's surface may be written as

$$U_m = \frac{1}{3} B_E^2 R_E^3 = \frac{1}{3} \frac{M^2}{R_E^3} . \qquad (5.114)$$

We may express the relative ring current single particle perturbation as

$$\frac{\Delta B_s}{B_E} = -\frac{2\epsilon}{3U_m} . \qquad (5.115)$$

It turns out that this expression is valid for trapped particles in the radiation belts regardless of the equatorial pitch angle α_0 [Dessler and Parker, 1959]. In deriving Equation (5.115) it was assumed that the total energy in the ring current is less than the magnetic field energy U_M. When that is not the case Equation (5.115) is no longer strictly valid and may be in error by up to a factor of two.

By summing up the effects of all the individual particle motions in the geomagnetic field, one arrives at the total magnetic field perturbation

$$\Delta B = \sum_i \int_o^{\pi/2} \sin\alpha_0 d\alpha_0 \int_1^{L_{max}} dL \int_{\epsilon_{min}}^{\epsilon_{max}} d\epsilon \; \Delta B_s \, f_i(\alpha_0, L, \epsilon)$$

$$(5.116)$$

where $f_i(\alpha_0, L, \epsilon)$ is the distribution function for particle species i, expressed as function of equatorial pitch angle, L-shell and energy.

Parker [1957] developed a hydromagnetic formalism that provides an alternative to this extensive integration. One may define the macroscopic particle pressures in the direction parallel and perpendicular to the local magnetic field direction

$$P_\| = \sum_i \iint F_i(X, v, \alpha_0)mv^2\cos^2\alpha_0 dvd\alpha_0 \qquad (5.117)$$

$$P_\perp = \frac{1}{2} \sum_i \iint F_i(X, v, \alpha_0)mv^2\sin^2\alpha_0 dvd\alpha_0 \qquad (5.118)$$

where F_i is the particle distribution function for a particle species i expressed in position, (X), speed, and pitch angle coordinates. The summation is extended over all particle species. The magnetic field pressure is

$$P_m = \frac{B^2}{8\pi} . \qquad (5.119)$$

With these pressure expressions the total gradient-curvature drift current can be written as

$$\mathbf{I}_d = \frac{c}{8\pi P_m} \; \mathbf{B} \times \left\{ \frac{P_\perp}{2P_m} \nabla P_m + \frac{P_\|}{P_\perp} (\mathbf{B} \cdot \nabla)\frac{\mathbf{B}}{8\pi} \right\} ,$$

$$(5.120)$$

where c is the velocity of light [Williams, 1982]. The corresponding gyration current of the particle distribution as a whole is

$$\mathbf{I}_g = \frac{c}{8\pi P} \; \mathbf{B} \times \left\{ \nabla P_\perp - \frac{P_\perp}{2P_m} \nabla P_m \right.$$

$$(5.121)$$

$$\left. - \frac{P_\perp}{P_m} (\mathbf{B} \cdot \nabla)\frac{\mathbf{B}}{8\pi} \right\} .$$

The two terms within the brackets of Equation (5.120) stem from the magnetic field gradient and field curvature respectively, and the three terms within the brackets of Equation (5.121) represent currents driven by the particle pressure gradient, the magnetic field gradient, and the magnetic field line curvature. The total current of all particles then reduces to

$$\mathbf{I} = \mathbf{I}_d + \mathbf{I}_g = \frac{c}{8\pi P_m}\mathbf{B} \times \left\{ \nabla P_\perp + \frac{(P_\| - P_\perp)}{P_m} (\mathbf{B} \cdot \nabla) \frac{\mathbf{B}}{8\pi} \right\}$$

$$(5.122)$$

As a rule of thumb, it requires a total of 4×10^{22} ergs of particle kinetic energy to produce a surface magnetic field depression of $\sim 100nT$ (1 nT $= 1\gamma = 10^{5}G$).

5.7.2 Composition and Sources

The population of trapped particles is made up primarily of electrons, protons, helium ions, carbon ions, and oxygen ions. The composition is found to vary substantially with location (such as L-shell) and with geomagnetic conditions. The heavier ions, such as He^+ and O^+, may be dominant during disturbed conditions on L-shells in the range L = 3 to L = 5, while prolonged quiet periods tend to favor H^+ (protons) above tens of keV energies. The latter is also a reasonable expectation since at typical ring current energies (~ 70 keV) the charge exchange lifetime of H^+ is longer. At lower energies, below a few keV,

the H^+ lifetimes are shorter than that of He^+ and O^+ lifetimes, and the opposite may be true. Figure 5-56 shows a relative comparison of ring current ion flux observations during four different time periods. These results pertain to $\epsilon \leq 20$ keV energies while the ionic composition at higher energies remains to be investigated observationally.

Ionospheric or atmospheric ions probably form a significant fraction of the ring current population. This is inferred from the observations reported by Shelley et al. [1974] and Sharp et al. [1976]. Low-orbiting polar satellites detected the precipitation of oxygen ions (L = 6.8) during distrubed times and also detected field-aligned upward moving accelerated ions from the auroral ionosphere. Sufficient pitch angle scattering at higher altitudes could cause these upward moving ions to become stably trapped and form part of the ring current.
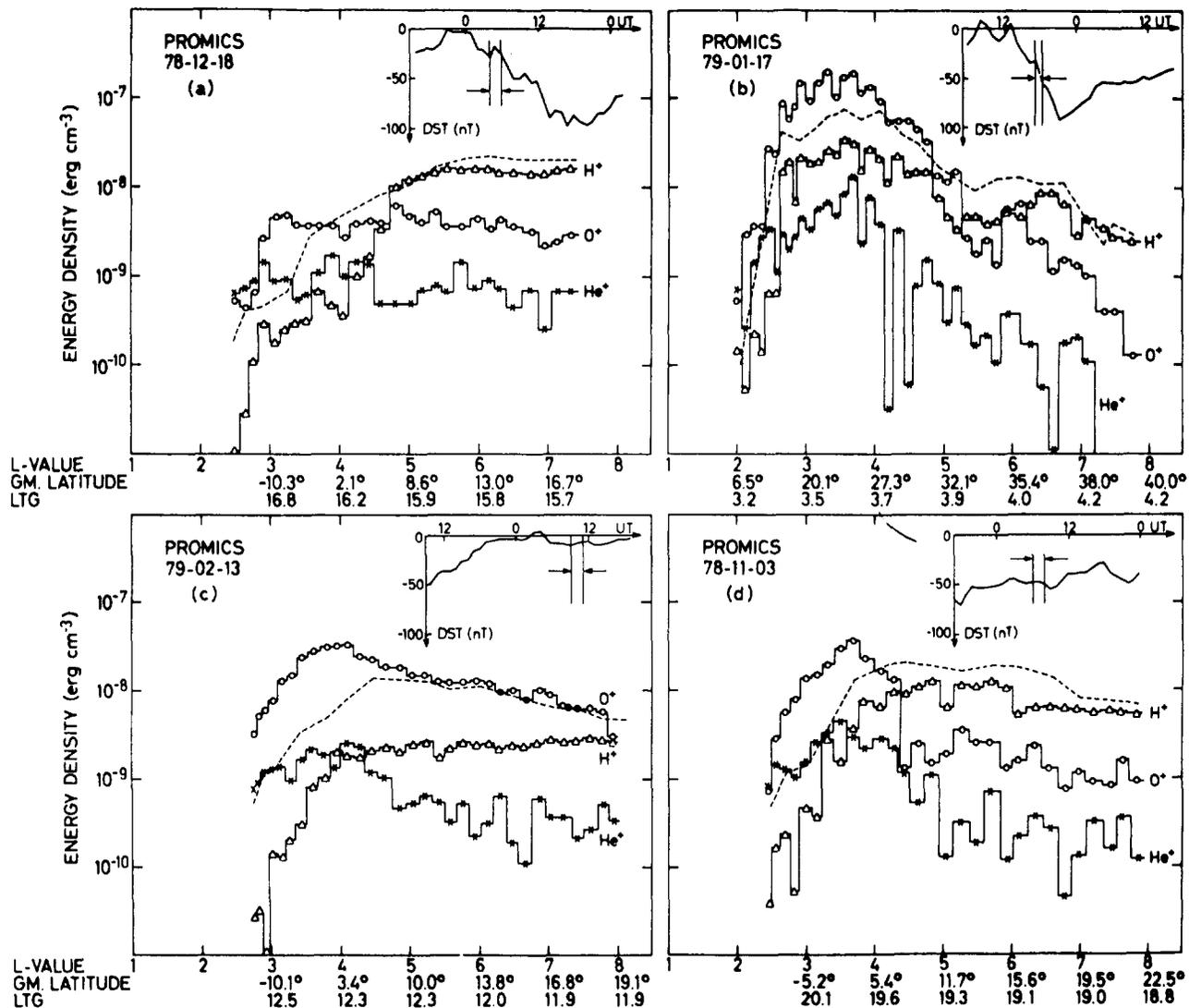
Figure 5-56. Observed energy densities of H^+, He^+ and O^+ ions in the radiation belts at ring current energies (0.2-17 keV/ion) versus orbital parameters. The data were derived from the PROMICS experiment on the PROGNOZ-7 spacecraft. The dashed curves indicate apparent energy densities calculated from a total ion (E/q) spectrometer (at 0.1-45 keV) under the assumption that only protons were measured. The results show the importance of the heavier ions at different times and locations. The four panels represent data for four different periods, and the D_{st}-index history is also shown as a guide to the ring current activity [Lundin et al., 1980].

Based on total ion (no mass resolution) observations, it has become clear that the greatest contribution to the ring current comes from ~20–200 keV ions where the mass composition is yet unknown. This is illustrated in Figure 5-57 [Williams, 1981].
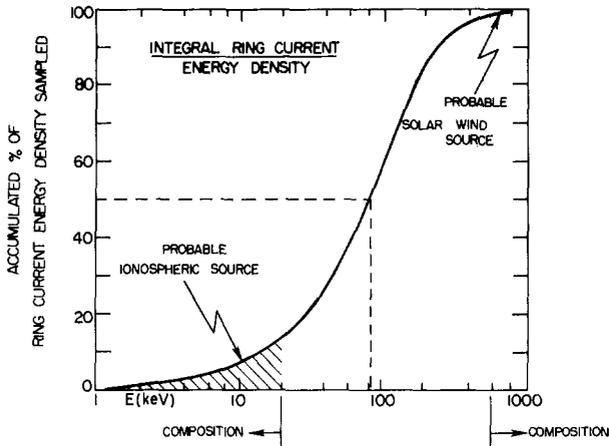

Figure 5-57. Integral representation of the ring current energy density as a function of ion energy. The contribution to the ring current energy density is greater where this curve is steepest. This is also where currently the ionic composition is unknown [Williams, 1981]

A practical measure for the overall strength of the extraterrestrial ring current is the D_{st}-index which measures the middle latitude spatially averaged decrease in the horizontal component H of the earth's surface magnetic field: $D_{st} = \langle \Delta H \rangle$. Under this definition the quiet time ring current corresponds to $D_{st} = 0$. Hourly values of the D_{st} index are published by NASA/National Space Science Data Center, Goddard Space Flight Center, Maryland. Magnetic storms generally have D_{st} depressions on the order of 100 to 200 nT (very large storms may exceed $|D_{st}| = 300$ nT), and the D_{st} index may also fluctuate substantially for other geomagnetic conditions for which $|D_{st}|$ generally remains less than 50 nT. Figure 5-58 shows an example of the D_{st} index plotted for June–December 1972, and the occurrence of four magnetic storm periods in June, August, September and October/November is evident. The D_{st} index is therefore very useful to identify magnetic storms from surface magnetogram records.

5.7.3 Adiabatic Effects Produced by the Ring Current

Much of the time the magnitude of the electrical current set up by the azimuthally drifting radiation belt particles changes slowly in comparison with the ion drift period. Therefore, the third adiabatic invariant, which is proportional to the enclosed magnetic flux threading the drift path, is most often conserved following injection or acceleration. Söraas and Davis [1968] have shown that significant adiabatic effects will take place even for moderate values of D_{st}. To separate the adiabatic and non-adiabatic features one can transform to a $D_{st} = 0$ reference. If $j_1 (\epsilon_1, L_1)$ is the equatorially mirroring flux for $\epsilon = \epsilon_1$ ($L = L_1$, $D_{st} = 0$) and $j_2 (\epsilon_2, L_2)$ is the corresponding flux for $D_{st} \neq 0$ then one has

$$j_2 (\epsilon_2, L_2) = (\epsilon_2/\epsilon_1) \quad j_1 (\epsilon_1, L_1) . \qquad (5.123)$$

This follows from Liouville's theorem which states that the phase space density is constant along dynamical particle trajectories ($f = \text{const.} = j/p^2$). The equatorially mirroring energy ϵ_2 is mapped from the unperturbed ϵ_1 energy by conservation of the first adiabatic invariant:

$$\epsilon_2 = \epsilon_1 \quad (B_2/B_1) \quad , \qquad (5.124)$$

where B_1 is the value of the quiet time magnetic field induction.

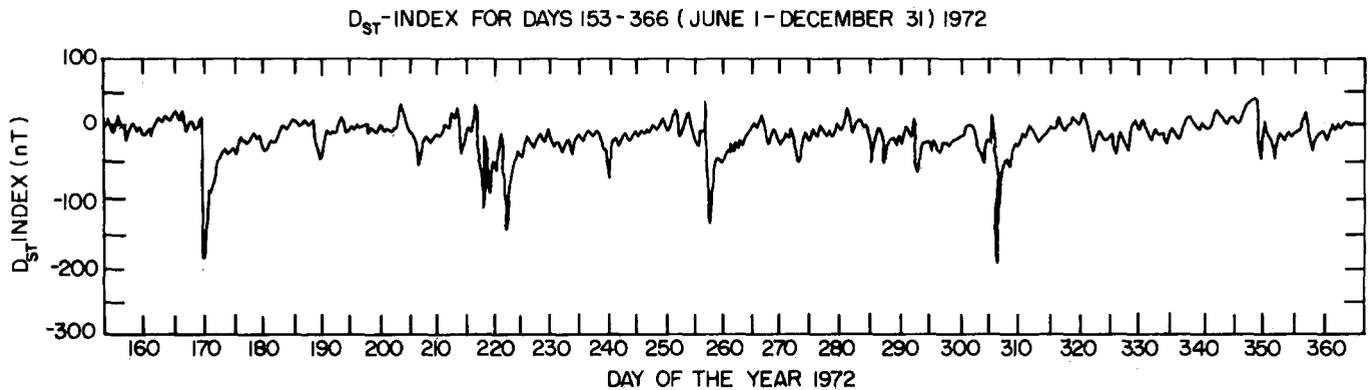Figure 5-58. An example of the time-variation of the horizontal magnetic field component (D_{st}) at the equator. The large rapid drops in D_{st} correspond to a build up of the ring current during magnetic storms followed by subsequent decay.

For a dipole field where $B_E = 0.312$ G

$$B_1 = \frac{B_E}{L_1^3} \qquad (5.125)$$

and

$$B_2 = \frac{B_E}{L_2^3} + \Delta B(r) . \qquad (5.126)$$

The magnetic flux enclosed by the drift path (the third adiabatic invariant) is given by

$$\Phi_1 = 2\pi \int_0^{L_1} \frac{B_E}{L^3} L dL = -2\pi \int_{L_1}^{\infty} \frac{B_E}{L^3} L dL = \frac{-2\pi B_E}{L_1}$$

$$(5.127)$$

and

$$\Phi_2 = -2\pi \, B_E/L_2 + 2\pi \int_0^{L_2} \Delta B(r) \, r dr , \qquad (5.128)$$

where $\Delta B(r)$ is the magnetic field change induced by the ring current enhancement [Soraas and Davis, 1968]. Equation (5.128) uses the fact that the integral from 0 to L includes the return magnetic flux through the earth so that the net dipole magnetic flux through the entire equatorial plane is zero. This fact allows the 0 to L_1 integration interval to be replaced by one for L_1 to ∞. The ions will now equatorially mirror at L_2 where by equating Φ_1, and Φ_2

$$B_E/L_2 = B_E/L_1 + \int_0^{L} \Delta B(r) \, r dr \qquad (5.129)$$

and

$$\Delta B(r) = 0.7 \, D_{st} \, f(r) . \qquad (5.130)$$

The function $f(r)$ is shown in Figure 5-59. For a given D_{st}, L_2 can be found, and hence, B_2. Knowing B_2, ϵ_2 can be determined. In Figure 5-60 we show an illustrative example as presented by Söraas and Davis [1968].

5.8 RADIATION EFFECTS ON SPACE SYSTEMS

Among the known effects of particle radiation on space systems are spacecraft charging phenomena and effects of penetrating radiation on materials. Specific effects include detector malfunction and degradation,
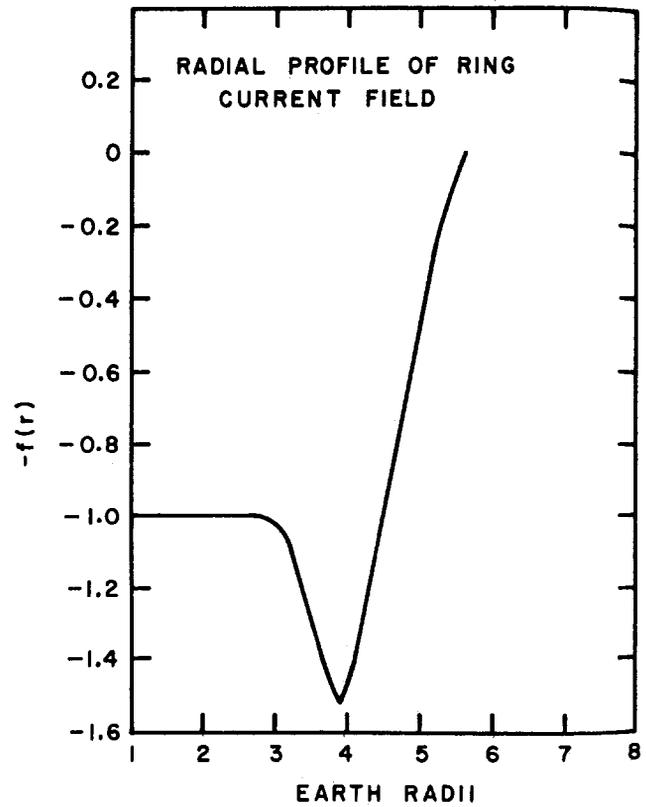
Figure 5-59. The radial dependence of the ring current magnetic field used in the calculation of adiabatic effects on trapped protons by Söraas and Davis [1968]. Notice that the decrease is greatest near L-4.
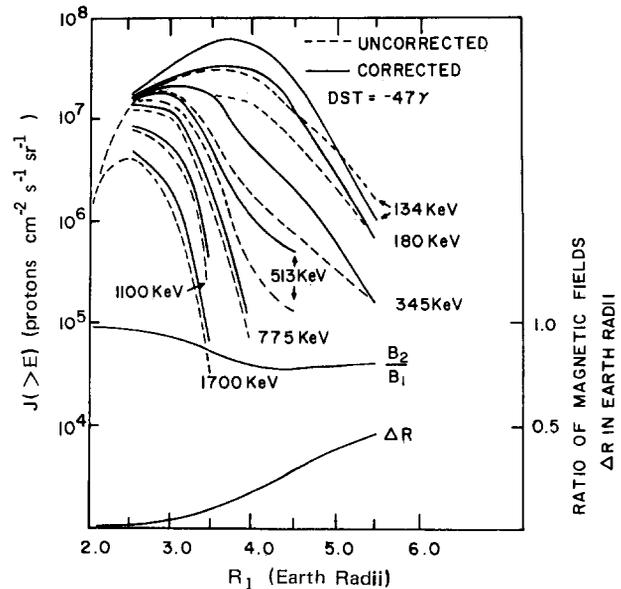
Figure 5-60. The radial proton integral energy intensity profile as measured on day 109 of 1965 when $D_{st} = 46$nT, together with the transformed profile corresponding to $D_{st} = 0$ assuming the three adiabatic invariants of motion conserved. The radial dependence of the ratio between the magnetic field after and before the build up of the ring current and the radial movement ΔR of the particles are shown in the lower part of the figure [Söraas and Davis, 1968].

optical system degradation, memory system alteration, and control system malfunction or failure. For manned space operations, biological effects are a major concern.

A crude measure for damage done by penetrating energetic radiation is *radiation dosage* which is measured in *rads*. This unit is defined as an energy deposition of 100 ergs (6.25×10^7 MeV) in one gram of a material substance. This definition does not distinguish between different kinds of incident radiation or different effects on the material. Radiation dosage is thus only an overall measure, and it is often necessary to examine specific interaction cross-sections when studying radiation effects.

Energy is deposited through chemical (molecular bond changes, bound electron excitation, and ionization) and nuclear (element transmutation, nuclear excitation, and induced radioactivity) interactions. The macroscopic effects are evident in device failure after a critical level of radiation exposure is reached. Most often this critical level depends directly on the nature and energy characteristics of the incident radiation.

A major concern is the on orbit lifetime of microelectronic devices that are designed to a specific level of radiation "hardness" (such as 10^4-10^5 rad). There is in many cases a trade off between orbit choice and system lifetime that must be determined.

A lowest order approximation to the expected radiation exposure effects can be estimated by combining the energy deposition rate versus incident energy curves of Janni and Radke [1979] with the expected radiation belt flux intensity deduced from previous observations, as in Section 5.6 or from theoretical modeling. A simple (but very crude) approach to estimating the radiation dosage follows.

It is assumed that shielding is equal in all directions so that a spherical shield approximation can be used. The shielding is also assumed to be aluminum or close to it in density. The incident omnidirectional particle fluxes are normalized (or scaled) to unity at a selected energy so that dosage need only be calculated as a function of spectral shape. The dose rate for a given energy spectrum is found by multiplying the resulting dosage by the model (or measured) omnidirectional flux at the selected energy. Total dosage is determined by integrating over the expected exposure time of the satellite.

Figure 5-61 shows a number of exponential spectral radiation curves normalized to unity at 1 MeV for energetic electrons up to 6 MeV. By picking the one curve that most nearly approximates the actual expected radiation energy spectrum, one has a one-parameter spectral representation, the spectral e-folding energy E_0. One then proceeds to calculate the radiation exposure for the normalized spectrum behind a certain thickness of shielding by using the curves in Figure 5-62. This process has to be averaged over the expected radiation conditions for the expected spacecraft orbit during the period of the desired orbital operations.
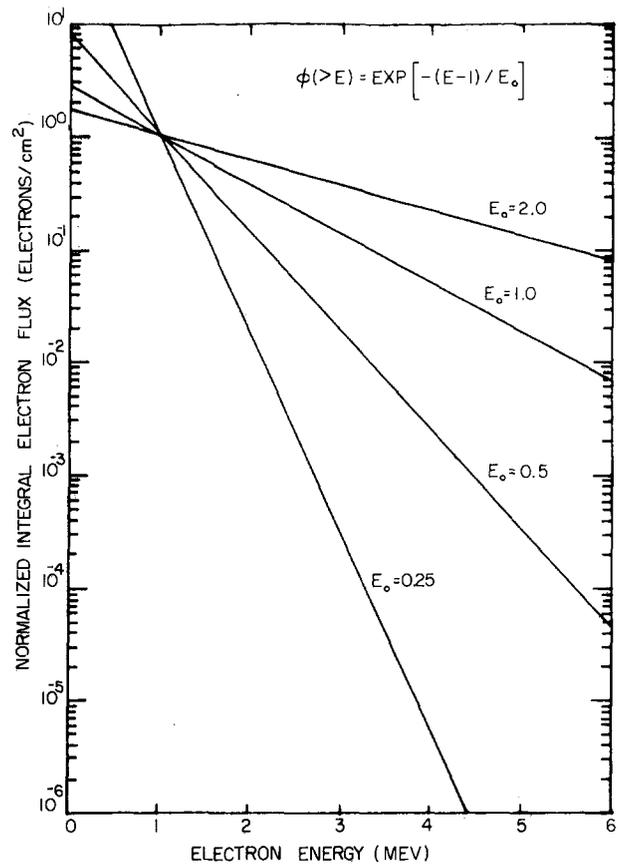

Figure 5-61. Model electron spectra for engineering applications: Normalized integral omnidirectional electron flux as a function of electron energy. By matching a model energy spectra to the curves the appropriate E_0 can be quickly found. The flux at 1 MeV is normalized to 1 electron/cm^2 [Janni and Radke, 1979].

A similar technique also applies to ions. For protons, Figure 5-63 shows a similar set of exponential spectral radiation curves extending to 300 MeV, and Figure 5-64 gives the radiation exposure dosage as function of the aluminum shielding thickness. Notice that the shielding is generally less effective in reducing the radiation dosage due to the very energetic ions in the radiation belts.

5.8.1 Detector Malfunctions

Single particle upsets occur when a single particle creates enough free electrons to simulate a device logic state change. Single particle effects are particularly severe in small ($<$10 μm) sensitive regions of microelectronic devices. Figure 5-65 illustrates the incidence of a cosmic ray (very energetic heavy ion) in a single memory cell commonly used for onboard information storage. Notice that the volume where the ionization takes place is at least comparable to the sensitive cell region itself. It is presently an area of controversy whether reduction in cell size will always increase the soft error or single event upset rate; it is conceivable that with very small memory cells the ionization volume could encompass many cells.
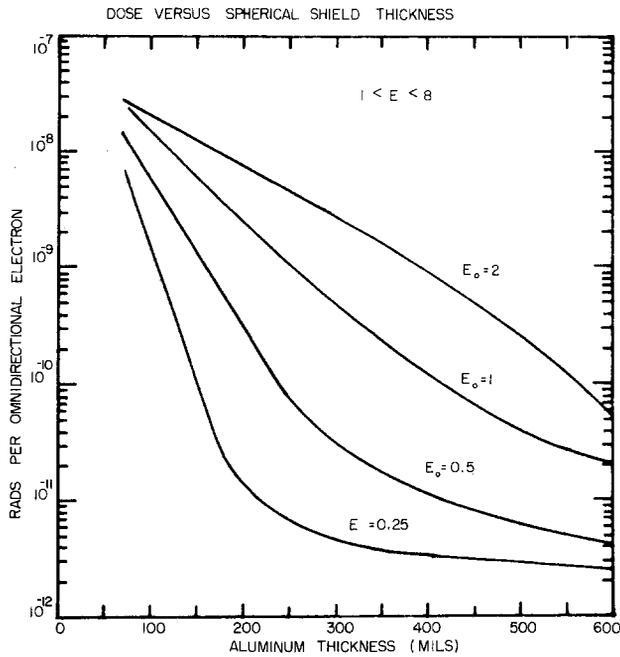
DOSE VERSUS SPHERICAL SHIELD THICKNESS

Figure 5-62. Radiation dosage experienced behind various shielding thicknesses of aluminum absorber for several incident electron energy spectra normalized to 1 electron/cm² at 1 MeV. Multiplication by the 1 MeV flux gives the expected radiation dose rate [Janni and Radke, 1979].

On the average, the effect of single-particle incidence on detector materials, such as aluminum and silicon, is the generation of one electron-hole pair per 3.6 eV of energy deposition. Thus, 1 rad of incident radiation in 1 gram of material creates 1.74×10^{13} electron-hole pairs. Even a moderately energetic radiation belt particle (for example 1 MeV) will create a large number of free charge carriers in the detector material and may lead to false signals. Prolonged exposure to energetic particles degrades the detector performance by the accumulation of material microstructural damage. For example, solid state detectors of the Al-Si-Au variety are found to have a factor of 10 increase in useful lifetime when the aluminum side is facing the radiation exposure (compared to the gold side). Very energetic and very heavy cosmic ray ions have a particularly devastating effect on detector systems; for further details see Adams and Partridge [1982] and McNulty [1981].

Figure 5-66 shows an example of a nuclear interaction occurring near a sensitive region of a radiation particle detector or other solid state device. An incident proton, for example, will stimulate a ^{28}Si nucleus to emit an alpha particle which has a short range. The recoiling ^{28}Si nucleus stops in even a much shorter distance. The combined effect can deposit tens of MeV in a small $(10 \times 20 \times 20)$ μm volume element creating a "soft" (data) error. Accelerator data [McNulty et al., 1980] indicate that the proton induced (E > 40 MeV) soft error rate is less than 10^{-6} soft errors/(protons-cm²). An upper

$$\phi(>E) = EXP\left[-(E-30)/E_o\right]$$
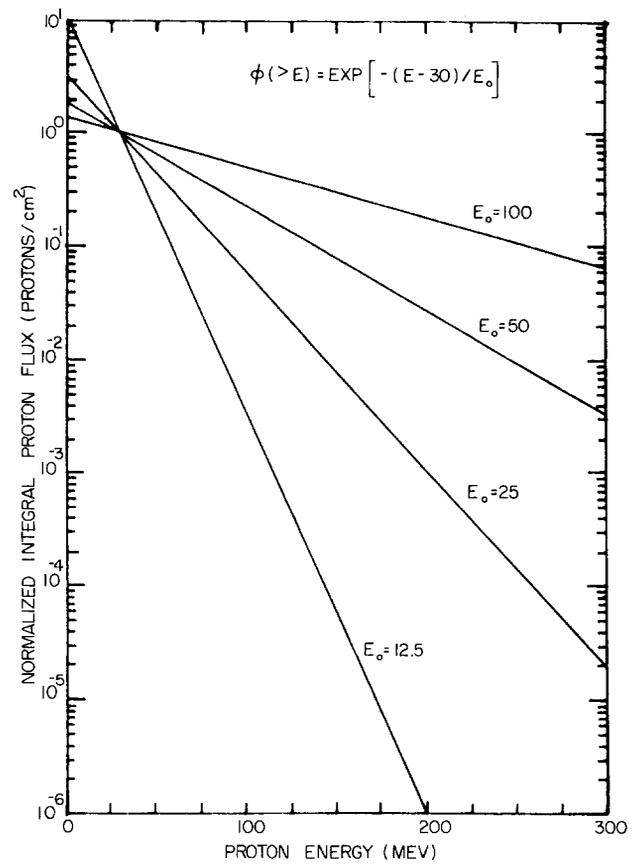
Figure 5-63. Model proton spectra for engineering applications: Normalized integral proton flux curves for estimating E_o where the flux at 30 MeV is normalized to 1 proton/cm² [Janni and Radke, 1979].

DOSE VERSUS SPHERICAL SHIELD THICKNESS

$$\phi(>E) = EXP[-(E-30)/E_o]$$
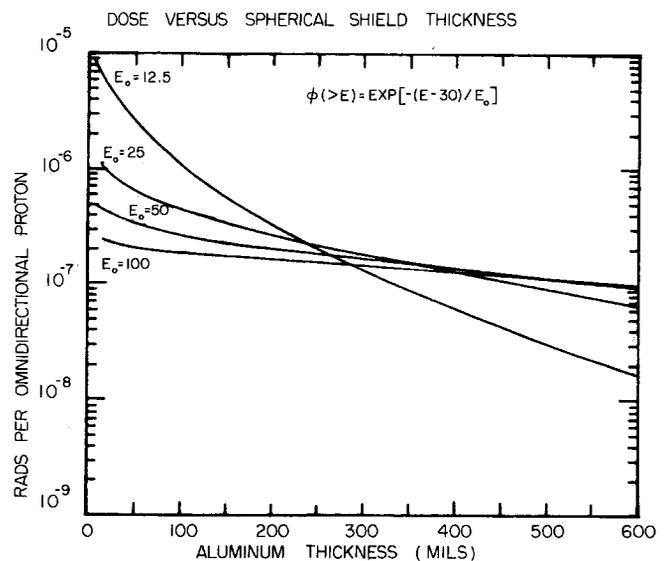
Figure 5-64. Radiation dosage experienced behind various shielding thicknesses of aluminum absorber for several incident proton spectra normalized to 1 proton/cm² at 30 MeV. Multiplication by the omnidirectional flux at 30 MeV will give the radiation dose rate [Janni and Radke, 1979].

SCHEMATIC REPRESENTATION OF SENSITIVE REGION

IN A SINGLE MEMORY CELL
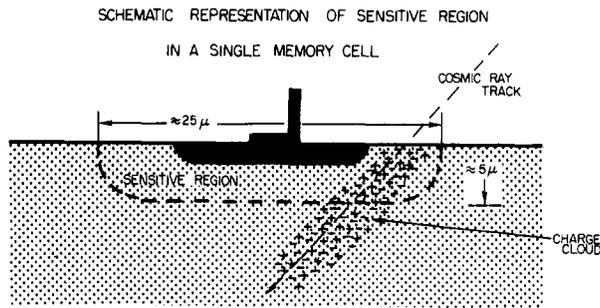
Figure 5-65. Illustration of radiation effect: Electron-hole generation near a sensitive region as a result of local ionization produced by a traversing cosmic ray or energetic particle [B. Blake, personal communication, 1982].

Figure 5-66. Illustration of the production of numerous secondary particles from the nuclear interaction of the primary particle in a sensitive volume of a solid state detector device [McNulty et al., 1980].

limit to the expected error rate (error/sec), therefore, can be found by using the proton flux models for $E > 40$ MeV times 10^{-6}. If trapped heavy ion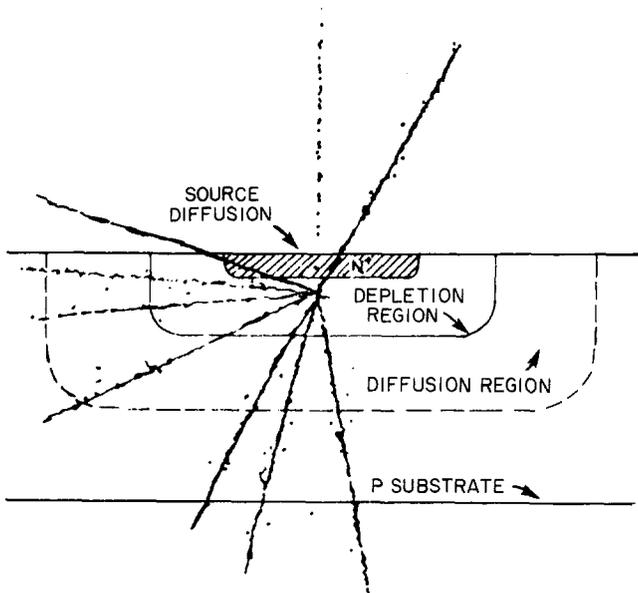s are sufficiently abundant they could dominate the soft error rate [Adams et al., 1981]. This is one of several purely practical motivations for measuring the energetic trapped particle composition to an adequate degree of accuracy.

5.8.2 Memory Alteration

Certain microcircuitry used in current spacecraft instrumentation has proven very susceptible to the effects of energetic heavy ions in the radiation belts and in the cosmic radiation. Memory chips and microprocessors are frequently found to have their logical states and information content severely altered by the localized energy

deposition process. Similar effects can result from alpha-particle emission from nuclear interactions and from natural and induced radioactivity in the devices themselves.

If the effects are infrequent in occurrence, engineering design emphasizing redundance of the critical components could circumvent the problem. However, when the effects are frequent and/or persistent this approach may not be feasible.

Figure 5-67 [E. Petersen, personal communication, 1982] shows the energy deposited in a 10 μm — thick sensitive region by different ions over a range of incident energies. The vertical scale on the right denotes the number of electrons produced. As a circuit becomes smaller and more complex, less deposited energy (charge) is needed to trigger errors.
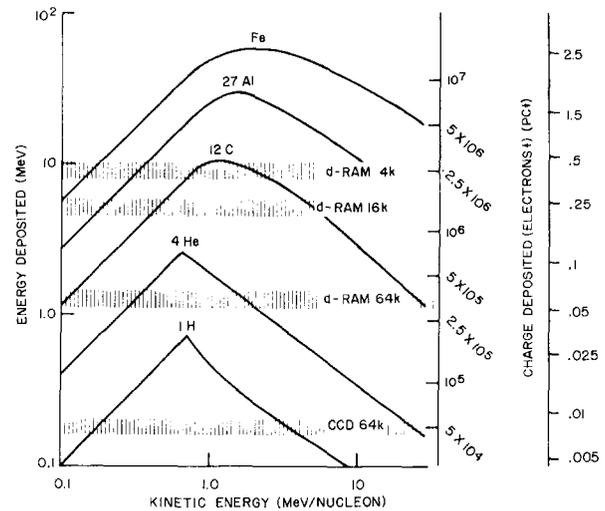
Figure 5-67. Energy deposited in 10 μm of silicon by different ions. The scale on the right shows the number of free electrons released. The low energy part of the curve occurs when the ion penetrating range is less than 10 μm so that it deposits all its energy [E. Petersen, personal communication, 1982].

5.8.3 Control System Failure

Radiation induced errors in electronic circuitry can be particularly damaging when they occur in critical circuitry such as control systems or in decision making logic. While other non-critical circuits may continue to function with false information, control systems can latch-up, that is, be switched into an undesired mode from which there may be no reset option, or the spacecraft may be damaged. Certain circuitry switching may cause burnout of electrical systems or even worse effects, particularly when propulsion, attitude, or weapons systems may be involved. For these reasons it is imperative that proper safeguards and redundancy design be considered in the early stages of spacecraft engineering.

5.8.4 Biological Effects

There is extensive literature on space biology [see for example Bacq and Alexander, 1961]. Here we shall only point out that the quiet time radiation belts at some locations present a lethal radiation dosage to a man in a space suit or even within a vehicle. But even outside the main trapped radiation zone, there are intermittent high fluxes of solar energetic particles. For example, it is believed that the energetic particle fluxes associated with the August 1972 solar flare/magnetic storm event would have been extremely harmful to humans almost anywhere in space. The method presented above can also be used to estimate human radiation exposure behind different shielding designs. A definitely lethal dosage is about 500 rads [Desrosier and Rosenstock, 1960].

5.9 MAN'S IMPACT ON THE RADIATION BELTS

The activity of mankind can, to a significant degree, influence the earth's radiation environment. Examples are nuclear detonations (fission and fusion), accelerator particle beams (neutral and charged), release of chemical substances, injection of metallic powders, and electromagnetic wave energy production. The effects of some of these modification sources have not yet been studied, but for others a substantial body of data is available.

5.9.1 Nuclear Detonations

A vast number of free neutrons and other particles and a great pulse of electromagnetic energy are released in nuclear explosions. In the nuclear fission process, the fission fragments also carry significant kinetic energy. The product of nuclear fusion is generally a stable particle (He) which may be ionized. As a rule of thumb $\sim 10^{26}$ fast neutrons (each of which decay into a proton-electron-neutrino triplet) are released per megaton nuclear explosive yield.

The size of the nuclear fireball depends not only on the explosive yield, but also on the medium in which the detonation occurs. In field-free empty space the fireball will expand without limits, but in the presence of material substances or a magnetic field the fireball is effectively restrained. In a dense gas (such as below ~ 100 km in the earth's atmosphere), collisions between the explosion products and the atmospheric constituents dissipate much of the detonation energy as heat. About half of this energy is radiated away and the thermalized remainder is typically at 6000 K to 8000 K [Zinn et al., 1966]. At an altitude of 60 km in the earth's atmosphere, a 1 megaton fissional detonation will have a fireball radius of ~ 4 km, and for the same nuclear explosive yield this radius will be smaller close to the ground. The fireball itself may accelerate to velocities of several km/sec due to buoyancy and shock processes. High altitude and space detonations (more than 100 km above the earth) have the fireball size limited by the magnetic field. This occurs because the explosion generates electrically charged fragments that are susceptible to the magnetic force, $q\mathbf{V} \times \mathbf{B}$, where q is the particle charge and $\mathbf{V}$ its velocity. A nuclear detonation of 1 megaton can have fireball expansion to ~ 1000 km across the magnetic field when the B-field has a value $B \approx 0.5$ G. The expansion is not magnetically limited along the field lines.

Depending on the location of the nuclear detonations, a certain fraction of the neutrons will decay within the magnetic field trapping region, and the decay products will thus constitute artificially created trapped radiation. For nuclear fission, the fission fragments also emit particles (such as electrons and α-particles) before reaching a nucleonic configuration as a stable isotope. This process further contributes to the trapped radiation, and the characteristic electron energy is 1 to 8 MeV from this source.

Studies of nuclear detonation effects have shown that even small high altitude explosions (in the kiloton range) affect the radiation belts considerably. See for example reviews by Hess [1968] and Walt [1977]. Table 5-4 gives an overview of the known radiation belt effects of the Teak, Orange, Argus 1, Argus 2, Argus 3, and Starfish nuclear detonations carried out at high altitudes by the United States, and the USSR-1, USSR-2 and USSR-3 high altitude nuclear detonations by the Soviet Union.

Energetic charged particles exiting the upper atmosphere along the geomagnetic lines of force are generally within the atmospheric bounce loss cone. In the absence of significant pitch angle scattering, such particles will follow the field lines and precipitate into the conjugate hemisphere. Empirically, a significant fraction of the nuclear detonation particles become trapped in the radiation belts. This implies that significant pitch angle scattering must take place from the angular source cone region $(\alpha_0 < \alpha_{OLC})$ to stably trapped particle orbits $(\alpha_0 > \alpha_{OLC})$. This pitch angle scattering must take place on the time scale of a single half-bounce period $\tau_b/2$ (which is of the order of seconds).

Following such an artificial injection of particles into the radiation belts, the normal radiation belt radial and pitch angle diffusion mechanisms will operate. The initial narrow injected radial distribution will broaden, and the charge exchange (for ions) and Coulomb energy degradation mechanisms will modify the characteristics of the injected distributions. Depending on the location, the artificial radiation belts may last for days or years [Walt and Newkirk, 1966; Stassinopoulos and Verzariu, 1971].

The effects of accelerator beams are likely to be similar to those of the nuclear detonation particles, but the yield (in terms of number of particles) is likely to be much smaller. On the other hand, since the beam particles may be generated over a wide range of energies

Table 5-4. Listing of high altitude nuclear detonations between 1958 and 1962 [Walt, 1977].

Event	Altitude (km)	Time (UT)	Date	Latitude	Longitude	Approximate L-Value Detonation	Yield	Characteristics of Band	Approximate Decay Time
Teak	76.8	10:50:05	01AUG58	17°N	169°W	1.12	MT Range	Low Altitude	few days
Orange	42.97	10:30:08	12AUG58	17°N	169°W	1.12	MT Range	Low Altitude	1 day
Argus 1	200	2:30:00	27AUG58	38°S	12°W	1.7	1-2 KT	Narrow Band	0-20 days
Argus 2	250	3:20:00	30AUG58	50°S	8°W	2.1	1-2 KT	Narrow Band	10-20 days
Argus 3	500	22:10:00	06SEP58	50°S	10°W	2.0	1-2 KT	Narrow Band	10-20 days
Starfish	400	09:00:29	09JUL62	16.7°N	190.5°E	1.12	1.4 MT	Wide Distribution	1-2 yrs
USSR 1	—	03:40:46	22OCT62	—	—	1.8	—	Wide Distribution	30 days
USSR 2	—	04:41:18	28OCT62	—	—	1.8	—	Wide Distribution	30 days
USSR 3	—	09:13	01NOV62	—	—	1.75	—	Narrow Band	30 days

(thermal to relativistic) a more precise study of their effects is warranted.

5.9.2 Release of Chemicals

Chemical releases for research purposes have been carried out at high altitudes. In most cases barium or lithium was released to trace magnetic field lines locally and to assess the magnitude of electric fields and upper atmosphere winds. Chemical releases into outer regions of geospace are also planned. Such programs may modify the environment locally (for example, by altering plasma wave dispersion characteristics), but are not expected to impact the radiation belts seriously unless large quantities of chemicals are used.

Extensive operations with rocket propulsion or special ion engines could, however, drastically alter the different particle populations and could lead to profound changes in the radiation belt structure. See Chapter 7. To date no comprehensive environmental impact analysis has been carried out.

5.9.3 Transmission of Radio Waves

It has been suggested that electromagnetic wave energy from tropospheric thunderstorm activity and whistler-mode waves from VLF radio transmitters can perturb the energetic electron component of the earth's radiation belts. Correlative studies indicate that energetic electron precipitation not only occurs from natural sources [Spjeldvik and Lyons, 1979] but also in correlation with strong terrestrial radio transmitter operations [Vampola and Kuck, 1978; Park et al., 1981; Imhof et al., 1981; Chang and Inan, 1983]. Precisely to what extent man's electromagnetic wave generation influences the overall radiation belt structure is not known, however.

5.9.4 Effects of Space Structures

Proposed operations of large manmade metallic and electrically insulated space structures will produce local "singular" regions in the magnetosphere. Associated with space shuttles, space platforms, or space power arrays will be a hydromagnetic wake in which the wave and particle behavior will go through a sudden change. It is not known whether or not these cavity phenomena may have a significant effect on the radiation belts themselves. For some details see Garrett and Pike [1980] and references therein.

CHAPTER 5

REFERENCES

Adams, J.H., Jr. and K. Patridge, "Do Trapped Heavy Ions Cause Soft Upsets on Spacecraft?" National Research Laboratory Memo. Rept. 4846, October 12, 1982.

Adams, J.H., Jr., R. Silverberg, and C.H. Tsao, "Cosmic Ray Effects on Microelectronics, Part I: The Near-Earth Particle Environment," National Research Laboratory Memo. Rept. 4506, August 25, 1981.

Akasofu, S.-I., *Polar and Magnetospheric Substorms,* D. Reidel, Dordrecht, Holland, 1968.

Alfvén, H. and C.G. Fälthammar, *Cosmical Electrodynamics,* Clarendon Press, Oxford, UK, 1963.

Axford, W.I., "Magnetospheric Convection," *Rev. Geophys.,* **1:** 421, 1969.

Bacq, Z.M. and P. Alexander, *Fundamentals of Radiology,* Pergamon Press, New York, 1961.

Baker, D.N., P.R. Higbie, E.W. Hones, Jr., and R.D. Belian, "High Resolution Energetic Particle Measurements at 6.6 R_E 3. Low Energy Anisotropies and Short-Term Substorm Predictions," *J. Geophys. Res.,* **83:** 4863, 1978.

Baker, D.N., P.R. Higbie, and R.D. Belian, "Multispacecraft Observations of Energetic Electron Flux Pulsations at 6.6 R_E," *J. Geophys. Res.,* **85:** 6709, 1980.

Baker, D.N. et al., "The Los Alamos Geostationary Orbit Synoptic Data Set," Los Alamos National Laboratory Report LA-8843, UC-34G, Los Alamos, N.M., August 1981.

Belian, R.D., D.N. Baker, P.R. Higbie, and E.W. Hones, Jr., "High-Resolution Energetic Particle Measurements at 6.6 R_E 2. High Energy Proton Drift Echoes," *J. Geophys. Res.,* **83:** 4857, 1978.

Belian, R.D., D.N. Baker, E.W. Hones, Jr., P.R. Higbie, S.J. Bame, and J.R. Asbridge, "Timing of Energetic Proton Enhancements Relative to Magnetospheric Substorm Activity and Its Implication for Substorm Theories," *J. Geophys. Res.,* **86:** 1415, 1981.

Blake, J.B. "Experimental Test to Determine the Origin of Geomagnetically Trapped Radiation," *J. Geophys. Res.,* **78:** 5822, 1973.

Blake, J.B., and J.F. Fennell, "Heavy Ion Measurements in the Synchronous Altitude Region," *Planet. Space Sci.,* **29:** 1205, 1981.

Bostrom, C.O., D.S. Beall, and J.C. Armstrong, "Time History of the Inner Radiation Zone," *Models of the Trapped Radiation Environment, Vol. III: Longterm Variations,* NASA SP-3024, 1971.

Brinkmann, H.C. and H.A. Kramers, "Zur Theorie der Einfangung von Elektronen Durch α-Teilchen," *Proc. Akad Wetensch. Amsterdam Afd. Natuurk,* **33:** 973, 1930.

Chandrasekhar, S., "Plasma Physics" (compiled by S.K. Trehan), *Phoenix Science Series,* University of Chicago Press, Chicago, 1965.

Chang, H.C. and U.S. Inan, "Quasi-Relativistic Electron Precipitation Due to Interactions With Coherent VLF Waves in the Magnetosphere," *J. Geophys. Res.,* **88:** 318, 1983.

Chapman, S. and J. Bartels, *Geomagnetism,* Oxford University Press, London, 1940.

Claflin, E.S., "Change Exchange Cross Sections for Hydrogen and Helium Ions Incident on Atomic Hydrogen: 1 to 1000 keV," Rep Tr-0059 (6260-20)-1, Aerospace Corp., El Segundo, Calif., 1970.

Cornwall, J.M., "Diffusion Processes Influenced by Conjugate Point Wave Phenomena," *Radio Sci.,* **3:** 740, 1968.

Cornwall, J.M., "Radial Diffusion of Ionized Helium and Protons: A Probe for Magnetospheric Dynamics," *J. Geophys. Res.* **77,** 1756, 1972.

Davidson, G.T., "The Motion of Charged Particles in the Earth's Magnetic Field," in *The Trapped Radiation Handbook,* edited by J.B. Cladis, G.T. Davidson, and L.L. Newkirk, Lockheed Palo Alto Research Laboratory, DNA 25241H, 1977.

Desrosier, N.W. and H.M. Rosenstock, *Radiation Technology in Food, Agriculture and Biology,* Avi, Westport, Conn., 1960.

Dessler, A.J. and E.N. Parker, "Hydromagnetic Theory of Geomagnetic Storms," *J. Geophys. Res.,* **64:** 2239, 1959.

Fälthammar, C.G., "Radial Diffusion by Violation of the Third Adiabatic Invariant," in *Earth's Particles and Fields,* edited by B.M. McCormac, Reinhold, New York, 1968.

Fennell, J.F., D.R. Croley, Jr., and S.M. Kaye, "Low-Energy Ion Pitch Angle Distributions in the Outer Magnetosphere: Ion Zipper Distribution," *J. Geophys. Res.,* **86:** 3375, 1981.

Fite, W.L., R.F. Stebbings, D.J. Hummer, and R.T. Brackman, "Transfer in Proton-Hydrogen Atomic Collisions," *Phys. Rev.,* **119:** 663, 1960.

Fritz, T.A. and W.N. Spjeldvik, "Simultaneous Quiet Time Observations of Energetic Radiation Belt Protons and Helium Ions: The Equatorial α/p Ratio Near 1 MeV," *J. Geophys. Res.,* **84:** 2608, 1979.

Fritz, T.A. and B. Wilken, "Substorm Generated Fluxes of Heavy Ions at the Geostationary Orbit," in *Magnetospheric Particles and Fields,* edited by B.M. McCormac, D. Reidel, Dordrecht, Holland, 1976.

Garrett, H.B., "Quantitative Models of the 0 to 100 keV Mid-Magnetospheric Particle Environment," in *Quantitative Modeling of Magnetospheric Processes,* edited by W.P. Olson, AGU, Washington, D.C., 1979.

Garrett, H.B. and C.P. Pike, (eds.) *Space Systems and Their Interactions with Earth's Space Environment,* AIAA Press, New York, 1980.

Hamlin, D.A., R. Karplus, R.C. Vik, and K.M. Watson, "Mirror and Azimuthal Drift Frequencies for Geomagnetically Trapped Particles," *J. Geophys. Res.,* **66:** 1, 1961.

Harel, M., R.A Wolf, P.H. Reiff, R.W. Spiro, W.J. Burke, F.J. Rich, and M. Smiddy, "Quantitative Simulation of a Magnetospheric Substorm 1. Model logic and overview," *J. Geophys. Res.,* **86:** 2217, 1981a.

Harel, M., R.A Wolf, R.W. Spiro, P.H. Reiff, C.K. Chen, W.J. Burke, F.J. Rich, and M. Smiddy, "Quantitative Simulation of a Magnetospheric Substorm 2. Comparison With Observations," *J. Geophys. Res.,* **86:** 2242, 1981b.

Hess, W. N., *The Radiation Belt and Magnetosphere*, Blaisdell, Waltham, Mass., 1968.

Higbie, P.R., R.D. Belian, and D.N. Baker, "High-Resolution Energetic Particle Measurements at 6.6 R_E 1. Electron Micropulsations," *J. Geophys. Res.*, **83:** 4851, 1978.

Hovestadt, D., G. Gloeckler, C.Y. Fan, L.A. Fisk, F.M. Ipavich, B. Klecker, J.J. O'Gallagher, and M. Scholer, "Evidence for Solar Wind Origin of Energetic Ions in Earth's Radiation Belts," *J. Geophys. Res. Letts.*, **5:** 1055, 1978.

Hovestadt, D., B. Klecker, E. Mitchell, J.F. Fennell, G. Gloeckler, and C.Y. Fan, "Spatial Distribution of Z $\geqq$ 2 Ions in the Outer Radiation Belt During Quiet Conditions," *Adv. Space Res.*, **1:** 305, 1981.

Imhof, W.L., E.E. Gaines, and J.B. Reagan, "High-Resolution Spectral Features Observed in the Inner Radiation Belt Trapped Electron Population," *J. Geophys. Res.*, **86:** 2341, 1981.

Jackson, J.D., *Classical Electrodynamics, 2nd edition,* Wiley, New York, 1975.

Jacobs, J.A., *Geomagnetic Micropulsations*, Springer-Verlag, New York, 1970.

Janni, J. and G. Radke, "The Radiation Environment and Its Effects on Spacecraft in *Quantitative Modeling of Magnetospheric Processes,*" edited by W.P. Olson, Geophysical Monograph 21, AGU, Washington, D.C. 1979.

Kaye, S.M., E.G. Shelley, R.D. Sharp, and R.G. Johnson, "Ion Composition of Zipper Events," *J. Geophys.*, **86:** 3383, 1981.

Kennel, C.F. and F. Engelmann, "Velocity Space Diffusion from Weak Plasma Turbulence in a Magnetic Field," *Phys. Fluids,* **9:** 2377, 1966.

Kennel, C.F. and H.E. Petschek, "Limit on Stably Trapped Particle Fluxes," *J. Geophys. Res.*, **71:** 1, 1966.

Kennel, C.F., L.J. Lanzerotti, and E.N. Parker, (eds.) *Solar System Plasma Physics,* Vols. I–III, North Holland, Amsterdam, 1979.

Kivelson, M.G., S.M. Kaye, and D.J. Southwood, "The Physics of Plasma Injection Events," *Dynamics of the Magnetosphere*, edited by S.-I. Akasofu, D. Reidel, Dordrecht, Holland, 1980.

Lanzerotti, L.J., D.C. Webb, and C.W. Arthur, "Geomagnetic Field Fluctuations at Synchronous Orbit 2. Radial Diffusion," *J. Geophys. Res.*, **83:** 3866, 1978.

Lerche, I., "Quasilinear Theory of Resonant Diffusion in a Magneto-Active Relativistic Plasma," *Phys. Fluids,* **11:** 1720, 1968.

Lo, H.H. and W.L. Fite, "Electron-Capture and Loss Cross Sections for Fast, Heavy Particles Passing Through Gases," *Atomic Data,* **1:** 305, 1970.

Lundin, R., L.R. Lyons, and N. Pissarenko, "Observations of the Ring Current Composition at L-Values less than 4," *Geophys. Res. Lett.*, **7:** 425, 1980.

Lyons, L.R., "Plasma Processes in the Earth's Radiation Belts," in *Solar System Plasma Physics,* edited by C.F. Kennel, L.J. Lanzerotti, and E.N. Parker, North Holland, Amsterdam, 1979.

Lyons, L.R. and R.M. Thorne, "The Magnetospheric Reflection of Whistlers," *Planet. Space Sci.*, **18:** 1753, 1970.

Lyons, L.R. and R.M. Thorne, "Equilibrium Structure of Radiation Belt Electrons," *J. Geophys. Res.*, **78:** 2142, 1973.

Lyons, L.R., R.M. Thorne, and C.F. Kennel, "Electron Pitch-Angle Diffusion Driven by Oblique Whistler Mode Turbulence," *J. Plasma Phys.*, **6:** 589, 1971.

Lyons, L.R., R.M. Thorne, and C.F. Kennel, "Pitch Angle Diffusion of Radiation Belt Electrons Within the Plasmasphere," *J. Geophys. Res.*, **77:** 3455, 1972.

Lyons, L.R. and D.J. Williams, "A Source for the Geomagnetic Storm Main Phase Ring Current," *J. Geophys. Res.*, **85:** 523, 1980.

MacDonald, J.R. and F.W. Martin, "Experimental Electron-Transfer Cross Sections for Collisions of Oxygen Ions in Argon, Nitrogen and Helium at Energies of 7–40 MeV," *Phys. Rev. (Sect. A),* **4:** 1965, 1971.

McIlwain, C.E., "Coordinates for Mapping the Distribution of Magnetically Trapped Particles," *J. Geophys. Res.* **66:** 3681, 1961.

McIlwain, C.E., "Redistribution of Trapped Protons During a Magnetic Storm," *Space-Research V*, North Holland, Amsterdam, 1965.

McNulty, P.J., R.C. Wyatt, G.E. Farrell, R.C. Filz and P.L. Rothwell, "Proton Upsets in LSI Memories in Space," in Prog. Astronaut. Aeronaut. Vol. 71, *Space Systems and Their Interactions with Earth's Space Environment,* edited by H.B. Garrett and C.P. Pike, AIAA Press, New York, 1980.

Mott, N.F. and H.S.W. Massey, *The Theory of Atomic Collisions,* Clarendon Press, Oxford, UK, 1952.

Mullen, E.G. and M.S. Gussenhoven, "SCATHA Environmental Atlas," AFGL TR-83-0002, ADA131456, 1938.

Park, C.G., C.S. Lin, and G.K. Parks, "A Ground-Satellite Study of Wave-Particle Correlations," *J. Geophys. Res.*, **86:** 37, 1981.

Parker, E.N., "Newtonian Development of the Dynamical Properties of Ionized Gases of Low Density," *Phys. Rev.*, **107:** 924, 1957.

Parsignault, D.R., E. Holeman, and R.C. Filz, "Solar Cycle Modulation of the 55-MeV Proton Fluxes at Low Altitudes," *J. Geophys. Res.*, **86:** 11439, 1981.

Paulikas, G.A. and J.B. Blake, "Effects of the Solar Wind on Magnetospheric Dynamics: Energetic Electrons at the Synchronous Orbit," in *Quantitative Modeling of Magnetospheric Processes,* edited by W.P. Olson, AGU, Washington D.C. 1979.

Retterer, J.M., J.R. Jasperse, and T.S. Chang, "A New Approach to Pitch Angle Scattering in the Magnetosphere," *J. Geophys. Res.*, **88:** 201, 1983.

Roederer, J.G., *Dynamics of Geomagnetically Trapped Radiation,* Springer-Verlag, New York, 1970.

Rossi, B. and S. Olbert, *Introduction to the Physics of Space,* McGraw-Hill, New York, 1970.

Rothwell, P.L. and L. Katz, "Enhancement of 0.24–0.96 MeV Trapped Protons During May 25, 1967 Magnetic Storm," *J. Geophys. Res.*, **78:** 5490, 1973.

Sagdeev, R.Z. and A.A. Galeev, *Nonlinear Plasma Theory,* W.A. Benjamin, New York, 1969.

Sawyer, D.M. and J.I. Vette, "AP-8 Trapped Proton Environment for Solar Maximum and Solar Minimum," NSSDC/WDC-A-R&S 76-06, NASA-GSFC TMS-72605, December 1976.

Schulz, M., "Geomagnetically Trapped Radiation," *Space Sci. Rev.*, **17**: 481, 1975a.

Schulz, M., "Particle Saturation of the Outer Zone, A Non-Linear Model," *Astrophys. Space Phys.*, **29**: 233, 1975b.

Schulz, M. and L.J. Lanzerotti, *Particle Diffusion in the Radiation Belts*, Springer-Verlag, New York, 1974.

Schulz, M. and G.A. Paulikas, "Secular Magnetic Variation and the Inner Proton Belt," *J. Geophys. Res.*, **77**: 744, 1972.

Sharp, R.D., R.G. Johnson, and E.G. Shelly, "The Morphology of Energetic O^+ Ions During Two Magnetic Storms, Temporal Variations," *J. Geophys. Res.*, **81**: 3283, 1976.

Shelley, E.G., R.G. Johnson, and R.D. Sharp, "Morphology of Energetic O^+ in the Magnetosphere," in *Magnetospheric Physics*, edited by B.M. McCormac, D. Reidel, Dordrecht, Holland, 1974.

Singley, G.W. and J.I. Vette, "The AE-4 Model of the Outer Radiation Zone Electron Environment," NSSDC 72-06, 1972.

Solov'ev, E.S., R.N. Il'in, V.A. Oparin, I.T. Serenkov, and N.V. Federenko, "Capture and Loss of Electrons by Fast Nitrogen and Oxygen Atoms and Ions in Air, Nitrogen and Oxygen," *Sov. Phys.-Tech. Phys.*, **37**: 777, 1975.

Söraas, F. and L.R. Davis, "Temporal Variations of the 10 keV to 1700 keV Trapped Protons Observed on Satellite Explorer 26 During First Half of 1965," NASA TMX-63320, GSFC, August 1968.

Spjeldvik, W.N., "Equilibrium Structure of Equatorially Mirroring Radiation Belt Protons," *J. Geophys. Res.*, **82**: 2801, 1977.

Spjeldvik, W.N., "Expected Charge States of Energetic Ions in the Magnetosphere," *Space Sci. Rev.* **23**: 499, 1979.

Spjeldvik, W.N. and T.A. Fritz, "Theory for Charge States of Energetic Oxygen Ions in the Earth's Radiation Belts," *J. Geophys. Res.*, **83**: 1583, 1978a.

Spjeldvik, W.N. and T.A. Fritz, "Energetic Ionized Helium in the Quiet Time Radiation Belts: Theory and Comparison with Observation," *J. Geophys. Res.*, **83**: 654, 1978b.

Spjeldvik, W.N. and T.A. Fritz, "Observations of Energetic Helium Ions in the Earth's Radiation Belts During a Sequence of Geomagnetic Storms," *J. Geophys. Res.*, **86**: 2317, 1981a.

Spjeldvik, W.N. and T.A. Fritz, "Energetic Heavy Ions with Nuclear Charge $Z \geq 4$ in the Equatorial Radiation Belts of the Earth: Magnetic Storms," *J. Geophys. Res.*, **86**: 2349, 1981b.

Spjeldvik, W.N. and L.R. Lyons, "On the Predictability of Radiation Belt Electron Precipitation into the Earth's Atmosphere Following Magnetic Storms," *Proceedings of the International Symposium on Geophysical Predictions, IV*, B-59, U.S. Department of Commerce, Boulder, 1980.

Spjeldvik, W.N. and R.M. Thorne, "The Cause of Storm After Effects in the Middle Latitude D-Region," *J. Atmos. Terr. Phys.*, **37**: 777, 1975.

Stassinopoulos, E.G. and P. Verzariv, "General Formula for Decay Lifetimes of Starfish Electrons," *J. Geophys. Res.*, **76**: 1841, 1971

Stebbings, R.F., W.L. Fite, and D.G. Hummer, "Charge Transfer Between Atomic Hydrogen and N^+ and O^+," *J. Chem. Phys.*, **33**: 1226, 1960.

Stix, T.H., *The Theory of Plasma Waves*, McGraw-Hill, New York, 1962.

Stone, E.C., "Physical Significance and Application of L, B_o and R_o to Geomagnetically Trapped Particles," *J. Geophys. Res.*, **68**: 4157, 1963.

Stormer, L., *Polar Aurora*, Clarendon Press, Oxford, 1955.

Teague, M.J., K.W. Chan, and J.I. Vette, "AE-6: A Model Environment of Trapped Electrons for Solar Maximum," NSSDC/WDC-A-R&S 76-04, May 1976.

Teague M.J., N.J. Schofield, K.W. Chan, and J.I. Vette, "A Study of Inner Zone Electron Data and Their Comparison with Trapped Radiation Models," NSSDC/GSFC, August 1979.

Teague, M.J. and E.G. Stassinopoulos, "A Model of the Starfish Flux in the Inner Radiation Zone," NASA-GSFC TMX-66211, December 1972.

Teague, M.J. and J.I. Vette, "The Inner Zone Electron Model AE-5," NSSDC/WDC-A-R&S 72-10, November 1972.

Teague, M.J. and J.I. Vette, "A Model of the Trapped Electron Population for Solar Minimum," NSSDC/WDC-A-R&S-74-03, NASA, April 1974.

Theodoridis, G.C., "Bimodal Diffusion in the Earth's Magnetosphere: 1. An Acceleration Mechanism for Trapped Particles," *Ann. Geophys.*, **24**: 944, 1968.

Tinsley, B.A., "Evidence that the Recovery Phase Ring Current Consists of Helium Ions," *J. Geophys. Res.*, **81**: 6193, 1976.

Vampola, A.L., "A New Study of the Outer Zone Electron Environment, A Hazard to CMOS," SAMSO-TR-77-127, June 1977.

Vampola, A.L. and G.A. Kuck, "Induced Precipitation of Inner Zone Electrons," *J. Geophys. Res.*, **83**: 2542, 1978.

Vette, J., I. King, W. Chan, and M.J. Teague, "Problems in Modelling the Earth's Trapped Radiation Environment," AFGL-TR-78-0130, ADA059273, 1978.

Vette, J.I., M.J. Teague, D.M. Sawyer, and K.W. Chan, "Modelling the Earth's Radiation Belts" in *Solar-Terrestrial Prediction Proceedings, Vol. 2*, edited by R.F. Donnelly, U.S. Department of Commerce, NOAA, Boulder, 1979.

Walt, M., "History of Artificial Radiation Belts" in *The Trapped Radiation Handbook*, edited by J.B. Cladis, G.T. Davidson, and L.L. Newkirk, Lockheed Palo Alto Research Laboratory, DNA 2524H, Revised January, 1977.

Walt, M. and L.L. Newkirk, "Addition to Investigation of the Decay of the Starfish Radiation Belt," *J. Geophys. Res.* **71**: 1966.

West, H.I., Jr., R.M. Buck, and G.T. Davidson, "The Dynamics of Energetic Electrons in the Earth's Outer

Radiation Belt During 1968 as Observed by the Lawrence Livermore National Laboratory's Spectrometer OGO-5," *J. Geophys. Res.,* **86:** 2111, 1981.

West, H.I., Jr., "The Signatures of the Various Regions of the Outer Magnetosphere in the Pitch Angle Distributions of Energetic Particles," in *Quantitative Modelling of Magnetospheric Processes,* edited by W.P. Olson, AGU, Washington D.C. 1979.

Williams, D.J., "An Overview of Radiation Belt Dynamics" in *Proceedings of the Air Force Geophysics Laboratory Workshop on the Earth's Radiation Belts: January 21–27, 1981,* edited by R.C. Sagalyn, W.N. Spjeldvik, and W.J. Burke, AFGL TR-81-0311, ADA113959, 1981.

Williams, D.J., "The Earth's Ring Current: Causes Generation and Decay," *Space Sci. Rev.* **34:** 223, 1983.

Young, D.T., "Ion Composition Measurements in Magnetospheric Modelling" in *Quantitative Modelling of Magnetospheric Processes,* edited by W.P. Olson, AGU Washington D.C. 1979.

Zinn, J., H. Hoerline, and A.G. Petschek, "The Motion of Bomb Debris Following the Starfish Test," in *Radiation Trapped in the Earth's Magnetic Field,* D. Reidel, Dordrecht, Holland, 1966.